Global numerical simulations of atmospheric ice crystals

Dissertation

for Attaining the Academic Degree of

"Doctor rerum naturalium (Dr. rer. nat.)"

of the Departments:

08 – Physics, Mathematics, and Computer Science
09 – Chemistry, Pharmaceutical Sciences, Geography, and Geosciences
10 – Biology
and University Medicine

of the Johannes Gutenberg University Mainz

Sara Bacer

born in Trieste

Mainz, 2019

First Reviewer:

Second Reviewer:

Day of the PhD defence: 3 April 2019

I hereby declare that I wrote the dissertation submitted without any unauthorized external assistance and used only sources acknowledged in the work. All textual passages which are appropriated verbatim or paraphrased from published and unpublished texts as well as all information obtained from oral sources are duly indicated and listed in accordance with bibliographical rules. In carrying out this research, I complied with the rules of standard scientific practice as formulated in the statutes of Johannes Gutenberg University Mainz to insure standard scientific practice.

Abstract

A comprehensive ice nucleation parameterization (Barahona and Nenes, 2009b, hereafter BN09) has been implemented in the global chemistry-climate model EMAC (ECHAM5/MESSy Atmospheric Chemistry) in order to improve the representation of ice crystal number concentration (ICNC). This parameterization takes into account the competition for water vapour between homogeneous and heterogeneous nucleation in cirrus clouds and the influence of different aerosol components on heterogeneous nucleation. Furthermore, the effect of pre-existing ice crystals, which deplete water vapour through their diffusional growth, has been included in the new algorithm. Thus, the implementation of BN09 allows one to simulate processes which are neglected by the standard configuration of EMAC used so far.

The modelled ICNCs obtained by using BN09 in the cirrus regime agree with the observations, as BN09 strongly reduces the ICNCs in the upper troposphere with respect to the standard model configuration. We found that the effect of pre-existing ice crystals is the main cause of such reduction. On the other hand, the ICNC reduction due to the water vapour competition between the ice nucleation mechanisms is very weak, thus, homogeneous ice nucleation is the dominant nucleation mechanism in cirrus clouds.

Focusing on the contributions of different aerosol components to immersion/condensation and deposition nucleation simulated via a parameterization included in BN09 (Phillips et al., 2013), we found that most of the new ice crystals in the cirrus regime derive from soluble organic compounds and in the mixed-phase regime from black carbon. Dust is on average less important than black carbon, and bioaerosols contribute by $\sim 20\%$ to form new ice crystals in the lower troposphere.

Finally, the analysis of the relative importance of the physical processes which produce and remove ice crystals shows that ice nucleation is the most important source in the upper troposphere, while convective detrainment and instantaneous freezing are more important at lower altitudes, at temperatures lower than -35°C. Sedimentation, which is the most important sink of ice crystals in the upper troposphere, is the main source in the mixed-phase regime.

Zusammenfassung

Eine umfassende Parametrisierung der Eiskeimbildung (Barahona and Nenes, 2009b, von hier an BN09) wurde in das globale Chemie-Klima-Modell EMAC (ECHAM5/MESSy Atmospheric Chemistry) implementiert, um die Berechnung der Anzahlkonzentration von Eiskristallen (ICNC) zu verbessern. Diese Parameterisierung berücksichtigt den Wettbewerb um Wasserdampf zwischen der homogenen und heterogenen Keimbildung in Zirruswolken und den Einfluss verschiedener Aerosolkomponenten auf die heterogene Keimbildung. Des Weiteren wird der Effekt von vorhandenen Eiskristallen, welche den Wasserdampfgehalt durch Diffusionswachstum verringern, im neuen Algorithmus berücksichtigt. Die Implementierung von BN09 erlaubt daher die Simulation von Prozessen, welche bislang in EMAC vernachlässigt wurden.

Mit BN09 modellierte ICNCs im Zirrus-Regime stimmen mit Beobachtungen überein, da BN09 die ICNCs in der oberen Troposphäre, relativ zum bisherigen EMAC model, reduziert. Der Effekt vorhandener Eiskristalle ist der Hauptgrund für diese Reduktion. Andererseits ist die ICNC-Reduzierung durch den Wettbewerb um Wasserdampf zwischen den Eiskeimbildungs-Mechanismen sehr schwach, daher ist die homogene Eiskeimbildung der dominante Mechanismus der Keimbildung in Zirruswolken.

Die Untersuchung der Beiträge verschiedener Aerosolkomponenten zur Immersions-/Kondensations- und Depositionsnukleation unter Verwendung der in BN09 enthaltenen Parameterisierung (Phillips et al., 2013) ergab, dass die meisten neuen Eiskristalle im Zirrus-Regime von löslichen organischen Stoffen und im Regime gemischter Phasen von Rußpartikeln herrühren. Staubpartikel sind im Durchschnitt weniger wichtig als Rußpartikel. Der Beitrag von Bioaerosolen zur Bildung neuer Eiskristalle liegt bei $\sim 20\%$ in der unteren Troposphäre.

Die Analyse der Bedeutung der verschiedenen physikalischen Prozesse, die Eiskristalle produzieren und entfernen, zeigt, dass Eiskeimbildung die wichtigste Quelle in der oberen Troposphäre ist, während konvektiver Entzug und instantanes Gefrieren in niedrigeren Höhen bei Temperaturen unter $-35°C$ wichtiger sind. Sedimentierung, die wichtigste Senke für Eiskristalle in der oberen Troposphäre, ist die Hauptquelle im Regime gemischter Phasen.

Contents

Introduction

Clouds cover about 70% of the terrestrial surface and play a fundamental role in the Earth System. They modulate the radiative fluxes in the atmosphere affecting the global energy budget: they reflect shortwave solar radiation back to space (*cloud albedo effect*) and absorb and re-emit at lower temperature the longwave radiation emitted by the Earth's surface and atmosphere (*greenhouse effect*). Different types of clouds have different impacts on the global energy budget, since factors such as temperature, size distribution and shape of cloud particles, and cloud phase change the reflectivity and the absorption-emission properties of clouds. Being the cloud albedo effect globally larger than the greenhouse effect, clouds cause a net cooling of the Earth System. In addition, clouds are part of the hydrological cycle, remove gaseous and particulate substances by scavenging, provide a medium for aqueous-phase chemical reactions, and influence the vertical redistribution of trace species, temperature, and moisture (Seinfeld and Pandis, 2006; Lohmann et al., 2016).

Further, aerosol–cloud interactions are also important for the atmosphere. In fact, aerosol particles can modify microphysical properties of clouds with effects on cloud albedo and cloud lifetime, and so on the global energy budget. On the other hand, clouds interact with aerosol particles removing them from the atmosphere by scavenging or changing their chemical composition when they are incorporated into cloud droplets.

Finally, clouds are thought to respond with different feedback mechanisms in a global warming scenario. For instance, high clouds are expected to rise in altitude exerting a stronger greenhouse effect, and storm tracks should move poleward causing a net shift of cloud cover towards latitudes that receive less solar radiation. The net cloud feedback is suggested to be positive, but its quantification remains difficult and cannot be confirmed neither by models nor by observations (IPCC, 2013).

Despite the great relevance of clouds, their understanding is still challenging and affected by large uncertainties (IPCC, 2013).

During the last two decades, significant improvements in sensors, instruments, measurement techniques, and post-processing algorithms have contributed to increase the knowledge of clouds. Nevertheless, some measurements are still not enough precise, and the interpretation of the observations can be ambiguous.

Moreover, cloud representation in atmospheric models has improved, also thanks to the increasing computer power, but many cloud processes are still poorly represented. In fact, the

numerical representation of clouds must contend with the poor understanding of the fundamental details of microphysical processes as well as the fact that cloud processes span several order of magnitudes, from nanometres to thousands of kilometres. Therefore, modelling of clouds remains a weak point in all atmospheric models, regardless of their resolution, and has been recognised as one of the dominant sources of uncertainty in climate studies (IPCC, 2013; Seinfeld et al., 2016).

Compared to warm (liquid) clouds, the microphysics of cold clouds is much more complicated because of the greater complexity of ice processes. Some examples are heterogeneous ice nucleation, which depends on particular aerosols and occurs in several ways, the secondary mechanisms of ice crystal formation, the competition for water vapour among different ice particles, and the thermodynamic instabilities when both liquid and ice phases coexist. As a result, processes in cold clouds and aerosol–cold cloud interactions are poorly understood and affected by large uncertainties (Cantrell and Heymsfield, 2005; Heymsfield et al., 2017; Korolev et al., 2017; IPCC, 2013).

This thesis is devoted to the study of cold clouds, with a particular focus on the ice nucleation mechanisms. The aim of the thesis is twofold. First, *to improve the representation of ice nucleation and in turn of ice crystal number concentration* in the global chemistry-climate model EMAC by implementing a comprehensive ice nucleation parameterization. Second, *to enhance the understanding of cold cloud microphysics* by analysing of the following points:

1. the competition for water vapour between homogeneous and heterogeneous nucleation in the cirrus regime and the effect of pre-existing ice crystals;
2. the contributions of different aerosol types on heterogeneous nucleation;
3. the relative importance of the physical processes which are sources and sinks of ice crystals in cold clouds.

The thesis is structured as follows. Chapter 1 provides the general background regarding the theory of cold cloud microphysics and an overview about cloud modelling and measurement techniques. Chapter 2 describes the EMAC model in general and those modules and parameterizations which concern clouds and ice nucleation more specifically. Chapter 3 describes the comprehensive ice nucleation parameterization of Barahona and Nenes (2009b) and its implementation in EMAC. The analyses of the model results and the evaluation of the model are given in Chapter 4. In Chapter 5, the water vapour competition between the ice nucleation mechanisms and the effect of pre-existing ice crystals are studied. Chapter 6 focuses on the contributions of different aerosol types on heterogeneous nucleation. Chapter 7 investigates the tendencies related to physical and microphysical processes of cold clouds. Finally, Chapter 8 summarises the results and presents the possible outlook.

The content of Chapters 3 and 4 closely follows Bacer et al. (2018).

Chapter 1

Cold clouds

Clouds can be divided in two main categories: *warm clouds* and *cold clouds*. Warm clouds are purely made of liquid water and their temperature is typically above 0°C, while cold clouds extend to altitudes where temperatures are below 0°C (*subfreezing temperatures*). It is common to observe water which is still liquid in clouds at low subfreezing temperatures, although common experience indicates that water freezes when the temperature falls below 0°C. While our experience is based on observations of bulk water in which a single ice nucleation event is sufficient to freeze the entire liquid water mass, clouds are an agglomeration of small liquid drops which must individually experience a nucleation event before the entire cloud is frozen (*glaciated*) (Rogers and Yau, 1989).

Cold clouds are classified as:

- *cirrus clouds,* consisting of purely ice crystals, at temperatures generally lower than −35°C,
- and *mixed-phase clouds*, including both ice crystals and supercooled liquid cloud droplets.

Cirrus clouds strongly impact the transport of water vapour entering the stratosphere, which in turn has a strong effect on radiation (Jensen et al., 2013), and play an important role in the global energy budget: differing from other types of clouds, they produce a positive net radiative effect at the top of the atmosphere (TOA) (Chen et al., 2000; Hong et al., 2016; Matus and L'Ecuyer, 2017). On the other hand, mixed-phase clouds exert a negative net radiative effect at TOA, although the estimates of their radiative effects are complicated by the coexistence of both ice and liquid cloud phases (Chen et al., 2000; Hong et al., 2016; Matus and L'Ecuyer, 2017). Mixed-phase clouds are thermodynamically unstable due to the difference between the vapour pressures over water and over ice, so ice crystals grow at the expense of water droplets (*Wegener–Bergeron–Findeisen* process) and clouds can convert into glaciated clouds (e.g. Korolev, 2007; Korolev et al., 2017). Precipitation is mainly formed in mixed-phase clouds, where ice crystals can grow quickly to precipitation-sized particles, while precipitation from cirrus clouds does not usually reach the surface (Lohmann, 2017).

At subfreezing temperatures, formation of new ice crystals takes place via homogeneous and heterogeneous nucleation. Ice crystals grow by water vapour deposition and other processes of collision-coalescence and can be removed from the atmosphere by sedimentation, sublimation,

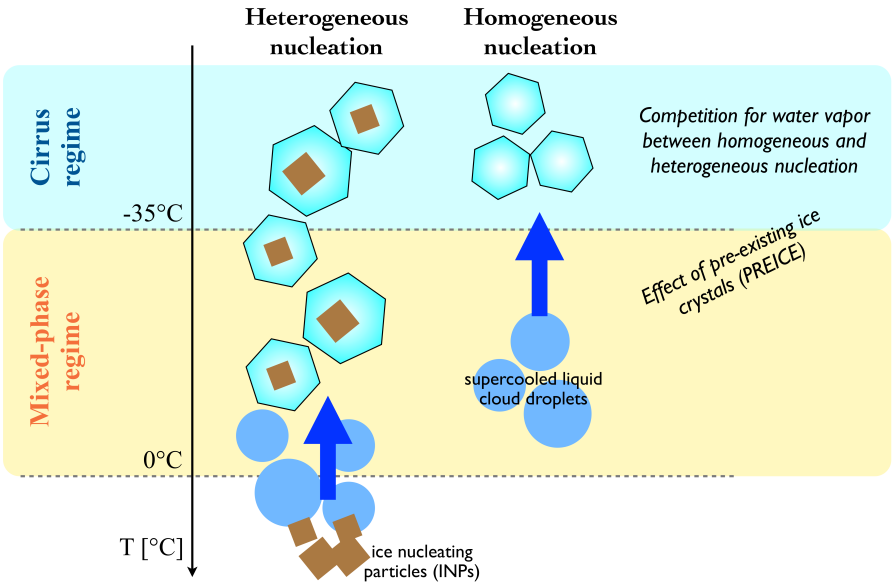

Figure 1.1: General picture for the two cloud regimes and ice nucleation mechanisms.

and melting. Ice crystal size ranges from few nanometres to few millimetres (Khain and Pinsky, 2018), and the number concentrations span from few crystals per litre of air (e.g in thin tropical tropopause layer – TTL cirrus) (Jensen et al., 2013) to several hundreds per cubic centimetre (e.g. in tropical convective updraughts) (Heymsfield et al., 2009), depending on the cloud type and geographical location. Generally, ice crystal concentrations are lower than typical aerosol concentrations by a factor of $10^3 - 10^4$ (Khain and Pinsky, 2018).

Two different cloud regimes are distinguished at subfreezing temperatures (Figure 1.1):

- the *cirrus regime* at temperatures lower than $-35°C$, where ice crystals originate via heterogeneous and homogeneous nucleation to form cirrus clouds;
- the *mixed-phase regime* at temperatures between $-35°C$ and $-0°C$, where ice crystals exclusively form via heterogeneous nucleation and alter the phase composition of the mixed-phase clouds.

This chapter provides much of the background necessary for the understanding of what is next in this thesis. Section 1.1 theoretically describes how ice crystals form and grow in cold clouds. Section 1.2 introduces the numerical representation of clouds, and in particular of ice nucleation, in global models, while Section 1.3 gives some brief information regarding different types of observations.

1.1 Cold cloud microphysics

1.1.1 Ice nucleation

At subfreezing temperatures, water molecules can exist in the vapour phase and liquid phase (supercooled water), in a thermodynamically metastable state, and in the solid phase (ice),

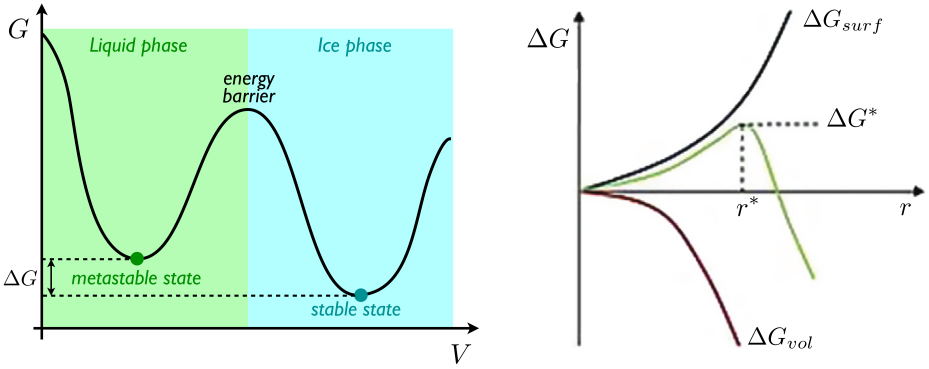

Figure 1.2: (*Left*) Gibbs free energy and the transition from the metastable state (supercooled liquid water) to the absolutely stable state (solid ice). (*Right*) Dependence of energy barrier (ΔG^*), interfacial energy (ΔG_{surf}), and volume energy (ΔG_{vol}) on embryo radius (adapted from Khain and Pinsky, 2018).

which is absolutely stable. Each phase is characterized by its own *Gibbs free energy* (G) such that the higher the stability, the lower the free energy (Khain and Pinsky, 2018). Thus, at subfreezing temperatures, vapour and liquid phases tend to move to the ice phase, having a lower G (Figure 1.2, left). The term *nucleation* denotes the initiation of a new thermodynamically stable phase which grows within the surrounding metastable parent phase, so *ice nucleation* indicates the formation of ice crystals through the initiation of the ice phase within the liquid or vapour phase (Lohmann et al., 2016).

The transition to the new (stable) phase, however, is not spontaneous but is hindered by an intermediate maximum of G, called *energy barrier* (Figure 1.2, left). Statistical fluctuations of water molecular arrangement in the parent phase due to thermal vibrations can lead to the spontaneous formation of ordered solid molecule clusters of the new phase with an ice-like structure (*ice embryo*). This results in fluctuations of G. When the amplitude of G is equal to or higher than the energy barrier, nucleation of ice occurs. In this way, the ice embryo has reached a critical size (*critical ice embryo* or *ice germ*) and has become thermodynamically favoured so that water molecules bind to the crystal lattice rapidly, initiating the spontaneous freezing of the entire parent phase. The stochastic nature of this theory is described by the so-called *classical nucleation theory* (CNT), which employs critical radii of ice germs, free energies, and nucleation rates as functions of both temperature and saturation ratios.

In the atmosphere, ice nucleation depends on environmental conditions (e.g. relative humidity, temperature, and pressure) and aerosol population (i.e. aerosol number concentrations and physicochemical characteristics, such as composition, shape, and surface tension) (Pruppacher and Klett, 1997; Kanji et al., 2017; Heymsfield et al., 2017). Of fundamental importance are the vertical air motions: the cooling (and the generation of ice supersaturation) associated to lifted air parcels depends on the strength of updraught velocities (e.g. $1 - 10$ cm s^{-1} in synoptic motions, $10 - 100$ cm s^{-1} in gravity waves, $100 - 1000$ cm s^{-1} in convective clouds) (Kärcher and Lohmann, 2002b).

Two types of ice nucleation mechanisms are possible in the atmosphere (Figure 1.1): *homogeneous ice nucleation* from liquid phase and *heterogeneous ice nucleation*, which occurs thanks to particular foreign aerosols called *ice nucleating particles* (INPs). Homogeneous ice nucleation from vapour phase is theoretically possible but requires very high relative humidities which are not observed in nature, therefore, only homogeneous ice nucleation from liquid water is described below.

1.1.1.1 Homogeneous ice nucleation

Homogeneous ice nucleation occurs at low temperatures (below $-35°C$) and high ice saturation ratios ($140\% - 160\%$). It is related to the number of cloud condensation nuclei (CCN) due to the freezing of *supercooled cloud droplets* (i.e. droplets with a negligible amount of solute, approximated to droplets of pure water) and *aqueous solution droplets* (i.e. liquid aerosols, like sulfuric acid, which have undergone hygroscopic growth) (Koop et al., 2000). While homogeneous nucleation of cloud droplets occurs mostly in deep convective clouds, homogeneous nucleation of solution droplets occurs in cirrus clouds which form in-situ (Lohmann et al., 2016).

The CNT defines the *Gibbs free energy change* associated to homogeneous nucleation from (pure) liquid water to ice phase ($\Delta G_{i,w}$, which will be indicated as ΔG for simplicity) as (Pruppacher and Klett, 1997; Ickes et al., 2015):

$$\begin{aligned} \Delta G &= \Delta G_{vol} + \Delta G_{surf} \\ &= -\frac{4\pi r^3 kT}{3\alpha_i} \ln \frac{e_{s,w}}{e_{s,i}} + 4\pi r^2 \sigma_{i,w} \end{aligned}$$

where r is the radius of the ice embryo, k is the Boltzmann constant, T is the temperature, $e_{s,w}$ and $e_{s,i}$ are the saturation vapour pressures over water and over ice, respectively, α_i is the specific volume of ice, and $\sigma_{i,w}$ is the surface tension of ice in water. The volume term (ΔG_{vol}) is proportional to the embryo volume and represents the difference in free energies between ice and supercooled liquid water. The surface term (ΔG_{surf}) is proportional to the embryo surface area and identifies the energy required to form a curved interface between liquid water and ice. Both terms are sketched in Figure 1.2 (right). The maximum of ΔG (ΔG^*) occurs at the *critical radius of the ice embryo* (determined by the condition $d\Delta G/dr = 0$):

$$r^* = \frac{2\sigma_{i,w}\alpha_i}{kT \ln(e_{s,w}/e_{s,i})} \ ,$$

which defines the *energy barrier to form a critical ice embryo from (pure) liquid water*:

$$\Delta G^* = \frac{16\pi}{3} \frac{\alpha_i^2 \sigma_{i,w}^3}{[kT \ln(e_{s,w}/e_{s,i})]^2} \ .$$

The lower the temperature, the larger the ratio $e_{s,w}/e_{s,i}$ (see Figure 1.12 in Subsection 1.1.3), the lower the energy barrier to form a critical ice embryo.

The energy barrier ΔG^* describes the thermodynamic part of ice nucleation in supercooled water, however, also the kinetic part describing the water molecules which can potentially be incorporated into the ice germ must be taken into account. Thus, the energy required for ice nucleation in supercooled water must actually overcome two energy barriers: ΔG^* and the *energy activation barrier* (ΔG^{act}), which is the minimum energy required to transfer a water molecule across the water–ice boundary and trigger the nucleation process (Pruppacher and Klett, 1997; Ickes et al., 2015; Khain and Pinsky, 2018).

An important quantity defined by the CNT is the *nucleation rate* J (in $\mathrm{m^{-3}\ s^{-1}}$), which describes the number of nucleation events (i.e. production of ice embryos with $r > r^*$) per unit volume of the parent phase and per unit time. Its formulation combines the termodynamic and the kinetic parts:

$$J_{hom} = A_{hom}(T) \exp\left(-\frac{\Delta G^* + \Delta G^{act}}{kT}\right),$$

where the factor $A_{hom}(T)$ incorporates different parameters and constants and varies with temperature (see Pruppacher and Klett, 1997, for more details). J_{hom} is highly sensitive to temperature and a threshold value (T_{th}) for the onset of homogeneous nucleation is introduced. Empirical measurements show that clouds do not contain liquid droplets once temperatures around $-40°\mathrm{C} \div -35°\mathrm{C}$ are attained, so T_{th} is associated to a value within this interval (Rogers and Yau, 1989).

As the growth velocity of ice is high at $T < T_{th}$, it is often assumed that, once the ice embryo reaches its critical size, its spontaneous growth within a droplet leads to the instantaneous freezing of the entire droplet. Therefore, one nucleation event per drop is enough to form an ice crystal. In this way, the nucleation rate is associated with the rate of ice crystal formation (Pruppacher and Klett, 1997). Additionally, it can be assumed that any nucleation event is independent from that in other droplets. Under these conditions, ice crystal formation is a stochastic process which can be described through the Poisson distribution. The probability that no nucleation event takes place in a time interval (Δt) is: $P(0, \Delta t) = \exp\left(-V_d J_{hom} \Delta t\right)$, where $V_d = \frac{4}{3}\pi r_d^3$ is the droplet volume. Hence, the *freezing probability of a droplet* is $[1 - \exp\left(-V_d J_{hom} \Delta t\right)]$, and the number concentration of ice crystals (ICNCs) formed in Δt from droplets with radius r_d is (Khain and Pinsky, 2018):

$$\Delta\mathrm{ICNC}_{r_d} = \mathrm{CDNC}_{r_d} \left[1 - \exp\left(-V_d J_{hom} \Delta t\right)\right] \ ,$$

where CDNC_{r_d} is the number concentration of cloud droplets with radius r_d. Since it is usually assumed that the bulk radius of an ice crystal is equal to the droplet radius, for a multidisperse population of cloud droplets the total concentration of ice crystals formed in Δt is (Khain and Pinsky, 2018):

$$\Delta\mathrm{ICNC} = \int_0^\infty f(r_d) \left[1 - \exp\left(-V_d J_{hom} \Delta t\right)\right] dr_d \ ,$$

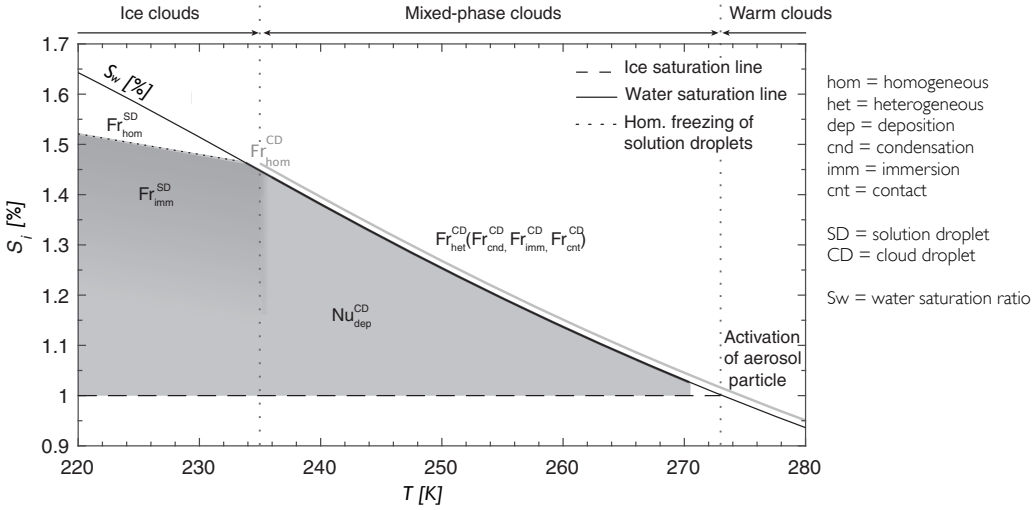

Figure 1.3: Nucleation mechanisms as functions of temperature (T) and ice saturation ratio (S_i) (adapted from Lohmann et al., 2016). The sloping dotted line (which starts at 235 K) marks the minimum S_i for solution droplets to freeze homogeneously, according to Koop et al. (2000).

where $f(r_d)$ is the size distribution of cloud droplets. The formula shows that the larger the volume of a droplet or the larger the time interval, the higher the probability of water molecules to change orientation in the supercooled droplet, and the higher the probability for an ice germ to be produced.

The CNT for pure water described so far can be extended to solution droplets, taking into account the fact that homogeneous ice nucleation from supercooled aqueous solutions depends on the water activity of the solution (Koop et al., 2000). Due to the freezing point depression of solution droplets, they freeze at lower temperatures than pure water droplets, hence, the higher the solute concentration, the lower the T_{th} associated to solution droplets. Additionally, thanks to the Raoult's effect which predicts the reduction of $e_{s,w}$ over a solution with respect to $e_{s,w}$ over pure water, homogeneous nucleation can be extended to relative humidities with respect to water lower than 100% (Figure 1.3).

1.1.1.2 Heterogeneous ice nucleation

Heterogeneous ice nucleation refers to the formation of ice germs on foreign aerosol surfaces which, reducing the energy barrier for ice nucleation, let ice crystals form at lower ice supersaturation and/or higher (subfreezing) temperature than homogeneous nucleation. This means that supercooled water droplets can freeze with the aid of a suitable subset of atmospheric aerosols (i.e. INPs) also at temperatures higher than T_{th}. Therefore, heterogeneous nucleation occurs in both cloud regimes, causing a competition for water vapour with homogeneous nucleation in the cirrus regime. While homogeneous nucleation occurs at values of ice supersaturation and temperature which are restricted in a narrow interval and primarily depend on

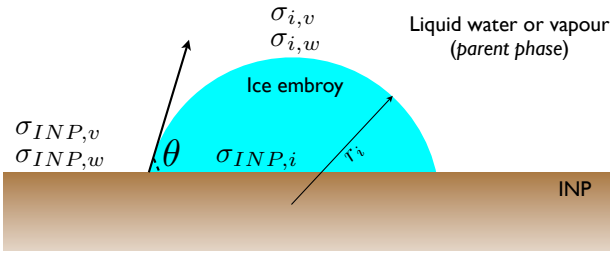

Figure 1.4: Contact angle (θ) in case of a planar surface of INP. $\sigma_{INP,i}$ is the surface tension between INP and ice embryo, $\sigma_{INP,w}$ and $\sigma_{INP,v}$ between INP and parent phase (liquid water or vapour), $\sigma_{i,w}$ and $\sigma_{i,v}$ between ice embryo and parent phase.

the water activity in the liquid phase (Koop et al., 2000), heterogeneous nucleation exhibits a broad range of freezing thresholds (Pruppacher and Klett, 1997).

The CNT applied to heterogeneous nucleation predicts the decrease of the energy barrier to form an ice embryo due to the smaller number of water molecules required to join the embryo before it reaches its critical radius with respect to the case of homogeneous nucleation. The theory is based on the concept of surface "wettability", which is represented by the so-called *contact angle* (θ). As illustrated in Figure 1.4, the ice embryos form a spherical cap on the INP surface. The interactions among ice embryo, INP, and parent phase (liquid water or vapour) are described via the surface tensions ($\sigma_{INP,i}$, $\sigma_{INP,w}$ or $\sigma_{INP,v}$, and $\sigma_{i,w}$ or $\sigma_{i,v}$) and are incorporated in the contact angle as follows: $\cos\theta = (\sigma_{INP,w} - \sigma_{INP,i})/\sigma_{i,w}$. This gives the measure of the wettability of the surface; for instance, when $\sigma_{INP,w} = \sigma_{i,w}$ and $\sigma_{INP,i} = 0$, $\cos\theta = 1$, and the INP is perfectly hydrophilic. The bigger the difference between $\sigma_{i,w}$ and $\sigma_{INP,i}$ (where $\sigma_{i,w} > \sigma_{INP,i}$), the smaller the θ, the more hydrophilic the INP surface, the lower the barrier ΔG^* (Figure 1.5).

The resulting reduction in the *energy barrier to form an ice embryo on an INP surface*, i.e. the energy barrier for heterogeneous nucleation, can be approximated as follows (Lohmann et al., 2016):

$$\Delta G^*_{het} \approx f(\cos\theta)\Delta G^*,$$

where $f(\cos\theta)$ is a geometric factor which depends on the contact angle and is limited by the extremes $f = 0$ when $\theta = 0°$ and $f = 1$ when $\theta = 180°$ (associated to homogeneous nucleation), so that $\Delta G^*_{het} \leq \Delta G^*$. In reality, the INP surface is not planar but has different shapes, so the geometric factor is also a function of the equivalent radius of the insoluble fraction in INP (r_{insol}) and r^*. Additionally, ΔG^* in the equation above should be slightly modified including a factor which characterises the misfit between the lattice of the INP and that of the ice germ (Khain and Pinsky, 2018).

The nucleation rate associated to heterogeneous nucleation has a similar form to J_{hom} and

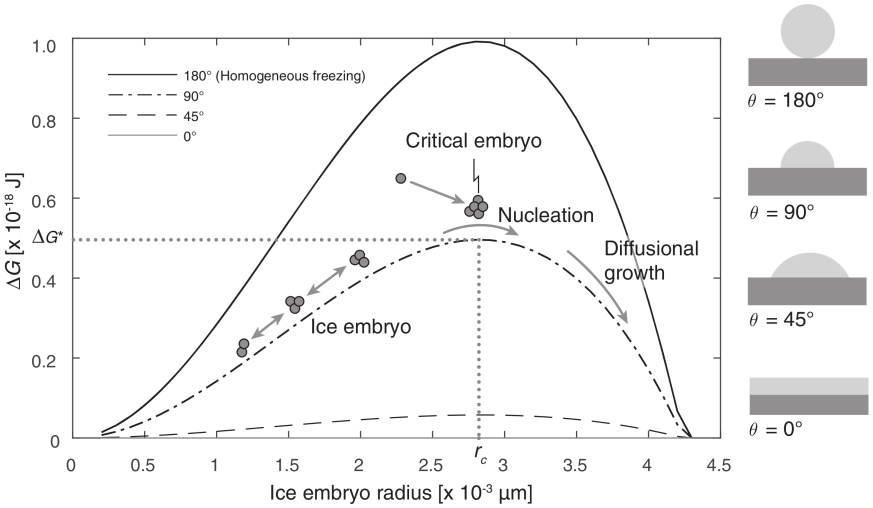

Figure 1.5: Gibbs free energy changes (ΔG) for homogeneous and heterogeneous nucleation and schematic illustration of various contact angles (from Lohmann et al., 2016).

can be expressed as (Pruppacher and Klett, 1997; Khain and Pinsky, 2018):

$$J_{het} = A_{het}(T, r_{insol}) \exp\left(-\frac{\Delta G^*_{het} + \Delta G^{act}}{kT}\right),$$

where the factor $A_{het}(T, r_{insol})$ incorporates different parameters and constants and varies with T and r_{insol} (see Pruppacher and Klett, 1997, for more details). It must be mentioned that the values of the contact angles and their distributions are poorly known, introducing significant uncertainties in the quantification of J_{het} (Kanji et al., 2017).

Heterogeneous nucleation occurs via different mechanisms called *nucleation modes* (Pruppacher and Klett, 1997; Kanji et al., 2017; Khain and Pinsky, 2018), which are listed below and schematically illustrated in Figure 1.6. (The symbols S_w and S_i will be used to indicate the saturation ratios over water and over ice, respectively; they will be defined in Subsection 1.1.3.)

- *Contact nucleation mode.*
  The collision between an INP and a spercooled cloud droplet causes the freezing of the droplet. The requirement of the droplet presence implies that relative humidities are near water saturation ($S_w = 1$). When INPs are large enough (> 0.1 μm), the inertial effects are not negligible and the hydrodynamic effects dominate; when INPs are smaller than 0.1 μm and move randomly, the collision mechanism is dominated by the Brownian diffusion.

- *Condensation nucleation mode.*
  As INPs usually contain some soluble material in addition to the insoluble part, they can act firstly as CCN and then as INP to initiate the freezing of the droplet.

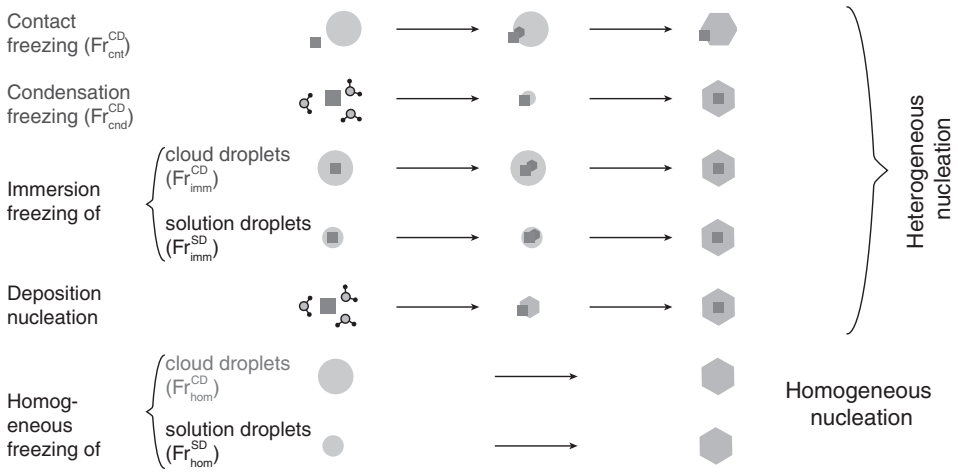

Figure 1.6: Schematic representation of the different ice nucleation mechanisms. The cubes represent INPs, the spheres droplets, the hexagons ice crystals (adapted from Lohmann et al., 2016).

- *Immersion nucleation mode.*
  The INP already immersed in the cloud or solution droplet initiates the freezing of the droplet upon its cooling. The prior existence of droplets imply that $S_w = 1$ for the freezing of cloud droplets, while there can be subsaturation ($S_w < 1$) for the freezing of solution droplets.

- *Deposition nucleation mode.*
  Water vapour can directly deposit onto the INP surface at ice supersaturation conditions ($S_i > 1$), although the minimum value of S_i is uncertain and could be higher than the unity (Lohmann et al., 2016).

This theoretical distinction of the ice nucleation modes is affected by large uncertainties because, in practice, it is challenging to differentiate all of them, especially the condensation mode which is often joined to the immersion mode. The relative importance of the different modes in the atmosphere is also not well established. The immersion and contact modes are suggested to be important in mixed-phase clouds, while the deposition mode might be important in the cirrus clouds (Kanji et al., 2017).

1.1.1.3 Ice nucleating particles

Besides temperature and ice supersaturation, which are the main environmental factors that determine ice nucleation, the physicochemical properties of INPs play a significant role in the heterogeneous nucleation initiation. Whereas in warm clouds the droplet concentration is directly related to the CCN number, in cold clouds the relationship between ice crystal concentration and INP number is more complicated and nonlinear. INPs are a subset of aerosols with physicochemical characteristics which facilitate the adsorption of water molecules and the formation of ice-like structures, so that ice crystals can form heterogeneously at lower

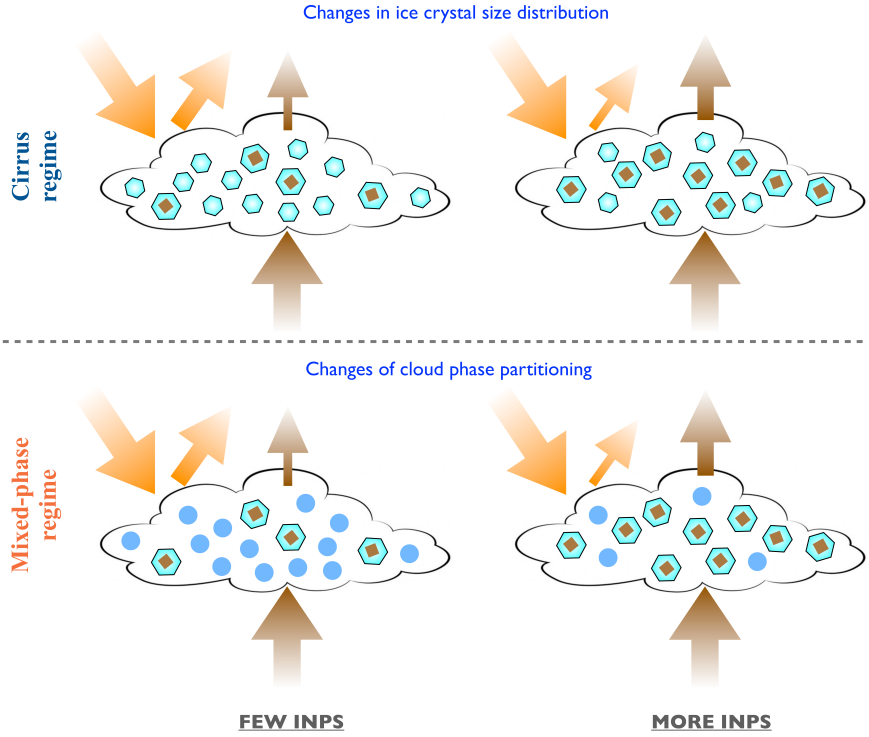

Figure 1.7: Changes in cloud radiative effects due to INP perturbations, in cirrus and mixed-phase clouds.

ice supersaturation and/or higher temperature than homogeneous nucleation (as remarked before).

INP concentrations are lower than CCN concentrations by orders of magnitude (Storelvmo, 2017), nevertheless, their perturbations strongly alter the optical properties of both mixed-phase and cirrus clouds, and so their cloud radiative effects (Figure 1.7). INP perturbations influence the liquid-ice phase partitioning in mixed-phase clouds: since ice crystals are approximately one order of magnitude larger than liquid droplets, a liquid cloud is optically thicker than an ice cloud for the same condensed water content (Korolev et al., 2017). Additionally, changes in INP concentrations modify the ice crystal size distribution in cirrus clouds: in the case of few INPs, homogeneous nucleation can still occur and cirrus clouds are formed by many small ice crystals; in the case of more INPs, cirrus clouds include fewer and larger ice crystals, so they are optically thinner (Heymsfield et al., 2017).

It is still not known with enough detail which properties make an aerosol particle an INP nor the main responsible aerosol types for the ice initiation (Kanji et al., 2017). Historically, the following requirements have been suggested (Pruppacher and Klett, 1997):

- insolubility;
- large size (typically > 0.1 μm);
- similar hydrogen bonds at surface (to facilitate the formation of ice crystal lattice);
- crystallographic lattice;

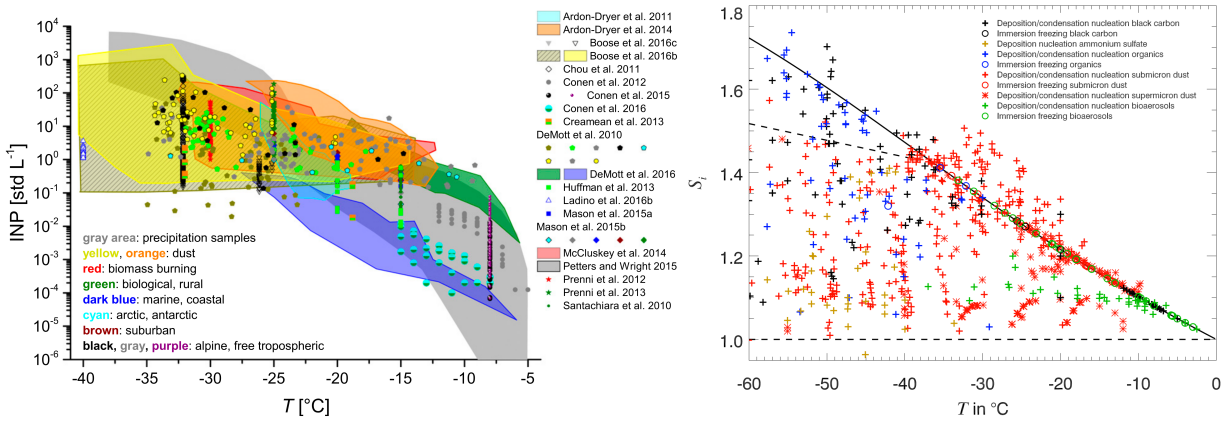

Figure 1.8: (*Left*) Summary of INP concentrations taken from studies of field measurmenets (from Khain and Pinsky, 2018). (*Right*) Overview of ice nucelation onset temperatures and saturation ratios (from Hoose and Möhler, 2012).

- *active sites* on surface (i.e. localised features, such as cracks or chemical impurities, which are more likely to adsorb water molecules and initiate ice nucleation).

However, recent observations have shown that biological macromolecules with diameters ~ 10 nm can be ice nucleating active, against the conventional requirement that INPs need to be insoluble or large (Khain and Pinsky, 2018). Also, solid ammonium sulfate aerosols have been recently observed to be involved in ice heterogeneous nucleation (Abbatt et al., 2006), questioning the insolubility requirement.

So far, several aerosol types have been identified as more or less efficient INPs (Figure 1.8, left): mineral dust from deserts, soil dust from grazed and agricultural lands, metals generated by anthropogenic activities, organic material, glassy organics, biomass burning particles, soot, bioaerosols, sea salt, and volcanic ash particles (Hoose and Möhler, 2012; Khain and Pinsky, 2018). Figure 1.8 (left) clearly shows an exponential increase of INP concentrations with decreasing temperatures, as expected from the CNT. However, the spread of the concentrations is several orders of magnitude large at any temperature. Below, more information is provided for the four aerosol components analysed in this thesis and shown in Figure 1.8 (right).

- **Mineral dust (DU).**
  Mineral dust particles derive from arid soils and deserts and are considered the most important INPs because of their high efficiency in ice initiation and their large abundance in the atmosphere. Dust particles can generally form ice crystals at $T < -15$°C, depending on their size (larger particles tend to nucleate ice at higher temperatures) and their mineral composition (montmorillonite, kaolinite, and illite are the most abundant clay minerals, but the studies concerning their ice nucleation ability have lead to contrasting results) (Hoose et al., 2008b; Hoose and Möhler, 2012). Mineral dust is important at regional scale but also at global scale, as it can be transported far away from its sources (Khain and Pinsky, 2018).

- **Black carbon (BC).**
  Black carbon is emitted as primary particle from incomplete combustion processes of fossil fuels (soot) and biomass burning sources (ash), such as forest and agricultural fires, wood stoves, heating, and industrial activities. Given their high emission rates, ash and soot may influence ice formation in clouds, however, their importance is still unclear because observational studies are contradictory. Additionally, the determination of ice nucleation ability of black carbon is complicated by the fact that it varies in composition depending on its combustible source and mixing state (chemical aging and coatings decrease the INP efficiency). Overall, the BC ability to nucleate ice in the atmosphere is still uncertain, especially at cirrus temperatures (Hoose and Möhler, 2012).

- **Organic compounds (OC).**
  Aqueous solution droplets containing a range of soluble oxygenated organic compounds are expected to be liquid at high temperatures, but they can covert to a highly viscous, semisolid amorphous state, named *glassy*, at very low temperatures. Glassy organics can form ice crystals heterogeneously in the cirrus regime, especially in the TTL at $T < -70°C$ in the deposition mode or at slightly elevated temperatures in the immersion mode. The temperature at which they are able to nucleate ice is strongly related to their glass transition temperature (Murray et al., 2010; Wilson et al., 2012).

- **Bioaerosols (BIO).**
  Primary biological aerosol particles (PBAPs or bioaerosols) are emitted by biogenic sources, such as vegetation, oceans, soils, and living organisms. Some example are bacteria, fungal spores, pollen, viruses, lichens, phytoplankton, and plant fragments. Their emission rates are orders of magnitude smaller than dust and their residence time can be very short (even less than one day) due to their large size (up to hundreds micrometers) and the resulting high settling velocity, hindering their lift up to cloud levels. Nevertheless, bacteria, fungal spores, and pollen have been identified as good INPs. As visible in Figure 1.8, bioaerosols have the ability to nucleate ice at high subzero temperatures, and some species only need $T < -2°C$. Thus, due to their high ice nucleation onset temperatures, bioaerosols can have an important role in the formation of ice at regional scale, especially over vegetative areas (e.g. the Amazon) where they are abundant. Additionally, they can reach high altitudes and be transported over long distances when they are associated to dust particles (Pratt et al., 2009; Prenni et al., 2009; Després et al., 2012).

The actual contribution of INPs to ice nucleation is an interplay between INP abundances and INP efficiencies, quantities which are highly variable and difficult to be determined. Measured concentrations of ice crystals in clouds range from the lower limit of detectability (0.01 L^{-1} or 0.1 L^{-1}) to about 100 L^{-1}. Additionally, a large discrepancy between ICNCs and INP concentrations has been observed, up to a factor of 10^4 at high subfreezing temperatures (Rogers and Yau, 1989; Kanji et al., 2017). Initially, it was suggested that the shattering

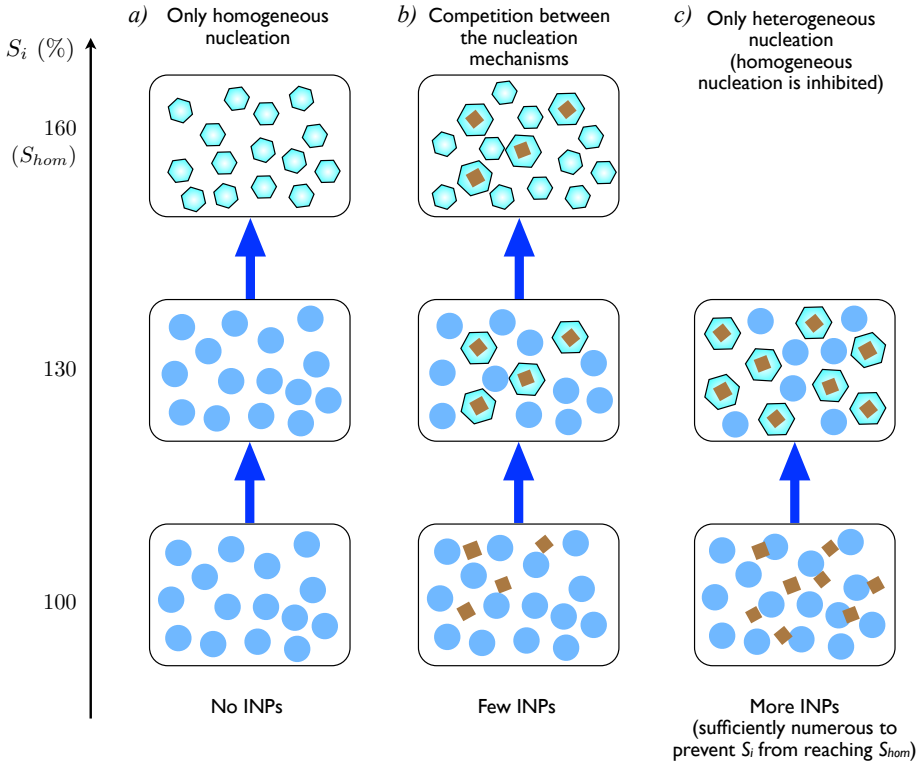

Figure 1.9: Schematic of competition for water vapour between homogeneous and heterogeneous nucleation. Circles are supercooled liquid cloud droplets, hexagons are ice crystals, and squares are INPs.

of ice crystals caused by the probe inlets could artificially increase the ICNC measurements, but the discrepancies have persisted also after the employment of antishattering inlets. Now, the most likely explanation for the high ICNCs is the existence of another mechanism named "secondary ice production", which produces new ice crystals through the "multiplication" of the primary ice crystals (see Subsection 1.1.2).

1.1.1.4 Competition for water vapour

While in the mixed-phase regime only heterogeneous ice nucleation is possible, in the cirrus regime both homogeneous and heterogeneous nucleation can occur simultaneously (Figure 1.1). The competition for water vapour between homogeneous and heterogeneous nucleation is schematised in Figure 1.9, where a lifted air parcel at $T < -35°C$ is analysed in three different situations. In the absence of INPs, the ice saturation ratio reaches the homogeneous nucleation threshold (S_{hom}), so homogeneous nucleation occurs and produces high number concentrations of small ice crystals (Figure 1.9a). Since INPs become active at lower ice supersaturation (e.g. $\sim 30\%$) than homogeneous nucleation, the available water vapour and the degree of supersaturation decrease in the presence of INPs, reducing the formation of ice crystals via homogeneous nucleation (Figure 1.9b). If INPs are sufficiently numerous to prevent the ice saturation ratio from even reaching S_{hom}, homogeneous nucleation is inhibited, and

ice crystals are formed only heterogeneously (Figure 1.9c). The final number of ice particles is lower than the clean air case (i.e. Figure 1.9a) as not all supercooled liquid droplets have been converted to ice.

It has been shown that the competition between the ice nucleation mechanisms drastically affects the ICNC in the cirrus regime, even at low INP concentrations (Kärcher and Lohmann, 2003; Spichtinger and Cziczo, 2010), and so the cloud optical properties. However, it is currently a matter of debate whether cirrus clouds are mainly formed homogeneously or whether sufficient INPs exist to cause widespread heterogeneous nucleation. Homogeneous nucleation has been considered the dominant process for cirrus formation in several modelling studies (e.g. Hendricks et al., 2011; Gettelman et al., 2012; Spichtinger and Krämer, 2013; Barahona et al., 2014), because the concentration of liquid droplets is higher than that of INPs in the upper troposphere, and observational studies (e.g. Krämer et al., 2016; Voigt et al., 2017). However, Barahona et al. (2017) have shown that heterogeneous nucleation is dominant in cirrus formation, in agreement with other field measurements (e.g. Cziczo et al., 2013; Jensen et al., 2013).

Furthermore, both in the cirrus regime and in the mixed-phase regime, water vapour can also be reduced by depositional growth onto pre-existing ice crystals and ice crystals carried into the cloud via convective detrainment and advective transport. Thus, the *pre-existing ice crystal effect* (PREICE) can inhibit ice nucleation as well. The PREICE can be especially important in cirrus clouds when ice crystals are of small size and have low sedimentation rates, on the other hand, it can be weak where temperatures are low and vertical velocities are high (Shi et al., 2015), like in tropical convections.

1.1.2 Secondary ice production

Secondary ice production (or *ice multiplication*) is a secondary process which leads to the production of new ice crystals through the multiplication of pre-existing (primary) ice crystals. It has received less attention than primary ice nucleation but is potentially important for controlling ICNCs. The following secondary mechanisms (illustrated in Figure 1.10) have been recognised (Rogers and Yau, 1989; Lohmann et al., 2016; Field et al., 2017), although some of them have been little quantified because of the challenging observations and measurements.

- *Rime splintering* (or *Hallet-Mossop process*), i.e. the ejection of small ice crystals (*splinters*) consequent from the capture of supercooled droplets by large ice particles (e.g. graupels) between -3°C and -8°C (Figure 1.10a). When supercooled droplets (larger than 25 μm in diameter) collide with graupels, they freeze from the surface towards the inner part which expands against the frozen surface producing cracks and ejecting ice splinters (Hallett and Mossp, 1974). The narrow temperature range is explained as follows: when $T > -3$°C, droplets tend to spread over the graupel surface loosing their discrete entity, when $T < -8$°C, droplets freeze so rapidly that the outer ice shell is too thick to be cracked.

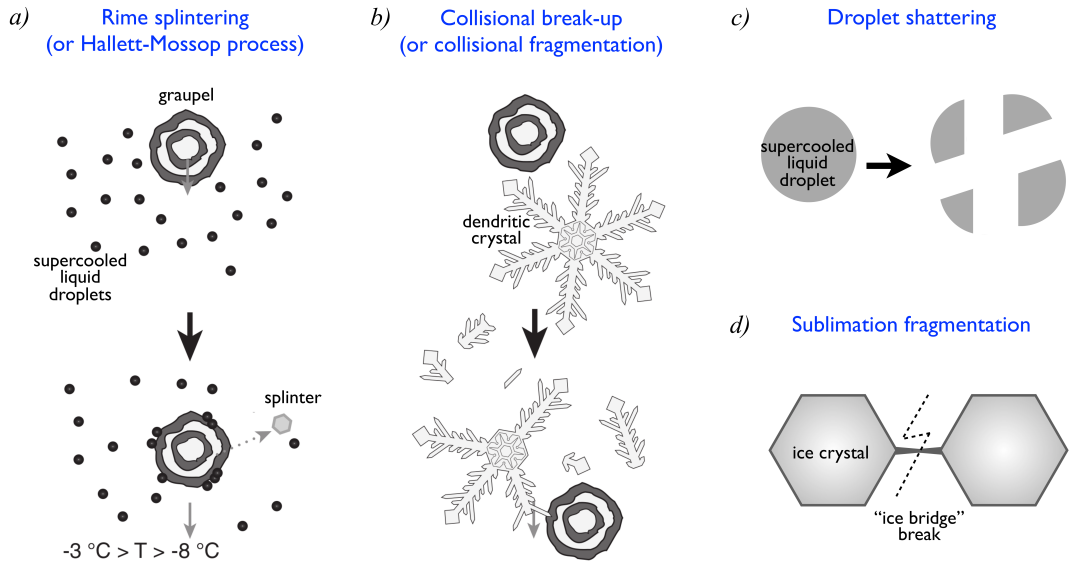

Figure 1.10: Ice multiplication mechanisms (the schematics for rime splintering and collisional break-up are adapted from Lohmann et al., 2016).

- *Collisional break-up* (or *collisional fragmentation*), i.e. small ice particles produced from the break-up of fragile slower-falling dendritic crystals which collide with dense graupel particles (Figure 1.10b).
- *Droplet shattering*, when large cloud droplets freeze and then shatter, producing splinters (Figure 1.10c) (Brownscombe and Thorndike, 1968). This process still needs to be explored in detail but seems to be efficient especially between $-10°C$ and $-15°C$.
- *Sublimation fragmentation*, when ice particles break from parent ice particles after the sublimation of "ice bridges" at subfreezing temperatures (until $-30°C$) and ice subsaturated conditions (Figure 1.10d). The break-up probability is strongly dependent on the particle shape and is higher for irregular particles (Bacon et al., 1998).

1.1.3 Ice crystal growth

Although the CNT assumes that newly formed ice crystals are spherical, in reality ice crystals have complicated shapes (*habits*). Indeed, the surface energy required to create a new surface for a given volume is minimised only if the shape of the ice crystal has a hexagonal lattice structure (*equilibrium shape*) made of water molecules arranged in a tetrahedral manner via the hydrogen bonds (e.g. columns and plates). When molecules do not have enough time to arrange themselves in the thermodinamically favored way, habits deviate from the equilibrium shape forming, for example, dendrites, needles, and stellar plates. Ice crystal habits are determined by temperature and ambient supersaturation (Figure 1.11) and have a strong impact on radiative properties and fall velocities of ice particles. Nevertheless, ambient conditions determine not only ice crystal habits, but also the ice crystal growth.

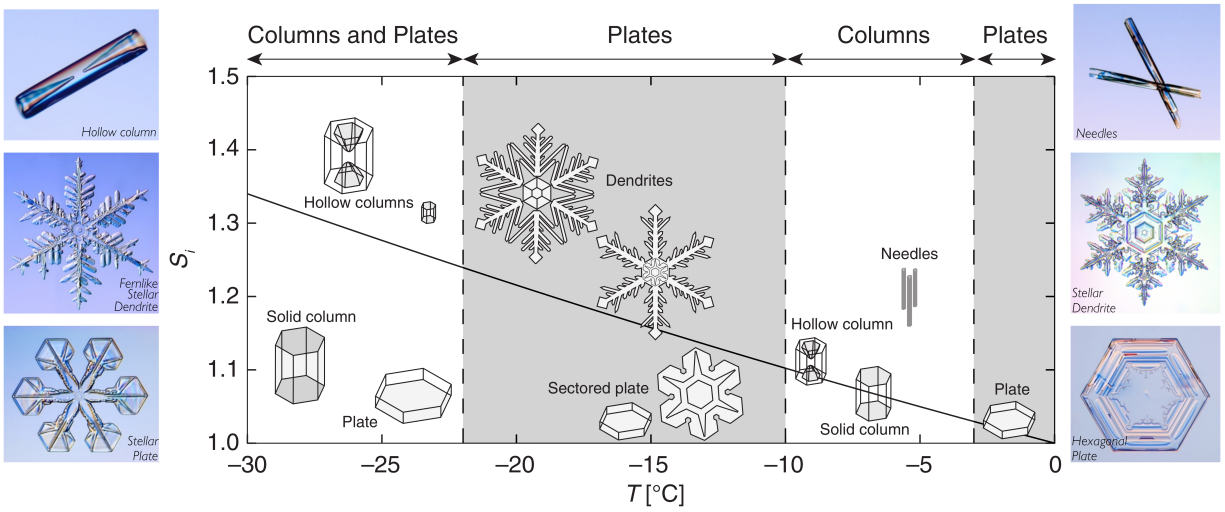

Figure 1.11: Ice crystal habits as a function of temperature and ice saturation ratio (from Lohmann et al., 2016, while the photographs are taken from www.snowcrystals.com).

As already visible in Figure 1.3, air can be supersaturated with respect to both water and ice. When an air parcel rises in the atmosphere, it undergoes an adiabatic cooling expansion which reduces the saturation vapour pressure over water ($e_{s,w}$), while the ambient water vapour pressure (e) decreases in proportion to the decreasing air pressure. As a result, the relative humidity with respect to water, named also water saturation ratio ($S_w = e/e_{s,w}$), increases even over 100% promoting condensation and cloud droplet formation until S_w is back to the equilibrium state ($S_w = 1$). At the same time, also the saturation vapour pressure over ice ($e_{s,i}$) decreases. As the intermolecular bonding energy is higher in ice than in liquid water, the flux of water molecules needed to compensate sublimation of molecules from ice is lower than the flux required to balance the evaporation from liquid water, i.e. $e_{s,i} < e_{s,w}$ at subfreezing temperatures (Figure 1.12, left). This means that an environment which is saturated with respect to liquid water is always supersaturated with respect to ice, i.e. the ice saturation ratio ($S_i = e/e_{s,i}$) is greater than one. Thus, at any temperature below freezing, ice is not in equilibrium with liquid water: whenever both phases coexist, the imbalance causes a continuous flux of water molecules from liquid to ice.

In the atmosphere, water supersaturation (i.e. water saturation ratio above the equilibrium: $s_w = S_w - 1$) of only $1\% - 2\%$ is observed, while very large ice supersaturation (i.e. ice saturation ratio above the equilibrium: $s_i = S_i - 1$) is possible (and necessary for ice crystal formation as seen in Subsection 1.1.1). The difference between $e_{s,w}$ and $e_{s,i}$ implies that mixed-phase clouds are thermodynamically unstable and offer a favourable environment for ice crystals to grow by diffusion at the expense of water droplets via the so-called *Wegener-Bergeron-Findeisen* (WBF) process (Pruppacher and Klett, 1997). The WBF process occurs when both water phases (liquid and ice) coexist and $e_{s,i} < e < e_{s,w}$ (Korolev, 2007). The diffusional growth of ice crystals is faster when the absolute difference between the saturation vapour pressures is larger (i.e. at $T \simeq -12°C$, see Figure 1.12, right). The WBF process is

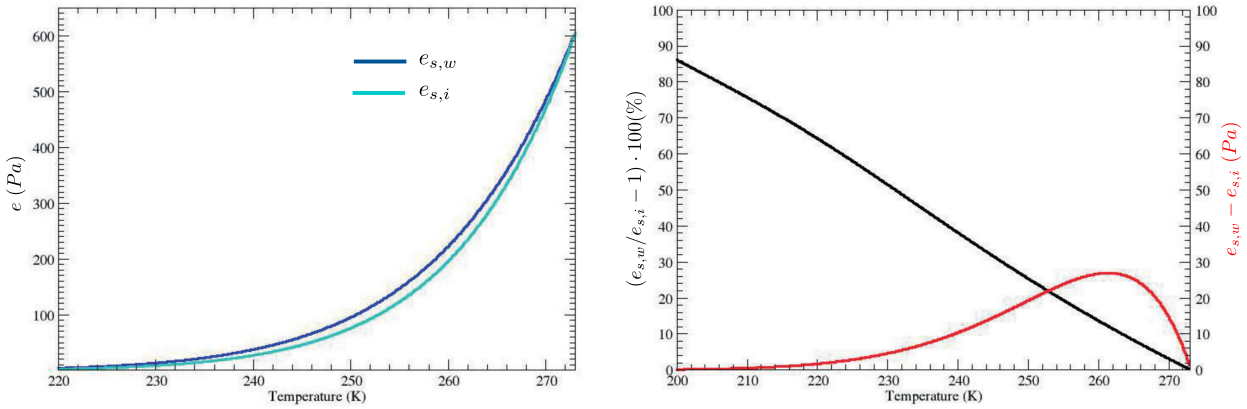

Figure 1.12: (*Left*) Saturation water vapour pressure over liquid water ($e_{s,w}$) and over ice ($e_{s,i}$) as a function of subfreezing temperature (from Storelvmo and Tan, 2015). (*Right*) Differences between $e_{s,w}$ and $e_{s,i}$ as functions of subfreezing temperatures: absolute difference (red line), with maximum around $-12°$C, and relative difference (black line), which is exacerbated with decreasing temperature (from Storelvmo and Tan, 2015).

schematically shown in Figure 1.13. Given an environment where the ambient vapour pressure is saturated with respect to liquid droplets, water molecules diffuse from droplets and deposit on ice crystals surface, reducing S_w below the saturation value. In order for the liquid droplets to restore the equilibrium, water molecules evaporate from the liquid surface to increase again the ambient vapour pressure and maintain the equilibrium ($S_w = 1$). In this way, ice crystals grow by deposition at the expense of the liquid droplets, which instead shrink. When liquid droplets are completely evaporated, air is subsaturated with respect to water and ice crystals can have reached sufficiently large sizes to precipitate out of the cloud (Storelvmo and Tan, 2015). Therefore, the WBF process can convert mixed-phase clouds into ice-only clouds and is an important mechanism of ice crystal growth and precipitation formation in the mixed-phase regime (e.g. Korolev, 2007; Korolev et al., 2017).

Nevertheless, ice crystals grow also by *diffusion* (Vapor + IC $\rightarrow$ IC, when $e_{s,i} < e$) without the presence of liquid droplets (Figure 1.14a). The diffusional growth rate is expressed in terms of a mass growth rather than a radius growth, given the non-spherical shapes of ice crystals, and includes an accommodation coefficient which takes into account the fact that not all attempts of water molecules to stick the ice surface are successful (as water molecules can stick only if they are oriented correctly in order to maintain the crystal lattice).

Another mechanism of growth for ice crystals is the *collision-coalescence* process (named also *collection* or *aggregation*) between ice particles as well as between ice particles and other hydrometeors, leading to the formation of hydrometeors which belong to either the type of the colliding particles or a third type (e.g. snow, graupel, and hail). Hence, collection is also a sink for ICNCs, in addition to being a growth mechanism for ice crystals. The process is characterised by the *collection efficiency*. It is the product of the *collision efficiency* (which depends on the mass and shape of the particles), the *coalescence efficiency* (which depends on

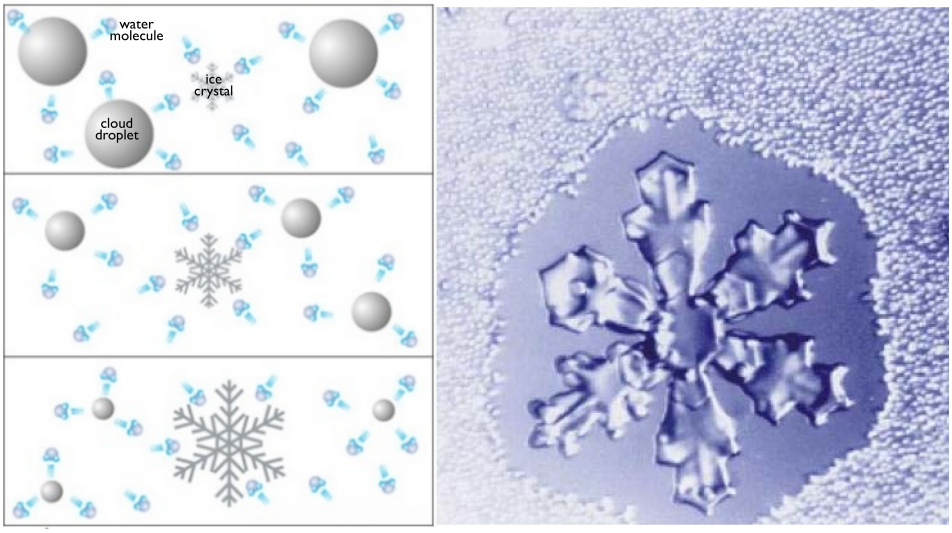

Figure 1.13: (*Left*) Schematic of the WBF process. (*Right*) Photo by R. Pitter of the WBF process.

the surface properties and shape of the particles, and the temperature, as ice crystals are more likely to stick together at higher temperatures), and the relative fall velocity of the colliding particles.

Several types of collection involving ice crystals have been defined (Rogers and Yau, 1989; Lohmann et al., 2016; Khain and Pinsky, 2018).

- *Self-collection* (IC + IC → IC).
  It consists in the collision-coalescence between hydrometeors of the same type, in this case ice crystals, and the production of hydrometeors of the same type but larger size. This process reduces ICNCs but does not change the mass content of ice.

- *Aggregation* (IC + IC → Snow).
  It is a combination of self-collection and *auto-conversion* processes: the ice crystals collide and clump together to form an aggregated snowflake (Figure 1.14b). Observations have shown that aggregation is mainly limited to temperatures higher than −10°C, due to the higher values of the temperature-dependent coalescence efficiency.

- *Accretion* (Snow + IC → Snow).
  Growth by accretion indicates the collection between two different hydrometeors, in this case between ice crystals and snowflakes (Figure 1.14b).

- *Riming* (Liquid + IC → IC).
  This process refers to the collision of ice crystals with supercooled liquid droplets which freeze upon the contact; the coalescence coefficient in this case is approximately unity (Figure 1.14c).

Growing ice crystals can sediment with different fall velocities. Sedimentation is an important process which affects the vertical profile of ICNCs. For instance, heterogeneously-formed

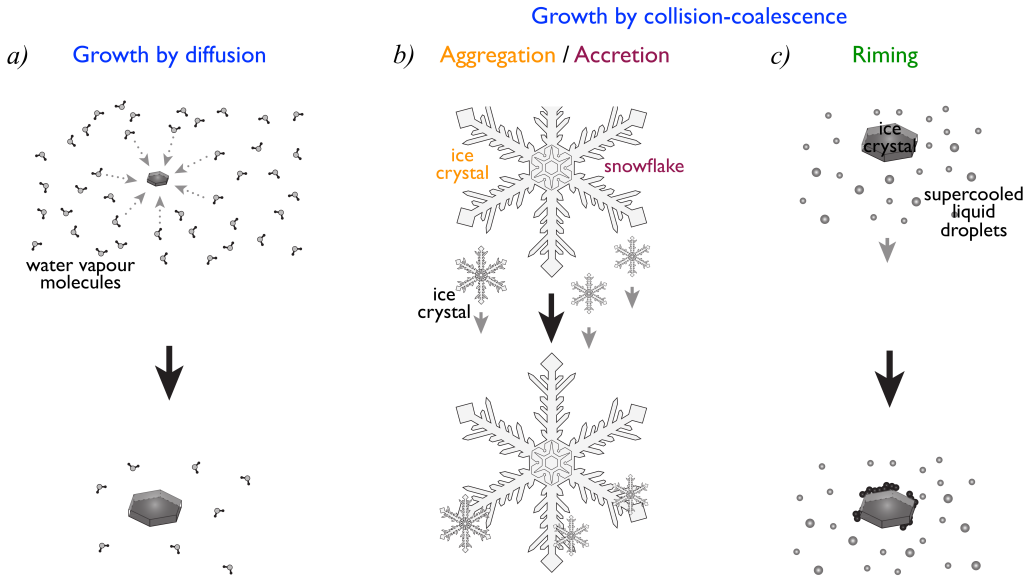

Figure 1.14: Schematic of ice crystal growth mechanisms (adapted from Lohmann et al., 2016).

ice crystals (which are usually bigger than those formed homogeneously) can sediment fast, before reaching the level where homogeneous nucleation takes place, thus, preventing any influence on this ice nucleation mechanism. Finally, growing ice crystals can reach a precipitation size and initiate precipitation.

1.2 Numerical representations in GCMs

Cloud processes cover a wide range of spatial and temporal scales, from nanometres to thousands of kilometres and from milliseconds to weeks (Figure 1.15). Even high resolution models cannot resolve the processes occurring at the smallest scales, hence, parameterizations must be used to represent subgrid unresolved processes.

In order to build physically-based parameterizations, cloud parcel models (CPMs) can be used (Khain and Pinsky, 2018). Parcel model equations encode the theoretical understanding of the physics controlling the evolution of cloud particles (e.g. aerosol activation and particle growth) in an individual volume of air. Thus, CPMs simulate the smallest scales relevant for clouds via a closed system of ordinary differential equations, which can be numerically integrated in time, and allow changes of various physical and chemical properties of cloud particles (Chen and Lamb, 1994, 1999).

Models which resolve turbulent motions within deep convective clouds (cloud-resolving model – CRM) or even turbulent eddies in the boundary layer (large-eddy simulation – LES) make use of parameterizations. They are important tools to interpret observations, to reveal features at the microscale which should be parameterized, and to test and improve parameterizations. However, these models are computationally demanding and are suitable only for

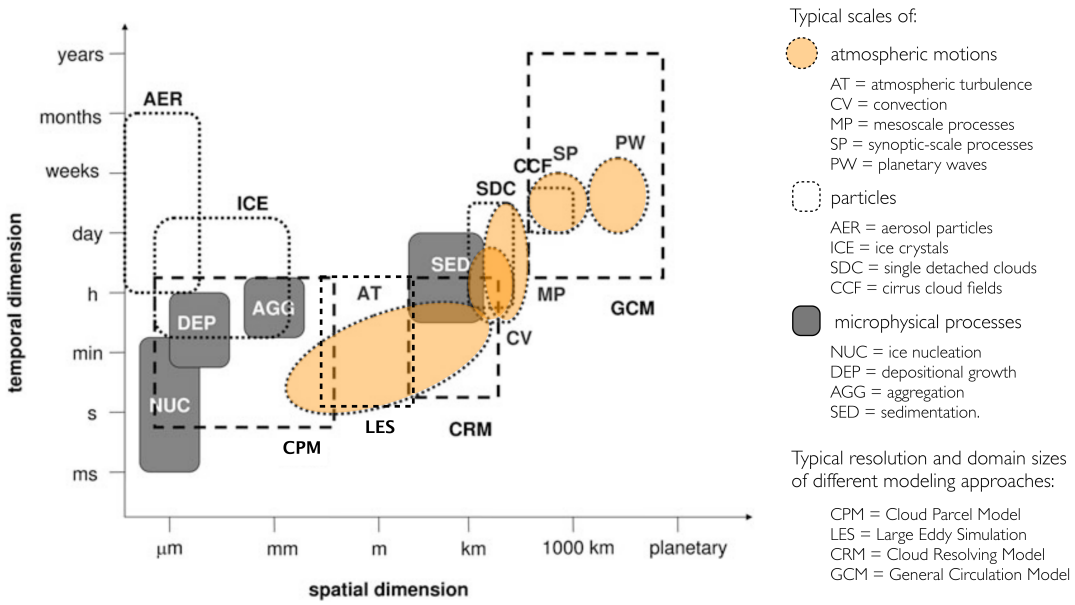

Figure 1.15: Typical scales of atmospheric motions (light orange), clouds (white), microphysical processes (dark gray) relevant for the formation and developments of ice clouds (adapted from Burkhardt and Sölch, 2012).

small domains, so that they cannot simulate cloud interactions with large scale dynamics nor quantify global radiative effects of clouds. For global estimates and climate studies, general circulation models (GCMs) must be used.

GCMs typically have a horizontal resolution of the order of hundred kilometres and represent all the subgrid processes via several parameterizations, for instance, convective clouds and large-scale (stratiform) clouds are handled by different parameterizations. Parameterising subgrid processes means to express smaller scale variabilities in terms of large-scale variables which are resolved by the model (Lohmann et al., 2007a). As this thesis concerns stratiform clouds, some general information about their parameterizations is provided below.

1.2.1 Stratiform cloud microphysics parameterizations

Different quantities characterising cloud properties can be described through specific *moments of the particle size distribution* (PSD) (Khain and Pinsky, 2018):

$$M_i = \int_{m_{min}}^{m_{max}} m^i f(m) dm \ ,$$

where m is the cloud particle mass, $f(m)$ is the PSD as a function of m, $f(m)dm$ is the number of particles (per unit of volume) with mass ranging from m to $m + dm$, and i is the order of the moment. For example, the *zero-order moment* of the PSD is the particle number concentration:

$$N = \int_{m_{min}}^{m_{max}} f(m) dm \ ,$$

the *first-order moment* describes the mass contents (e.g. mixing ratio), and the *second-order moment* describes the radar reflectivity.

PSDs are represented differently in numerical models according to the approach used to simulate the cloud microphysics (Khain and Pinsky, 2018).

- *Spectral bin parameterizations* aim to simulate cloud microphysics as accurate as possible, and PSDs are defined for every type of hydrometeor on a discrete mass grid containing from tens to hundreds mass bins (where each j-bin contains particles of mass m_j). No PSD shape is assumed, and PSDs are computed (prognostically) by solving explicit microphysical equations.

- *Bulk parameterizations* aim to represent the most general microphysical cloud properties (or bulk properties) using semiempirical descriptions of PSDs. Some schemes use only one moment of the distribution (usually the mass content of the hydrometeor, $i = 1$) and are called *one-moment (bulk) schemes*, others use two moments (usually the number concentration and the mass content, $i = 0, 1$) and are named *two-moment (bulk) schemes*. PSDs are represented by specific mathematical functions which are determined by few parameters and whose relations between moments are known. Several mathematical functions have been used for ice particles, for example, exponential functions, the lognormal distribution, and the Gamma function. Prognostic equations are solved for each moment and for each hydrometeor type. The number of equations solved in bulk parameterizations is lower (normally by one order of magnitude) than that in spectral schemes.

1.2.2 Ice nucleation parameterizations

Ice nucleation parameterizations can be theoretically based or empirically derived. The key parameter to be parameterized in homogeneous nucleation schemes is the nucleation rate (see Subsection 1.1.1). It can be obtained from the CNT (e.g. in Barahona and Nenes, 2008) or from laboratory measurements (e.g. Koop et al., 2000).

On the other hand, parameterizations which simulate heterogeneous nucleation starting from an INP population (called "INP parameterizations") follow two different approaches which are based on two main hypothesis (Kanji et al., 2017; Lohmann et al., 2016; Pruppacher and Klett, 1997).

- The *stochastic hypothesis* assumes that the freezing process is stochastic and time dependent. Given an ensemble of identical ice embryos formed on the surface of identical supercooled liquid droplets at a certain temperature, the ice embryos have the same probability per unit time of reaching the critical size, thanks to random fluctuations among water molecules (so at fixed ambient conditions, the probability increases with time). The presence of INPs enhances the efficiency of the random fluctuations without disturbing the stochastic nature of the process, hence, the theory is equivalent for both homogeneous and heterogeneous nucleation. The CNT follows this approach and

describes ice nucleation through the nucleation rate prognostic variable. This theory has as drawback the fact that it tends to overpredict ICNCs.

- The *singular (deterministic) hypothesis* assumes that ice nucleation is a deterministic and time independent process. This approach assumes that each INP is characterised by a distinct freezing temperature/ice saturation ratio below/above which ice nucleation is triggered. Consequently, heterogeneous nucleation is fully determined by the ambient conditions and does not depend on time. The parameterizations of this category are empirically developed from fits obtained with INP measurements as a function of ice supersaturation (e.g. Meyers et al., 1992), temperature (e.g. Fletcher, 1962), temperature and aerosol concentrations (e.g. DeMott et al., 2010), temperature, ice supersaturation, and aerosol numbers (e.g. Phillips et al., 2008, 2013). Some parameterizations have been developed by using atmospheric INP observations (e.g. DeMott et al., 2010; Phillips et al., 2008, 2013), others by using laboratory measurements (Lohmann and Diehl, 2006). The number of new ice crystals is expressed in terms of the site density (i.e. the number of active sites per unit surface area), assuming that one active site corresponds to the freezing of a single ice crystal, and the INP surface area. The first parameter is empirically derived, while the second one is provided by the model in which the parameterization is implemented. Being explicitly temperature dependent, the drawback of these parameterizations is their limited use in large-scale models, which require a wide temperature range.

Experimental studies have shown that heterogeneous nucleation has both a stochastic and a deterministic component, although stochastic effects are less important because of the dominance of specific active sites which promote ice nucleation (Kanji et al., 2017). Current models use either the stochastic or the singular approach (Khain and Pinsky, 2018). Information about the parameterizations used in this thesis is included in Sections 2.3 and 3.1.

1.2.3 State-of-the-art of numerical models

Currently, state-of-the-art GCMs use two-moment schemes, for example ECHAM5 (Lohmann et al., 2007b), CAM5 (Gettelman et al., 2012), and GEOS-5 (Barahona et al., 2014). The advantage of using a two-moment scheme is that it enables the simulation of aerosol–cloud interactions and, therefore, allows for a more realistic representation of cloud–radiation feedbacks (Burkhardt and Sölch, 2012). Cloud schemes in atmospheric and climate models have evolved from using only macrophysical properties, like cloud cover, to representing the microphysics explicitly, e.g. formation, evolution, and removal of cloud droplets and ice crystals (Gettelman et al., 2010; Barahona et al., 2014). Including in GCMs sophisticated schemes which solve physically-based equations allows for a more realistic description of clouds, variability in cloud properties and cloud radiative effects, improving the climate predictions (Lohmann and Feichter, 2005; Kanji et al., 2017). The use of an accurate aerosol model for the representation of INPs is also of fundamental importance (Kanji et al., 2017). Nevertheless, some processes are still not included in most of the standard model versions (e.g. the PREICE and the WBF

process) or are poorly represented (e.g. chemical aging and coatings of INPs). Additionally, the vertical velocity is usually highly simplified in GCMs, despite its fundamental role in ice nucleation (Donner et al., 2016).

Recently, sophisticated ice nucleation parameterizations have been developed, taking into account the aerosol influence on ice formation and the different modes of heterogeneous nucleation. These schemes also allow for the simulation of ice supersaturation (e.g. Kärcher and Lohmann, 2002a), reached for example when growth rates of ice crystals are too slow to drop S_i to the equilibrium within one model time step. (Previously, the *saturation adjustment* hypothesis was applied, i.e. it was assumed that air in clouds could be only saturated and any supersaturation was instantaneously removed by transforming water vapour to cloud condensate.)

Liu and Penner (2005) presented an ice nucleation scheme based on the numerical solutions of a parcel model and considered the competition between homogeneous and heterogeneous nucleation following the CNT. Kärcher et al. (2006) developed a physically-based parameterization for ice initiation and ice crystal initial growth in cirrus clouds, considering the PREICE and allowing for the competition between the ice nucleation mechanisms. Barahona and Nenes (2009b) introduced an ice cloud formation parameterization based on the analytical solution of the cloud parcel model equations. Their scheme calculates the competition for water vapour between homogeneous and heterogeneous nucleation and takes into account the variability (in size and chemical composition) of different aerosol components through a variety of INP parameterizations.

Since then, these parameterizations have been included in GCMs in order to better predict ICNCs and cloud phase partitioning. Hendricks et al. (2011) and Kuebbeler et al. (2014) implemented the parameterization of Kärcher et al. (2006) into the ECHAM4 and ECHAM5-HAM models, respectively. The parameterization of Liu and Penner (2005) was implemented into the CAM3 and CAM5 models by Liu et al. (2007) and Liu et al. (2012), respectively. Also, Liu et al. (2012) and Barahona et al. (2014) implemented the scheme of Barahona and Nenes (2009b) in CAM5 and GEOS-5, respectively. In this thesis, the scheme of Barahona and Nenes (2009b) has been implemented in EMAC (as described in Section 3.2).

1.3 Observations

Measurements of quantities related to cold clouds are carried out in three different ways: in laboratories, in the field (*in-situ measurements*), and by remote (*remote sensing*). In-situ measurements are performed exactly at the measurement location, by means of a sensor which is in direct contact with the quantity of interest, and are discrete in space; remote sensing observations are taken from a distance and offer a larger (even global) coverage. Merging all types of measurements is crucial to get a global and deep insight of atmospheric phenomena. Different kinds of measurements will be mentioned along this thesis, so a short overview about the observation techniques is now provided.

1.3.1 Laboratory measurements

Laboratory studies are focused on the microscale. They concern, for instance, INPs (e.g. their physical properties, chemical composition, efficiency to nucleate ice, and possible coatings), nucleation modes (e.g. the required thermodynamic conditions), ice crystal habits and their reflectivity properties, and growth processes. The samples analysed in laboratory in order to study ice nucleation can have different origin. They can be samples collected directly from the atmosphere (*natural particles*), the remaining part of a hydrometeor after evaporation/sublimation of water (*ice residuals*), or particles produced artificially (*artificial particles*).

Ice nucleation mechanisms and ICNCs are investigated in laboratories via the so-called "cloud chambers" or *continuous flow diffusion chambers* (CFDCs). CFDCs provide controlled water vapour content and temperature at which aerosols can nucleate ice; then, some ice crystal detection methods (e.g. optical particle counter) are used to count the number of crystals as a function of supercooling (Rogers and Yau, 1989). Each cloud chamber is built to study specific ice nucleation mechanisms at certain ranges of temperature. Some of the chambers vary only the temperature, others only the relative humidity, others can vary both parameters (e.g. the aerosol interaction and dynamics in the atmosphere – AIDA chamber). The cloud chambers in laboratories are large, but they can be also smaller to be installed onboard aircraft for in-situ measurements (Cziczo et al., 2017).

1.3.2 In-situ measurements

Observations in the field can be *airborne* (performed from aircraft) or *ground-based* (performed at stations located at high altitudes).

Numerous flight campaigns have been carried out in the last couple of decades, nevertheless, their measurements remain very discrete in space. Flight campaigns can have mixed-phase clouds (e.g. ICE-L, 2011) or cirrus clouds (e.g. ML-CIRRUS; Voigt et al., 2017) as targets. In the first case, the coverage is limited to the Northern Hemisphere (NH) and in particular over North America and the surrounding oceanic regions; in the second case, the coverage is global, although more field campaigns have been conducted in the NH (Storelvmo, 2017). Recently, aircraft measurements of different campaigns have been collected in a unified larger (in space and time) data set which provides a sort of climatology, suitable for evaluations of global simulations and satellite observations (e.g. Krämer et al., 2009, Krämer et al., 2016, and the JUeLich In-situ Airborne – JULIA database by Krämer (personal communication) for cirrus clouds). Additionally, global observations of atmospheric trace gases, aerosols, and cloud properties (such as cloud particle size distributions) have being collected from passenger aircraft (e.g. In-service Aircraft for a Global Observing System – IAGOS).

Examples of instruments installed on aircraft are the following ones (Storelvmo, 2017; Cziczo et al., 2017; Baumgardner et al., 2017).

- The portable version of the CFDC and the *forward scattering spectrometer probe* (FSSP) are both used to measure number concentrations of INPs and ice crystals. The FSSP is

an optical particle counter which detects the particles by measuring the intensity of the scattering when they pass through a light beam. The two versions of FSSP, FSSP100 and FSSP300, measure particles in the size ranges $1.5-15$ μm and $0.3-20$ μm, respectively, and are generally able to detect $\sim$ 90% of the total ICNCs in cirrus clouds (Krämer et al., 2009).

- The *counterflow virtual impactor* (CVI) is used to measure ice residuals. It separates small particles from larger cloud particles which can overcome the counterflow and sublimates the condensed phase of the collected particles, releasing the residuals. However, only crystals up to a size of 50 μm can be stopped and sublimated, so only a smaller fraction of the total ice crystals can be sampled.

- The *single-particle mass spectrometer* (SPMS) determines the chemical composition of single particles (e.g. ice residuals). It detects and sizes particles using the scattered light as they pass through one or two laser beams set at a fixed distance. Then, another laser (typically in the near UV) is used to evaporate the particles and ionize the components; the extracted ions are detected by a time-of-flight mass spectrometer (TOFMS) which produces a complete mass spectrum on a single-particle basis.

- The *imaging probe* is an imaging spectrometer which use imaging to reconstruct cloud particle shape and size.

Meteorological variables (e.g. temperature and relative humidity) are measured from aircraft as well, so that indications of what ice nucleation mechanism is likely to dominate are inferred. Observed ICNCs can be artificially high due to the ice crystal shattering caused by the impact with the inlet (see Subsection 1.1.1). Recently, new instruments and post-processing techniques have been developed to avoid this artifact, and previous data sets have been revised.

Ground-based stations typically operates in the mixed-phase regime due to their lower altitudes with respect to the flight heights (e.g. the research station Jungfraujoch in the Swiss Alps). No ground-based observations will be used in this thesis.

1.3.3 Remote sensing

Remote sensing is mainly based on the measurement of electromagnetic radiation. It can be performed by *active sensors*, which emit radiation towards atmospheric targets, and the part which is scattered back is detected by a receiving sensor, and *passive sensors*, which detect the natural radiation emitted or scattered by the targets (reflected sunlight is the most common external source of radiation sensed by passive sensors, such as the radiometer). In general, remote sensors do not perform direct measurements of the target, but the measurements must be "interpreted" and converted into the desired observation (which is named *retrieval*). The synergy of different remote sensing systems considerably improve the insight into the physics of clouds and precipitation.

Two common active sensors in meteorology are the radar and the lidar.

- The weather RADAR (RAdio Detection And Ranging) transmits a short pulse of high power electromagnetic waves through a directional antenna and records the reflected signal with high spatial ($100 - 1000$ m) and temporal ($2 - 10$ min) resolution. Radar retrieves the information and provides insights of three-dimensional structures of clouds and precipitation systems. The wavelength is selected according to the target of interest. Cloud radars use short wavelengths (between 8 mm and 3 mm) to enable the detection of cloud droplets and ice crystals (down to diameters of 10 μm). They are used to investigate various cloud parameters: size and amount of cloud particles (which are related to the reflectivity), types of hydrometeors (their different fall velocities are responsible for different Doppler frequencies), liquid and ice water contents (Hagen et al., 2012).

- The atmospheric LiDAR (Light Detection And Ranging) transmits a light pulse through a laser and detects the reflected light with a receiving sensor. Differences in laser return times and wavelengths are used also in this case to provide a three-dimensional representation of the targets, such as aerosols, clouds, and other constituents of the atmosphere. The lidar is also employed to discriminate liquid and ice particles in mixed-phase clouds.

Remote sensors can work from ground-based stations, aircraft, and satellites. Satellites have the advantage of providing a global coverage and are of crucial importance for the evaluation and improvement of weather forecasting and climate models. They are differentiated in *geostationary satellites* and *polar orbiting satellites*. Geostationary satellites orbit ~ 35800 km directly above the Equator with an orbital period which matches the Earth's rotational period, keeping so a fixed location above the Equator. Due to their position, they do not offer a good view of high latitudes. By contrast, polar orbiting satellites (and nearly-polar orbiting satellites) orbit at much lower altitudes (~ 850 km) above (or nearly above) both poles of the Earth. Since the Earth rotates beneath, they cover the entire globe at least once per day and provide detailed images even at high latitudes. Nearly-polar orbiting satellites are sun-synchronous when they orbit over any location of the Earth's surface at the same local time.

Some satellites which provide vertically-resolved observations concerning clouds are embedded into the NASA's "Afternoon Satellite Constellation" (named *A-Train*), which includes five polar-orbiting satellites. Among these, *CloudSat* has a Cloud Profiling Radar (CPR) onboard, and *CALIPSO* (Cloud–Aerosol Lidar and Infrared Pathfinder Satellite Observations) uses a Cloud Aerosol Lidar with Orthogonal Polarization (CALIOP). While CALIOP operates at short wavelengths (532 nm and 1064 nm) and is sensitive to small cloud particles, CPR operates at higher wavelengths (~ 3 mm) and is sensitive to larger and precipitating particles. Therefore, CALIOP detects thin cirrus clouds and cloud tops, while CPR probes thicker clouds and precipitation systems which cannot be penetrated by lidars (Bühl et al., 2017). Some algorithms have been developed taking the advantage of the CALIOP-CPR synergy to produce advanced products, like the cloud retrievals of the liDAR-raDAR (DARDAR) data set (Delanoë and Hogan, 2010). DARDAR has been recently used by Sourdeval et al. (2018) to retrieve ICNCs, providing a new observational data set useful for model evaluations.

Chapter 2

The EMAC model

This chapter presents the chemistry-climate model EMAC (ECHAM5/MESSy Atmospheric Chemistry). It is a general circulation model which includes a dynamical core, ECHAM5, and the MESSY interface, which links a variety of submodels designed for the representation of tropospheric and middle atmosphere processes and their feedback with radiation.

The first two sections describe the ECHAM5 model (Section 2.1) and the MESSY interface (Section 2.2), including an overview of all the submodels used for this thesis. Section 2.3 focuses on the submodel which has been mostly modified and used during this study: the CLOUD submodel.

2.1 ECHAM5

ECHAM5 is the atmospheric GCM developed at the Max Planck Institute for Meteorology in Hamburg. Its original form comes from the weather prediction model of the European Centre for Medium-range Weather Forecasting (ECMWF), but it has been evolved in order to perform climate experiments. ECHAM5 version 5.3.02 has been used for this thesis. Its description below follows Roeckner et al. (2004).

The basic equations of atmospheric dynamics and thermodynamics are solved for the following prognostic variables: divergence (D), vorticity (ξ), temperature (T), mixing ratios (q) of different water species (water vapour, cloud liquid water, cloud ice), and the natural logarithm of the surface pressure ($\ln p_s$). While the mixing ratios are represented in a grid-point space, the other variables are represented in a spherical space.

Being the equations non-linear, they are horizontally discretized by applying the *transform method*, which computes space derivatives in spectral space, whereas non-linear products (including parameterizations) are evaluated in grid-point space. The basis functions for the spectral representation are the *spherical harmonics* (Y_n^m), i.e. the eigenfunctions of the Laplace equation in spherical coordinates which are used to describe any function on a sphere. They are a combination of sine and cosine functions (i.e. Fourier series) along the zonal direction and Legendre polynomials along the meridional direction. A triangular truncation (T) is applied to

Spectral resolution	Lat_G x Lon_G [# grid points]	Resolution [degrees]	Resolution [km]	Time step [s] ([min])
T21	32 x 64	5.62 x 5.62	626 x 626	2400 (40)
T31	48 x 96	3.75 x 3.75	417 x 417	1800 (30)
T42	64 x 128	2.81 x 2.81	313 x 313	1200 (20)
T63	96 x 192	1.87 x 1.87	209 x 209	720 (12)
T58	128 x 256	1.41 x 1.41	156 x 156	480 (8)
T106	160 x 320	1.12 x 1.12	125 x 125	360 (6)
T159	240 x 480	0.75 x 0.75	83 x 83	180 (3)

Table 2.1: Triangular truncations and associated Gaussian latitudes (and longitudes) with the corresponding horizontal resolutions and the maximum time step.

the superposition of spherical harmonics, with the advantage of making the horizontal spatial resolution uniform throughout the sphere. The horizontal resolutions possibly employed by ECHAM5 are (Table 2.1): T21, T31, T42, T63, T85, T106, and T159, where the number (M) is the truncation level (i.e. the maximum zonal wave number). The number of independent spherical harmonics is $M^2/2$ (Satoh, 2014).

On the other hand, the grid-point space is represented by a Gaussian grid. The Gaussian latitudes (Lat_G) associated to different spectral resolutions must fulfill the condition: $Lat_G = (3 \cdot M + 1)/2$, while the Gaussian longitudes (Lon_G) are usually twice Lat_G (Table 2.1).

Hybrid coordinates are used for the vertical discretization. They are defined by the pressures of the "half-levels" (i.e. the interface between the layer) which follow the terrain profile in the lower atmosphere and become pressure constant in the upper troposphere and stratosphere. Many vertical resolutions are possible. The standard one which focuses on the troposphere consists of 19 or 31 vertical layers (up to 10 hPa), while the one which extends to the middle-atmosphere has 39 or 90 layers (up to 0.01 hPa).

Time integration is performed by applying the *leapfrog scheme*, a semi-implicit time-centred integration scheme which has three time levels, i.e. it connects the values of a variable at three different time steps, $t-1$, t, and $t+1$ (Kalnay, 2002). This scheme is simple and accurate but produces an additional spurious solution (called "numerical mode"), thus, the Robert-Asselin time filter (Asselin, 1972) is applied. In order to garantee the stability of the solution (i.e. the solution must remain bounded as the time step tends to zero), the *Courant–Friedrichs–Lewy* (CFL) condition must be satisfied, so that a signal cannot travel more than one grid size in one time step (Courant et al., 1928). The flux form semi-Lagrangian scheme developed by Lin and Rockel (1996) is used for the advection of passive tracers, i.e. for the water components (vapour, liquid, solid) and chemical substances.

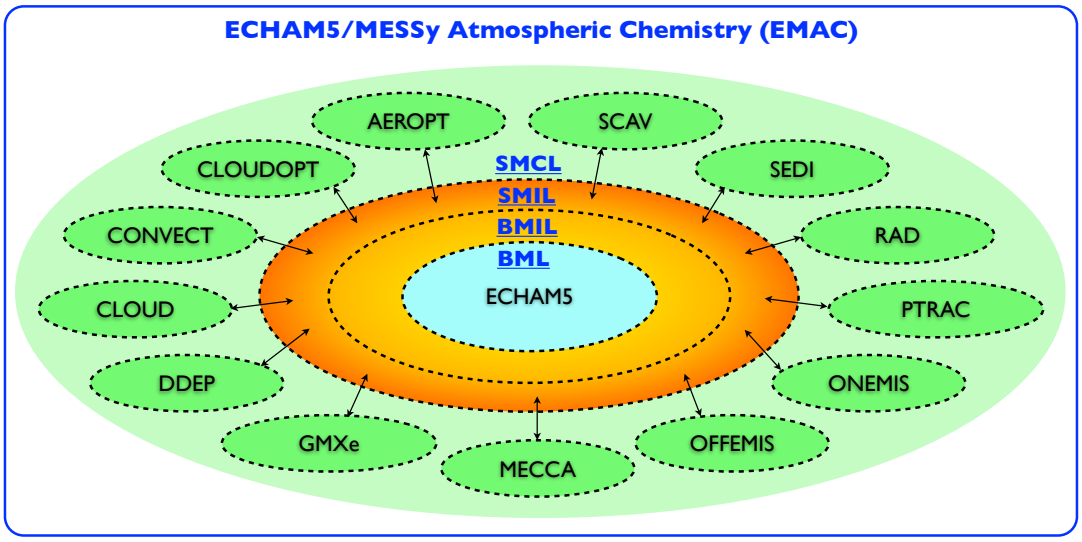

Figure 2.1: Process-oriented approach of MESSy and its four layers (BML, BMIL, SMIL, and SMCL) with some examples of submodels.

2.2 MESSy

The Modular Earth Submodel System (MESSy) is a modular interface structure which connects a base model to its submodels describing tropospheric and middle atmosphere processes and their interactions with ocean, land, and human influences (Jöckel et al., 2005). The fundamental idea is to realise a comprehensive Earth System Model (ESM) to simulate the couplings among different domains (i.e. atmosphere, hydrophere, cryosphere, lithosphere, pedosphere, biosphere, and anthroposphere) and their feedback mechanisms in a highly modularised way. MESSy can be implemented into any kind of model (box, regional, or global). In this thesis, MESSY (version 2.53) has been used in connection with ECHAM5, extending the GCM to a fully coupled chemistry-climate model: the EMAC model.

2.2.1 MESSy structure

MESSy adopts a *process-oriented approach* where each process is coded as a singular, independent entity (i.e. the submodel) and connected to a base model via a standard interface which allows to exchange information online (Jöckel et al., 2005). The modularity of MESSy allows to switch on/off each submodel individually and is particularly useful for the analysis of feedback mechanisms.

The structure of MESSy comprises four layers (Figure 2.1).

1. The *Base Model Layer* (BML) consists of a base model with all the modularised parts removed. ECHAM5 is the base model in EMAC.

2. The *Base Model Interface Layer* (BMIL) has three functionalities: *(a)* to allow the base model to control (i.e. to switch and call) the submodels, *(b)* to organise the data transfer

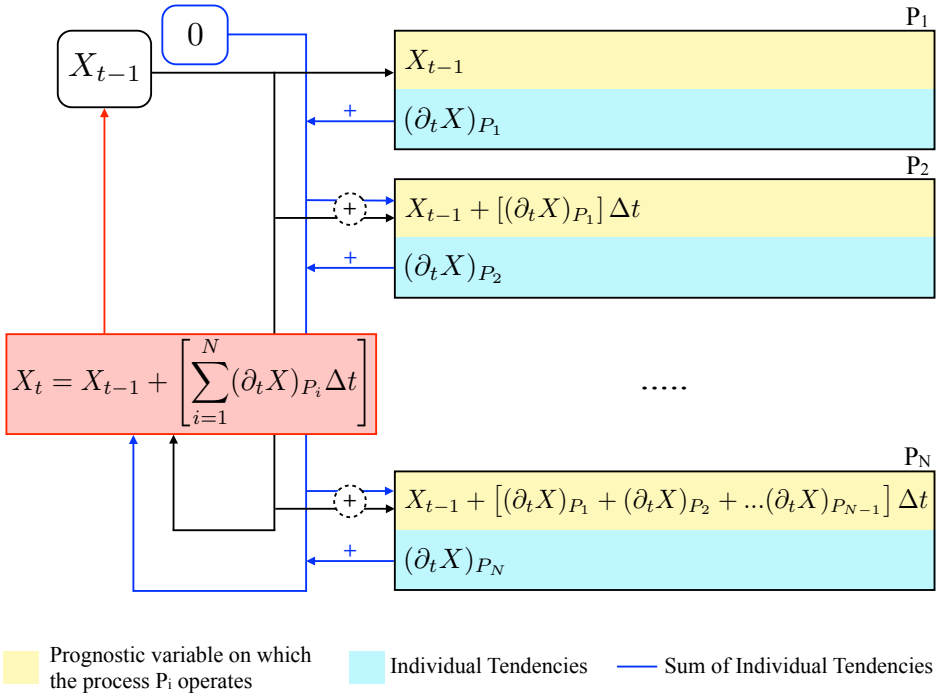

Figure 2.2: Operator splitting concept. $P_1, P_2, ...P_N$ are different processes (or submodels).

between the submodels and the base model and among different submodels, and *(c)* to import gridded initial and time dependent boundary conditions.

3. The *Submodel Interface Layer* (SMIL) transfers information from the BMIL to the core routines in the SMCL (see below) via parameter lists and, vice versa, distributes the calculated results back to the BMIL. SMIL also performs the couplings between different submodels.

4. The *Submodel Core Layer* (SMCL) includes the representation of the individual processes, i.e. the core routines of the submodels. The routines are self-consistent (i.e. the output is exclusively defined by its numerical input) and independent of the base model.

The fundamental method which enables the combination of individual processes (i.e. the coupling of different submodels) into one simulation is the so-called *operator splitting concept* (Jöckel, 2012; Eichinger and Jöckel, 2014). Following this method, the processes which modify a specific prognostic variable (X) occur in sequence: each process adds its individual contribution (*individual tendency*) to the overall change of X, which becomes the *total tendency* of X at the end of each integration time. As shown in Figure 2.2, the total tendency depends on *(a)* the sum of the individual tendencies determined by the previous processes which have operated in the same time step and *(b)* the initial value of X, $X(t = 0)$, or the state of X at one (or more) previous time step(s), $X(t - 1)$, according to the applied time integration scheme. At the end of the time step, the total tendency is given by the sum of all individual

Submodel	Function	Reference
AEROPT	Aerosol optical properties	Dietmüller et al. (2016)
AIRSEA	Air-sea exchanges of chemical species	Pozzer et al. (2006)
CLOUD	Large-scale clouds	Roeckner et al. (2004)
CLOUDOPT	Cloud optical properties	Dietmüller et al. (2016)
CONVECT	Convective clouds	Tost et al. (2006b)
CVTRANS	Convective transport of tracers	Tost et al. (2010)
DDEP	Dry deposition of gases and aerosols	Kerkweg et al. (2006a)
E5VDIFF	Turbulent vertical diffusion	Roeckner et al. (2004)
GMXe	Aerosol microphysics and gas/aerosol partitioning	Pringle et al. (2010)
JVAL	Photolysis rate coefficients	Sander et al. (2014)
LNOX	Lighting NO_x production	Tost et al. (2007)
MECCA	Tropospheric chemistry	Sander et al. (2011)
OFFEMIS	Offline emissions	Kerkweg et al. (2006b)
ONEMIS	Online emissions	Kerkweg et al. (2006b)
ORBIT	Orbital parameters	Dietmüller et al. (2016)
PTRAC	Prognostic tracers	Jöckel et al. (2008)
RAD	Radiative transfer	Dietmüller et al. (2016)
SCAV	Scavenging of gases and aerosol	Tost et al. (2006a)
SEDI	Aerosol sedimentation	Kerkweg et al. (2006a)
SURFACE	Surface processes	Jöckel et al. (2016)
TNUDGE	Tracer nudging	Kerkweg et al. (2006b)
TROPOP	Tropopause pressure	Jöckel et al. (2006)

Table 2.2: The MESSy submodels used in this thesis.

tendencies and it is added to the initial value of X. Then, the time integration scheme calculates the initial value of the prognostic variable for the next time step and resets the total tendency to zero. Mathematically, the individual tendency of X due to a particular process P_i is the partial time derivative of X and is indicated as $(\partial_t X)_{P_i}$. The total tendency, i.e. the total time derivative of X, is approximated by the sum of all partial derivatives: $\sum_{Pi} (\partial_t X)_{P_i}$. In this way, the temporal evolution of the prognostic variables is computed sequentially in several steps, and each step is determined by a submodel attributed to a specific process.

2.2.2 MESSy submodels

The MESSy submodels used in this thesis are listed in Table 2.2 and briefly described below.

AEROPT computes the optical properties of aerosols by using aerosol climatologies (offline mode) or concentrations and size distributions of aerosols simulated via an aerosol model, e.g. GMXe (online mode) (Lauer et al., 2007; Pozzer et al., 2012; Dietmüller et al., 2016). The

optical properties are: aerosol optical thickness (i.e. total extinction by scattering and absorption of aerosol particles in each grid box), single-scattering albedo (i.e. ratio of scattering over absorption by the aerosols), and asymmetry factor (which describes the angular distribution of scattering intensity). Aerosol property information is a necessary input for the radiation scheme.

AIRSEA computes the exchange of chemical constituents between ocean and atmosphere (Pozzer et al., 2006).

CLOUD describes large-scale (stratiform) clouds via cloud microphysical and cloud cover schemes. The original ones used in ECHAM5 are from Lohmann and Roeckner (1996) and Tompkins (2002), respectively. A more detailed description of CLOUD is presented in Section 2.3.

CLOUDOPT computes the optical properties of clouds (cloud optical depth, single scattering albedo, and asymmetry factor) in different solar spectral bands (four in the shortwave spectrum, sixteen in the longwave spectrum) to account for their wavelenght dependency (Dietmüller et al., 2016). Cloud property information is an input for the radiation scheme.

CONVECT includes multiple parameterizations to simulate convective clouds (Tost et al., 2006b). Convective cloud microphysics is solely based on temperature and updraught strength and does not take into account influences from aerosols in cloud droplet and ice crystal formation. The parameterisations mainly address the influence of the convective activity on larger circulation: the detrained water vapour is added to the large-scale water vapour field, while the detrained cloud condensate is used as a source term for the cloud condensate treated by the CLOUD submodel.
In this thesis, the scheme of Tiedtke (1989) with modifications by Nordeng (1994) has been used, which is the default for ECHAM5.

CVTRANS addresses the transport of tracers within convective clouds. It follows the bulk formulation of Lawrence and Rasch (2005) and collects the required updraught and downdraught air mass fluxes and the respective entrainment and detrainment rates from CONVECT (Tost et al., 2010).

DDEP calculates the process of dry deposition, i.e. the removal of gas molecules and aerosol particles from the atmosphere by means of turbulent transfers or uptake processes onto the terrestrial surface, in absence of precipitation or clouds (Kerkweg et al., 2006a). Dry deposition is a sink process which is applied at the lowermost model layer. Dry deposition fluxes (expressed in kg m^{-2} s^{-1}) for each species X (in the gas or aerosol phase) are computed online as:

$$F_{dep,X} = q_X \cdot \frac{M_X}{M_{air}} \cdot \frac{\Delta p}{g \Delta z} \cdot v_{d,X} \ ,$$

where q_X is the mixing ratio of X, M_X and M_{air} are the molar masses of X and dry air, respectively, g is the gravitational acceleration, Δp and Δz are the layer thickness in Pa and m, and $v_{d,X}$ is the dry deposition velocity of X.
Dry deposition velocities are computed according to the "big leaf approach" (Ganzeveld et al., 2006), i.e. considering the canopy or other surfaces as a bulk substrate (neglecting the different removal processes at different levels in the canopy). $v_{d,X}$ depends on the aerodynamic resistance (which is a function of the physical state of the atmosphere), the quasi-laminar boundary layer resistance (which is controlled by molecular diffusion), and the surface resistance (which depends on the chemical, physical, and biological properties of the surface). Given the influences of different surface properties, $v_{d,X}$ is actually the sum of individual dry deposition velocities defined for various types of surface.

E5VDIFF computes the vertical diffusion by turbulent motions of the following prognostic variables X: temperature, meridional wind, zonal wind, humidity, cloud liquid water, cloud ice, and tracers. Vertical turbulent fluxes ($\overline{w'X'}$) at the surface are derived from a bulk transfer relation, whose transfer coefficients are obtained from the Monin-Obukhov similarity theory. Above the surface, the eddy diffusion method is applied, i.e. $\overline{w'X'}$ is related to the vertical gradient of X through vertical eddy diffusion coefficients (Roeckner et al., 2004).

GMXe (Global Modal-aerosol eXtension) is an aerosol microphysics and gas/aerosol partitioning model (Pringle et al., 2010). It is a two-moment aerosol model which prognostically predicts the number concentration and the mass mixing ratio of the aerosol modes.
Aerosol microphysics is treated using an extended version of M7 (Vignati et al., 2004), which describes the aerosol size distribution ($n(\ln r)$, where r is the aerosol radius) using seven interacting *lognormal aerosol modes*. Therefore, $n(\ln r)$ is given by the sum of seven lognormal distributions:

$$n(\ln r) = \sum_{j=1}^{7} \frac{N_j}{\sqrt{2\pi}\ln\sigma_j} \exp\left(-\frac{(\ln r - \ln \bar{r}_j)^2}{2(\ln\sigma_j)^2}\right) ,$$

where N_j is the total number concentration, $\bar{r}_j$ is number mean radius, and σ_j is the geometric standard deviation of the jth lognormal aerosol mode. Soluble aerosols are distributed in four *hydrophilic modes* which cover the aerosol size spectrum of nucleation (NS, $r < 5$ nm), Aitken (KS, 5 nm $< r <$ 50 nm), accumulation (AS, 50 nm $< r <$ 500 nm), and coarse (CS, $r >$ 500 nm) modes. Insoluble aerosols are assigned to three *hydrophobic modes* (KI, AI, CI) which have the same size range, excluding the nucleation mode. The standard deviations are constant values, 1.59 and 2.0 only for CS and CI. The aerosol composition within each mode is uniform (*internally mixed*) but it varies among the modes (*externally mixed*).
GMXe simulates the microphysical aerosol processes of nucleation and coagulation. Nucleation of new particles is calculated as a function of temperature, relative humidity, and concentration of sulfuric acid (H_2SO_4) via two possible parameterizations (i.e. Kulmala et al., 1998, and Vehkamäki et al., 2002). Coagulation is determined for Brownian motion via the coagulation coefficients defined in Fuchs (1964). It can be intramodal (e.g. KS + KS $\rightarrow$ KS) or intermodal,

i.e. moving aerosols from smaller to larger modes (e.g. KS + AS → AS) or from hydrophobic to hydrophilic modes (e.g. AI + KS → AS).
The thermodynamic treatment of the gas/aerosol partitioning of semi-volatile inorganic species is performed in two stages. Firstly, GMXe calculates the amount of gas phase kinetically able to condense onto each aerosol mode (within a model time step), according to the volatility of the gas species. Secondly, the partitioning model (e.g. the thermodynamic equilibrium model of Fountoukis and Nenes, 2007, ISORROPIA-II) re-distributes the mass between the gas and the aerosol phases.
Other processes described in GMXe are: changes from hydrophobic to hydrophilic of *aged* aerosols (due to coagulation with soluble material or condensation of sulfuric acid), uptake of water vapour by hydrophilic aerosols, aerosol growth, and aerosol re-distribution between the modes (this is the final step of GMXe at each model time step).
Additionally, GMXe offers the flexibility to consider the emitted aerosols as *bulk* species, i.e. the aerosol chemical composition is unresolved (e.g. dust – DU, black carbon – BC, organic compound – OC, and sea salt – SS), or *speciated* species, i.e. the individual ions that compose an aerosol are simulated and then transported as tracers (e.g. Cl^-, Na^+, SO_4^{2-} for SS).

JVAL computes online the rate coefficients of different photolysis reactions in the atmosphere (Sander et al., 2014), according to the algorithm of Landgraf and Crutzen (1998).

LNOX calculates the production of NO_x resulting from lightning activity. It includes multiple parameterizations to compute the flash frequency (Tost et al., 2007). Since there are large uncertainties in the amount of NO_x produced by lightning, a scale factor is used to adjust the calculated amount within the expected range $2 - 8$ Tg N yr^{-1}.
In this thesis, the parameterization of Grewe et al. (2001) has been used, which links updraught velocity (indicator of the convective strength) and the associated cloud electrification with flash frequency.

MECCA (Module Efficiently Calculating the Chemistry of the Atmosphere) describes tropospheric and stratospheric chemistry (Sander et al., 2005, 2011). MECCA computes the rate coefficients of all the chemical reactions considered in the simulation, according to meteorological and chemical parameters, such as temperature, pressure, and tracer concentrations. Additionally, it uses the photolysis rates calculated by JVAL and the heterogeneous rate coefficients calculated by the HETCHEM submodel (Jöckel et al., 2006) for heterogeneous chemistry on aerosol surfaces. The ordinary differential equations associated to different chemical reactions are integrated by the KPP (Kinetic Preprocessor) software (Sandu and Sander, 2006) to determine the evolution of the atmospheric chemical components.
In this thesis, the stratosphere is excluded from the vertical domain, so only tropospheric chemistry is computed. The same chemical mechanisms to the base simulations in Jöckel et al. (2016) have been considered (see "CCMI-base-02.bat" in the supplement material of Jöckel et al., 2016), while aerosol climatologies have been used for heterogeneous chemistry.

OFFEMIS (OFFline EMISsions) manages the files which store pre-calculated emission fluxes of gas phase and aerosol species (Kerkweg et al., 2006b). It distinguishes three types of emission:

1. *surface emissions* (2-D, in molecules m^{-2} s^{-1}), which occur at the interface between land/ocean and atmosphere;
2. *multilayer emissions* (Nx2-D, in molecules m^{-2} s^{-1}), i.e. emissions which occur at the specific N-heights (defined in the namelist-file "import.nml") above the surface;
3. *volume emissions* (3-D, in molecules m^{-3} s^{-1}), which are vertically distributed along the vertical hybrid pressure levels (e.g. aircraft and volcanic emissions).

The offline emissions can be used by other submodels, not directly influencing the atmospheric chemical species (*method 0*), to compute the tracer tendency to be applied to the corresponding tracer field (*method 1*), or to compute the lower boundary conditions for the vertical diffusive fluxes of tracers (*method 2*, applicable only to 2-D fields).
By using the climatologies described in Section 4.1, the emissions of the following species have been offline simulated in this thesis: NO, CO, C_2H_4, C_2H_6, C_3H_6, C_3H_8, NC_4H_{10}, CH_3CHO, CH_3COCH_3, CH_3CO_2H, CH_3OH, HCHO, HCOOH, MEK, SO_2, NH_3 (from biomass burning, anthropogenic sources, aircraft emissions, biogenic sources, volcanic eruptions), DMS, NH_3, CH_3I, and halocarbons.

ONEMIS (ONline EMISsions) calculates the emissions of gas phase and aerosol tracers which depend on the actual state of the model (e.g. meteorological conditions and soil characteristics) at each model time step (Kerkweg et al., 2006b).
Emissions of soil-biogenic NO_x and the volatile organic compounds (i.e. isoprene and monoterpene) have been computed online in this thesis.

ORBIT computes the orbital variations which affect the total solar radiation incident the Earth and the temporal and spatial distribution of terrestrial insolation. The orbital variations, identified by Milankovitch (1941), are the obliquity of the Earth's axis, the eccentricity of the Earth's orbit around the Sun, and the precession of the equinoxes. Their representation can be based on precise orbit determination principles, to simulate short term variations of today's climate, or the Kepler's laws, for paleoclimate studies (Roeckner et al., 2004). Orbital parameters, such as distance of the Sun to the Earth, cosines of the zenith angle, and day length, are used by the radiation scheme (Dietmüller et al., 2016).

PTRAC enables the definition of additional prognostic tracers, in the gas or aerosol phase. Such tracers are defined in the namelist-file "ptrac.nml", on the contrary, usual tracers are defined in the TRACER submodel, and any change in their definition requires the recompilation of the code (Jöckel et al., 2008). Additionally, PTRAC can serve as a highly simplified aerosol model with aerosol properties constant in time and space. In this case, aerosols do not interact

with each other (as when they are described by GMXe) but behave as passive tracers which are transported and removed by physical sinks. The bioaerosols simulated in this thesis have been defined in this way.

RAD is largely based on the original ECHAM5 radiation code (Roeckner et al., 2004) and provides the temperature tendencies due to radiation. Shortwave and longwave radiative fluxes depend on scattering and absorption by *radiatively active species* (i.e. CO_2, O_3, CH_4, N_2O, $CFCl_3$, CF_2Cl_2), water vapour, cloud optical properties, cloud cover, aerosol optical properties, and orbital parameters (Dietmüller et al., 2016). The computations are solved for four spectral bands in the solar shorwave spectrum and sixteen bands in the terrestrial longwave spectrum. RAD can work using online computed tracers and online input variables (from the submodels AEROPT, CLOUDOPT, and ORBIT) or offline input variables (from IMPORT). As it is computationally expensive, RAD is called less frequently than the dynamics (i.e not at each model time step).
In this study, the original ECHAM5 aerosol climatology (Tanre et al., 1984) has been applied in combination with the climatology provided by the Chemistry–Cimate Model Initiative (CCMI, ftp://iacftp.ethz.ch/pub_read/luo/ccmi). Additionally, the radiatively active species have been nudged following the CCMI recommendations.

SCAV simulates the wet removal of trace gases and aerosol particles by large-scale and convective clouds and precipitation events (Tost et al., 2006a). Additionally, SCAV computes the aqueous phase chemistry in cloud droplets.
SCAV distinguishes two types of scavenging. *Nucleation scavenging* (NS) dissolves soluble species during the nucleation and growth of cloud droplets, while *impaction scavenging* (IS) removes both soluble and insoluble species after their impact with falling rain/cloud droplets and their uptake. In the uppermost layer where a cloud occurs, scavenging starts as NS. In the layer below, firstly IS due to the incoming precipitation flux is computed, then NS (in the same layer). Both processes are computed as long as there are clouds in the layers beneath; then, only IS is calculated until the ground level. In this way, the species incorporated in cloud droplets via NS can be removed from the atmosphere through precipitation, but they can be also released back into the atmosphere after cloud evaporation. Only the cloud covered/rainy part of the grid box contributes to the scavenging.
Scavenging can be computed via two different approaches: *(i)* using empirically determined, fixed scavenging coefficients (with the advantage of being computationally efficient), or *(ii)* solving a system of ordinary differential equations (taking into account feedback mechanisms between multiphase chemistry and transport processes).
The process of uptake and release of gases from cloud or rain droplets is formulated following the Henry's equilibrium law and a correction for gas phase diffusion limitation and accommodation coefficients. Scavenging of aerosols depends on Brownian motion (and on impaction in IS) and rainfall intensity. It is characterised by a minimum scavenging efficiency for aerosols with radius near 0.1 μm (called "scavenging gap" or "Greenfield gap" by Greenfield, 1957).

SEDI treats the sedimentation, i.e. the settling process due to gravity, of aerosol particles. Sedimentation takes place within the entire vertical model domain and is negligible for trace gases (Kerkweg et al., 2006a). SEDI computes the changes in aerosol concentration due to sedimentation according to the sedimentation theory presented in Pruppacher and Klett (1997), who defined the terminal sedimentation velocity ($v_{t,sed}$) for each mode (or bin) as:

$$v_{t,sed} = v_{Stokes} \cdot f_{Cunn} \cdot f_{Slinn} \ ,$$

where v_{Stokes} is the sedimentation velocity for spherical particles, f_{Cunn} is the Cunningham-slip-flow factor which corrects the aerodynamic differences due to non-spherical shapes, and f_{Slinn} is a correction applied when the modal aerosol representation is used, as the mean settling velocity of all particles of a lognormal mode is larger than the settling velocity of a particle with the mean radius (the correction is one for bin aerosol models).

SURFACE computes heat and water budgets of soil, water temperature, ice thickness and ice temperature of lakes, as described in Roeckner et al. (2004).

TNUDGE performs the nudging of user-defined tracers with (imported) prescribed fields. It is especially used when emission fluxes of specific tracers are highly uncertain or the tracer lifetime is sufficiently long (e.g. CH_4), so that the mixing ratios are well known (Kerkweg et al., 2006b).
In this thesis, the lower boundary conditions of the following tracers have been prescribed: N_2O, CH_4, CO_2, COS, CFCs, HCFCs, Halons, and H_2 using the AGAGE database (Prinn et al., 2000). Additionally, the radiatively active species have been nudged within the entire atmosphere.

TROPOP computes the tropopause height diagnostically according to various definitions (Jöckel et al., 2006). Additionally, TROPOP diagnoses the height of the planetary boundary layer.
In this thesis, the tropopause pressure is derived from the definition of the World Meteorological Organisation (WMO, 1992), based on the temperature lapse rate for latitudes equatorward of 30° and the potential vorticity iso-surface of 3.5 PVU for latitudes poleward of 30°.

2.3 The CLOUD submodel

The standard stratiform cloud scheme of ECHAM5 solves the governing equations for three prognostic variables (in kg kg^{-1}): specific humidity (q_v), cloud liquid water mixing ratio (q_w), and cloud ice mixing ratio (q_i). Cloud droplet number concentration (i.e. CDNC) and ice crystal number concentration (i.e. ICNC) are prescribed or determined by simple empirical functions, while rain and snow are treated diagnostically (Roeckner et al., 2004). Nevertheless, ECHAM developments have led to the introduction of a new prognostic equation for CDNC,

allowing for cloud droplet nucleation, advection, evaporation, and collision-coalescence and a more realistic estimation of CDNC (Lohmann et al., 1999). Later, Lohmann (2002) introduced a new prognostic equation for ICNC as well. Currently, the CLOUD submodel uses a double-moment stratiform cloud microphysics scheme (Lohmann et al., 1999; Lohmann, 2002; Lohmann et al., 2007b) which defines prognostic equations for the in-cloud variables q_v, q_w, q_i, CDNC, and ICNC. The usage of a two-moment scheme has the advantage of allowing for aerosol–cloud interactions, improving calculations of cloud microphysical processes and radiative transfer.

In the CLOUD submodel, ice crystals form via homogeneous nucleation in the cirrus regime and via immersion and contact nucleation in the mixed-phase regime (more details about ice nucleation are given in Subsection 2.3.2). The WBF process at subfreezing temperatures is parameterized, so liquid water is forced to evaporate from cloud droplets and deposit onto existing ice crystals. The cloud condensate detrained from convection (source term provided from the CONVECT submodel) is considered either liquid or ice depending on the temperature (if $T < -35°C$ the phase is ice) and the updraught velocity. The number of detrained ice crystals is estimated from the detrained ice condensate by assuming an only temperature dependent radius.

Cloud droplet formation is parameterized by the "unified activation framework" (UAF) (Kumar et al., 2011; Karydis et al., 2011). It is an advanced physically-based parameterization which merges two theories: the κ-Köhler theory (Petters and Kreidenweis, 2007), which governs the activation of soluble aerosols, and the Frenkel-Halsey-Hill adsorption activation theory (Kumar et al., 2009), which describes the droplet activation due to water adsorption onto insoluble aerosols (e.g. mineral dust). Aerosol modes that consist of only soluble material follow the κ-Köhler theory, and the required effective hygroscopicity (κ) is calculated on the basis of the chemical composition of the aerosol mode. Aerosol modes that consist of an insoluble core with soluble coating follow the UAF scheme, which takes into account the effects of adsorption and absorption on the CCN activity of the mixed aerosol. More details about the UAF scheme and its implementation in the EMAC model can be found in Karydis et al. (2017).

The diagnostic cloud cover scheme of Sundqvist et al. (1989) based on the grid-mean relative humidity is used. Such scheme assumes that a grid box is partially covered by clouds when the relative humidity exceeds a threshold and is totally covered when water saturation is reached. Other microphysical processes, such as phase transitions, autoconversion, aggregation, and accretion, are also taken into account by the CLOUD submodel (further details about ice crystal related processes are given in Subsection 2.3.1).

In the CLOUD submodel, a single updraught velocity (w) is used for the whole grid cell, although w can strongly vary in reality within the cell horizontal dimension (e.g. Guo et al., 2008). This is a simplification which is commonly used by GCMs. In EMAC, the subgrid-scale variability of vertical velocity (w_{sub}) is introduced by a turbulent component which depends on the subgrid-scale turbulent kinetic energy (TKE) described by Brinkop and Roeckner (1995), such that $w_{sub} = 0.7\sqrt{TKE}$. Hence, the vertical velocity is given by the sum of the grid-mean

vertical velocity resolved by the model ($\overline{w}$) and the turbulent contribution: $w = \overline{w} + w_{sub}$ (Lohmann and Kärcher, 2002). Kärcher and Ström (2003) and Joos et al. (2008) showed that such a representation of w is in good agreement with vertical velocity observations. Zhou et al. (2016) analysed the effects of different updraught velocity representations and showed that using w_{sub} overestimates the ICNCs at temperatures below −70°C, but agrees better with the observations at higher temperatures.

An evaluation of the double-moment cloud microphysics scheme of ECHAM5 was presented in Lohmann et al. (2007b), Lohmann et al. (2008), and Lohmann and Hoose (2009), applying the two-moment aerosol microphysics scheme HAM (Stier et al., 2005). Lauer et al. (2007) and Righi et al. (2016) evaluated the CLOUD submodel in conjunction with the aerosol microphysics submodel MADE (Ackermann et al., 1998), while Tost (2017) evaluated it in combination with the GMXe submodel. The comparison of CLOUD with observations will be extended in Chapter 4.

2.3.1 The ICNC prognostic variable

As far as the ice phase is concerned, the EMAC model solves the prognostic equations for q_i as well as ICNC, so the first two moments of the ice crystal size distribution are predicted (see Subsection 1.2.1).

According to Lohmann (2002) and Roeckner et al. (2004), the prognostic equation for ICNC is:

$$\frac{\partial \mathrm{ICNC}}{\partial t} = R_{transp} + R_{sedi} + R_{ncir} + R_{nmix} + R_{secp} - (R_{self} + R_{aggr} + R_{accr} + R_{melt} + R_{subl}) \quad (2.1)$$

where the R-terms represent the rates of advective, turbulent, and convective transport (R_{transp}), sedimentation (R_{sedi}), ice nucleation in the cirrus regime (R_{ncir}), ice nucleation in the mixed-phase regime (R_{nmix}), secondary ice production (R_{secp}), self-colletion (R_{self}), aggregation (R_{aggr}), accretion (R_{accr}), melting (R_{melt}), and sublimation (R_{subl}) of ice crystals (ICs). Transport as well as sedimentation are computed from grid-mean values ($\overline{\mathrm{ICNC}}$), while the other terms are calculated from in-cloud values ($\mathrm{ICNC}_{\text{in-cloud}}$). The latter ones are related to the grid-mean values via the fractional cloud cover (f_C): $\mathrm{ICNC}_{\text{in-cloud}} = \overline{\mathrm{ICNC}}/f_C$.

The CLOUD submodel computes the rates associated to the physical and microphysical processes. Sedimentation is formally treated like vertical advection, while all the microphysical processes are computed with different parameterizations. Secondary ice production occurs via the Hallet-Mossop process (or rime splintering) as described in Levkov et al. (1992). Self-collection, aggregation, and accretion of ICs follow Lin et al. (1983) and Levkov et al. (1992). (It must be noted that the self-collection influences ICNCs but does not affect the cloud mass, so it would not be considered in one-moment schemes.) Sublimation of ice is computed like in Lin et al. (1983), while it is assumed that ICs melt as soon as $T > 0$°C. More information can be found in the cited works and references therein, while the ice nucleation parameterizations are described in the next subsection.

2.3.2 Ice nucleation parameterizations

In the CLOUD submodel, ice nucleation is computed via independent parameterizations in the two cloud regimes. In the cirrus regime, it is assumed that cirrus clouds form exclusively homogeneously using the parameterization of Kärcher and Lohmann (2002b) (hereafter referred to as KL02). In the mixed-phase regime, heterogeneous nucleation occurs via immersion and contact nucleation as described in Lohmann and Diehl (2006) (hereafter referred to as LD06).

KL02 is a physically-based parameterization which analytically solves the parcel model equations governing ice nucleation and ice crystal growth. KL02 parameterizes homogeneous nucleation of supercooled aerosols in an adiabatically rising air parcel at $T < -38°C$ on the basis of the experimental studies of Koop et al. (2000), so it is applicable to a wide class of aqueous solutions relevant to homogeneous nucleation in the atmosphere. KL02 treats the number of new ICs formed homogeneously ($N_{i,hom}^{NEW}$) as a function of updraught velocity, temperature, and aerosol size distribution. Indeed, higher vertical velocities create higher ice supersaturation, allowing more particles to freeze before the supersaturation is depleted. The lower the temperature, the more particles freeze, as the growth rate decreases when temperature decreases (Pruppacher and Klett, 1997) and water vapour depletion is slower. Finally, aerosol size effects are important when the timescale of nucleation is fast compared to the timescale of depositional growth. Thus, KL02 includes two different regimes: the *fast growth regime* and the *slow growth regime*. In the first regime, the growth of ICs is fast so that the memory about the initial size of aerosol particles is lost and the number of new ICs is insensitive to the aerosol size distribution. In this case, the freezing of new ICs occurs over an extended period of time. Vice versa, in the slow growth regime the IC growth is slow, the aerosol size effects are taken into account, and all particles freeze suddenly and almost simultaneously.

KL02 abandons the saturation adjustment scheme (see Subsection 1.2.3) to obtain a more realistic description of ice crystal formation. In fact, differently to cloud droplet activation, ice nucleation requires high levels of ice supersaturation. Moreover, the growth rate can be quite long (e.g. many hours) at very low temperatures ($T < -70°C$), therefore, equilibrium may not be reached within the model time step and ice supersaturation can persist.

KL02 needs the following variables as input: ice saturation ratio, updraught velocity, temperature, pressure, and number concentration and radius of soluble aerosols. The output variables of KL02 are the number concentration and radius of the newly-formed ICs. It must be mentioned that the influence of the pre-existing ice particles is not taken into account; the number of aerosol particles available for ice nucleation in the cirrus regime is simply reduced by the existing ice particle number.

In the mixed-phase regime, the concentration of the new ICs formed via immersion ($N_{i,imm}^{NEW}$) and contact ($N_{i,cnt}^{NEW}$) nucleation are computed following LD06. It is an empirical parameterization derived from laboratory observations of artificial drops. Both black carbon and mineral

dust, assumed to be composed of either kaolinite or montmorillonite, are considered INPs. Insoluble aerosols can initiate contact nucleation, while soluble aerosols are responsible for immersion nucleation. Contact nucleation follows Levkov et al. (1992) and depends on the concentration and radius of supercooled liquid droplets, the concentration of contact nuclei, and the Brownian aerosol diffusivity (which is temperature dependent). Immersion nucleation is parameterized according to Diehl and Wurzler (2004) and depends on the number of immersion nuclei and temperature (exponentially). The dependency of ice nucleating ability on aerosol size is neglected in both parameterizations.

In the current operational version of EMAC, it is assumed that dust is only composed by montmorillonite, representing a more efficient INP than a kaolinite dust particle. Moreover, contact nucleation by black carbon is excluded. Thus, black carbon takes part only in immersion nucleation, while dust both in immersion and contact nucleation.

Chapter 3

The newly-implemented ice nucleation parameterization

The ice nucleation parameterization of Barahona and Nenes (2009b) has been implemented in the EMAC model in order to improve the representation of the ice nucleation mechanisms in the cirrus and in the mixed-phase regimes. This chapter describes the BN09 parameterization in Section 3.1 and its implementation in Section 3.2.

3.1 Parameterization of Barahona and Nenes (2009)

The parameterization of Barahona and Nenes (2009b) (hereafter referred to as BN09) is a comprehensive, physically-based parameterization of new ice crystal formation. It provides an analytical solution of the cloud parcel model equations and is computationally efficient and suitable for large-scale atmospheric models. BN09 resolves the dependency of ice nucleation on ambient conditions (i.e. temperature, pressure, relative humidity, and vertical updraught) and chemically-heterogeneous, polydisperse aerosols acting as INPs. Additionally, it explicitly considers the competition for water vapour between homogeneous and heterogeneous nucleation in the cirrus regime. BN09 builds upon the schemes of Barahona and Nenes (2008) (hereafter called BN08) for homogeneous nucleation and Barahona and Nenes (2009a) for the competition between homogeneous and heterogeneous nucleation given a monodisperse aerosol population.

BN09 allows for the use of five different heterogeneous nucleation parameterizations, defined by Meyers et al. (1992), Phillips et al. (2007), Phillips et al. (2008), Phillips et al. (2013), and Barahona and Nenes (2009b). They are all empirically based except the latter one, which is derived from the CNT. The sensitivity studies in Barahona et al. (2010) and Sullivan et al. (2016) have shown that global means of ICNCs vary up to a factor twenty according to the INP parameterization used (when the competition between homogeneous and heterogeneous nucleation is taken into account). Moreover, empirically-based parameterizations better agree with the observations, while the CNT overestimates the number of ice crystals. Phillips et al.

(2008) showed that their parameterization (hereafter referred to as PDA08) is closer to the observations than the other schemes considered in their study (e.g. Meyers et al., 1992, and LD06). The simulations run for this thesis use the parameterization of Phillips et al. (2013) (hereafter referred to as P13) to simulate heterogeneous nucleation, as P13 is a development of PDA08 and well agrees with the observations (as remarked in Subsection 3.1.2).

Overall, BN09 takes into account processes which are neglected by the parameterizations KL02 and LD06, i.e. the water vapour competition in the cirrus regime, the influence of polydisperse aerosols (up to four different components using P13), and the PREICE. Additionally, P13 simulates both immersion/condensation and deposition nucleation and is built on field measurements of natural samples, not on laboratory experiments like LD06. Homogeneous nucleation and water vapour competition between the ice nucleation mechanisms is described in the next subsection, while P13 is described in Subsection 3.1.2.

3.1.1 Homogeneous nucleation

Homogeneous ice nucleation in BN09 is treated as a stochastic process and described via the CNT (see Subsection 1.1.1). The theory implies that freezing of a perfectly monodisperse droplet population results in a polydisperse ice crystal population, thus, extending the case to a polydisperse droplet population, the overall ice crystal distribution is given by the superposition of all ice crystal distributions.

As predicted by the physically-based parameterizations derived from CPMs (e.g. Kärcher and Lohmann, 2002a), the evolution of the ice crystals within an adiabatically rising air parcel is governed by the following *supersaturation balance equation*:

$$\frac{dS_i}{dt} = AS_i w - B\frac{dq_i}{dt} \ , \tag{3.1}$$

where w is the updraught velocity, dq_i/dt is the rate of water vapour deposition on ice crystals (q_i is the ice mixing ratio of the parcel), A and B are two temperature-pressure dependent parameters. The equation describes the competition between the S_i generation because of the cooling of the parcel rising with w (first term on the right-hand side of the equation) and the S_i reduction due to depositional growth of ice crystals (second term on the right-hand side). The maximum ice supersaturation (s_{max}) is derived from the condition $dS_i/dt = 0$.

The BN09 algorithm operates differently at temperatures below or above the threshold of $-35°$C (Figure 3.1). When $T < -35°$C, the algorithm can be divided in three subsequent parts.

Step 1 The limiting number of active INPs needed to inhibit homogeneous nucleation (N_{lim}) is computed. Indeed, at temperatures below $-35°$C, homogeneous and heterogeneous nucleation compete for water vapour, decreasing the ice supersaturation. When the number of active INPs exceeds N_{lim} and s_{max} is less than the threshold for homogeneous nucleation (s_{hom}), homogeneous nucleation is suppressed, and ice crystals are formed only heterogeneously. N_{lim} is determined by computing the number of INPs required to keep s_{max} below s_{hom}.

Step 2 The number concentration of ice crystals nucleated heterogeneously ($N_{i,het}$) is computed via the selected INP parameterization at s_{hom}; then, two cases can follow.
If the condition $N_{i,het}(s_{hom}) \geq N_{lim}$ is satisfied, ice crystals are formed only heterogeneously at s_{max} (i.e. $N_{i,het}(s_{max})$), as homogeneous nucleation is suppressed. s_{max} is determined using a bisection method to balance the supersaturation within the air parcel (equation 3.1).
If $N_{i,het}(s_{hom}) < N_{lim}$, the competition for water vapour between homogeneous and heterogeneous nucleation is simulated. The concentration of the new ice crystals nucleated homogeneously ($N_{i,hom}$) is determined via the homogeneous nucleation parameterization of Barahona and Nenes (2008, 2009b) (hereafter called BNhom):

$$\begin{aligned} f_c &= f_{c,hom}\left[1-\left(\frac{N_{i,het}(s_{hom})}{N_{lim}}\right)^{3/2}\right]^{3/2} \\ N_{i,hom} &= N_c e^{-f_c}(1-e^{-f_c}) \end{aligned}$$

where N_c is the number concentration of activated liquid cloud droplets, f_c (from Barahona and Nenes, 2009b) and $f_{c,hom}$ (from Barahona and Nenes, 2008) are the fractions of frozen droplets at s_{hom} with and without the presence of INPs, respectively.

Step 3 The total concentration of the new ice crystals formed in the cirrus regime ($\mathrm{N}_{\mathrm{i,cirrus}}^{\mathrm{NEW}}$) is determined by the contribution of both heterogeneous and homogeneous nucleation, i.e. $\mathrm{N}_{\mathrm{i,cirrus}}^{\mathrm{NEW}} = N_{i,het} + N_{i,hom}$.

On the other hand, when $T > -35°\mathrm{C}$, the algorithm uses the INP parameterization to compute $N_{i,het}(s_{max})$ (see the next subsection). Therefore, the number concentration of the new ice crystals in the cirrus regime is:

$$\mathrm{N}_{\mathrm{i,cirrus}}^{\mathrm{NEW}} = \begin{cases} N_{i,het}(s_{hom}) + N_{i,hom} & N_{i,het}(s_{hom}) < N_{lim},\ s_{max} = s_{hom} \\ N_{i,het}(s_{max}) & N_{i,het}(s_{hom}) \geq N_{lim},\ s_{max} < s_{hom} \end{cases}$$

while the concentration of the new ice crystals in the mixed-phase regime is:

$$\mathrm{N}_{\mathrm{i,mix}}^{\mathrm{NEW}} = N_{i,het}(s_{max})\ .$$

As mentioned before, P13 has been used to compute $N_{i,het}$. Since P13 simulates the new ice crystals formed via deposition and immersion/condensation nucleation modes, $N_{i,het}$ is also indicated as $\mathrm{N}_{\mathrm{i,imm}}^{\mathrm{NEW}}$ (like in Figure 3.2 and equation 3.3).

In order to account for subgrid-scale variabilities, the output variables of BN09 which depend on the vertical velocity ($f(w)$) are weighted over a Gaussian probability density function of updraught velocities ($P(w)$, with mean 0.1 cm s^{-1} and standard deviation equal to w_{sub}) by numerically calculating the integral (Morales and Nenes, 2010; Sullivan et al., 2016):

$$\overline{f(w)} = \frac{\int_0^\infty f(w')P(w')dw'}{\int_0^\infty P(w')dw'}\ . \tag{3.2}$$

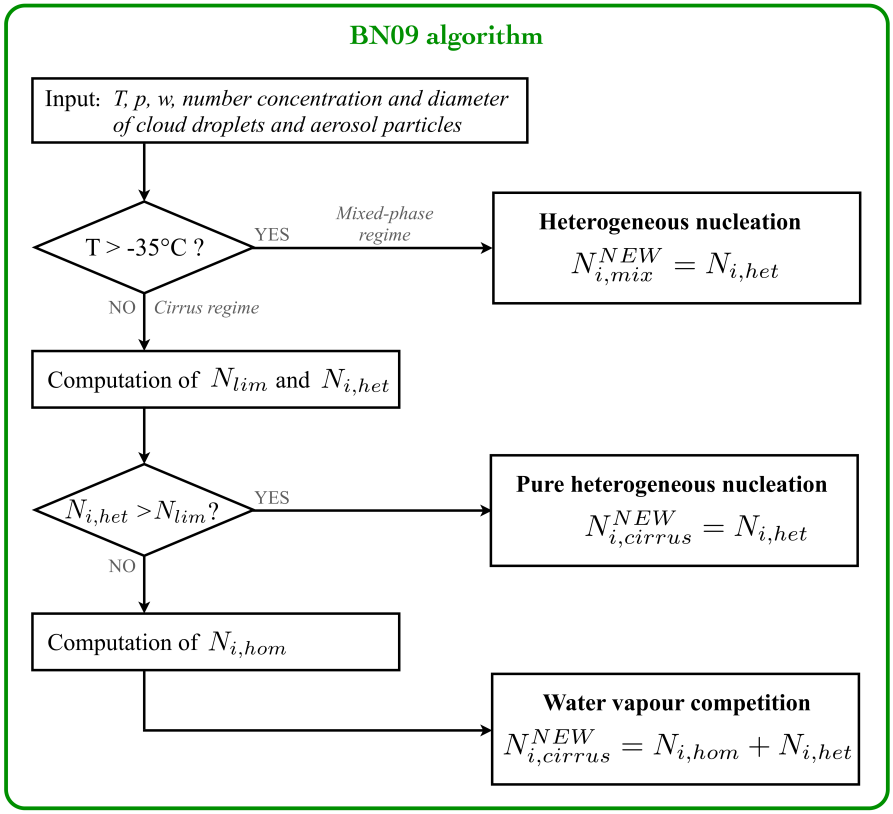

Figure 3.1: Algorithm of BN09.

3.1.2 Heterogeneous nucleation (Phillips et al. 2013)

The P13 parameterization for heterogeneous ice nucleation is empirically derived and depends on the chemistry and surface area of multiple aerosol types. P13 computes ice nucleation in immersion/condensation and deposition mode and contact mode and assumes that each active INP can nucleate ice either by one or the other mode depending on local temperature and relative humidity. Four basic groups of INPs are defined: insoluble dust (DU), black carbon (BC), and primary biological aerosol particles (PBAPs), and soluble organics (OC). PBAPs (or BIO) are assumed not to be diversified in individual species, like bacteria, fungal spores, and pollen.

The parameterization is based on the singular hypothesis (see Subsection 1.2.2), so the active INPs freeze instantaneously as soon as they reach their characteristic freezing temperature. P13 relies on the fundamental assumption that the number of active INPs of one particular aerosol group is proportional to the total aerosol surface area of that group, at any given value of ice supersaturation. Such assumption, which is observational supported, derives from a strong theoretical basis. Surface active sites have a certain probability of occurrence per unit area within a given INP species. They depend on the particle history and chemical composition (Pruppacher and Klett, 1997) and form ice embryos at specific onset temperatures. It is assumed that larger INPs have more and better active sites than smaller ones and, thus, a higher nucleation efficiency. Therefore, the aerosol freezing fraction is related

to the density of active nucleation sites and to the surface area and number concentration of the aerosol population. More specifically, the concentrations of the new ice crystals from each aerosol group are based on INP measurements at reference conditions which are then adjusted by the simulated aerosol surface area, temperature, and ice supersaturation to account for regional and seasonal variations.

P13 has been validated against laboratory and field observations (Phillips et al., 2013). The comparison with flight measurements showed a net dominance of black carbon as active INP predicted by P13 in two out of five flights, while dust was the dominant INP in the other three flights. The active INPs derived from PBAPs were predicted to be $\sim 5\%$, in agreement with the observations. In the comparison with other INP parameterizations, Phillips et al. (2008) showed that their empirical parameterization PDA08 predicts active INP concentrations always lower of (about) two orders of magnitude than LD06 at $T < -15°C$.

The advantages of using P13 are multiple. P13 *(a)* reflects the diversity of INP chemistry (it is not a merely function of temperature and ice supersaturation like most of the previous parameterizations), *(b)* is based on natural INPs sampled from the background free troposphere (it is not derived from laboratory observations or the CNT), *(c)* represents the scarcity of heterogeneous nucleation at humidities well below water saturation for warm subzero temperatures (i.e. $T > -40°C$), and *(d)* represents all known modes of heterogeneous ice nucleation. Actually, the P13 algorithm implemented in EMAC does not include contact nucleation. It simulates only the immersion/condensation and deposition mode (described below), so contact nucleation is simulated via LD06 (see Subsection 2.3.2).

Immersion/condensation and deposition ice nucleation.
A *reference activity spectrum* ($n_{INP,*}$) is defined as the average number concentration of active INPs at water saturation associated to a background-troposphere scenario, i.e. it is assumed to be representative of the background state of the free troposphere. $n_{INP,*}$ is constructed from field observations of aerosols with (dry) diameters less than 1 μm performed with the CFDC. It grows exponentially with the ice saturation ratio and receives the contributions from the four aerosol groups: $n_{INP,*} = \sum_X n_{INP,X,*}$, where X =DU, BC, OC, BIO. The scarcity of heterogeneous ice nucleation in substantially subsaturated conditions is empirically determined and described through the fraction term $H_X(S_i, T)$. This satisfies the condition $0 \leq H_X \leq 1$ ($H_X = 1$ at water saturation) and its values depend on certain thresholds of temperature ($T_{0,X,min}$) and ice saturation ratio ($S_{i,0,X,min}$), see Table 3.1. Another important quantity is the *mean number of activated ice embryos per insoluble aerosol particle with diameter* D_X:

$$\mu_X(D_X, S_i, T) = H_X(S_i, T)\xi(T)\left(\frac{\alpha_X n_{INP,*}}{\Omega_{X,*}}\right)\pi D_X^2 \ ,$$

where:

- $\xi(T)$ (with $0 \leq \xi \leq 1$) is a factor which takes into account the observation that drops containing INPs are not seen to freeze at temperature higher than a certain threshold ($T_{X,max}$); thus, $\xi(T_{X,max}) = 0$ and $\xi(T_{X,max} - \Delta T_X) = 1$, with a cubic interpolation in

between.

- α_X is the fractional contribution of X to the active INP concentrations in the background-troposphere scenario (when $H_X = 1$), i.e. the portion of aerosol number belonging to X within $n_{INP,*}$ inferred from CFDC data. The fractions α_X are assumed to be constant (see Table 3.1), although they could depend on temperature and humidity.
- $\Omega_{X,*}$ is the total surface area of all aerosols with dry diameters between 0.1 μm and 1 μm in the background-troposphere scenario in the group X.
- $\pi D_X^2 = \Omega_X$ is the total surface area of all aerosols with dry diameters > 0.1 μm in the group X.

The number concentration of active INPs derived from the groups $X = \mathrm{DU, BC, BIO}$ is defined as:

$$n_{INP,X} = \int_{\log(0.1\mu\mathrm{m})}^{\infty} \left[1 - e^{-\mu_X(D_X,S_i,T)}\right] n_X(\log D_X) d\log D_X \ ,$$

where $n_X(\log D_X)$ is the aerosol size distribution of the group X. The concentration of active INPs derived from soluble organics ($X = \mathrm{OC}$) is computed differently and only in the cirrus regime:

$$n_{INP,OC} \approx \frac{H_{OC}(S_i,T)\ g_{glass}\ n_{INP,OC,*}\ \Omega_{OC}}{\Omega_{OC,*}} \ ,$$

where:

- g_{glass} is the maximum fraction of soluble organic aerosols that can be glassy (it is fixed at 0.5 according to Murray et al., 2010);
- $n_{INP,OC,*}$ is the reference activity spectrum for soluble organics defined with AIDA chamber experiments;
- $\Omega_{OC,*}$ is the baseline surface area of all soluble organic aerosols with dry diameters > 0.1 μm defined with AIDA chamber experiments;
- Ω_{OC} is the total surface area of all soluble organic aerosols with dry diameters > 0.1 μm.

In the end, the number concentration of the new ice crystals formed heterogeneously through immersion/condensation and deposition nucleation is given by the sum of all groups X:

$$N_{i,het}\left(= \mathrm{N}_{\mathrm{i,imm}}^{\mathrm{NEW}}\right) = \sum_X n_{INP,X} \tag{3.3}$$

For the sake of clarity, it must be said that the P13 code implemented in EMAC does not include all the developments done for the BC group in Phillips et al. (2013), with respect to Phillips et al. (2008). Indeed, the effect of organic coatings on BC particles, which smother the INP activity, is neglected in the definition of $S_{i,0,BC,min}$. Moreover, it is assumed that all BC particles have the same propensity for ice nucleation and α_{BC} is kept constant (like in Phillips et al., 2008), although Phillips et al. (2013) introduced a factor to take into account the fact that ice nucleation ability of BC greatly varies with its source.

Variable	DU	BC	OC	BIO	Description
$T_{0,X,min}$ [°C]	-40	-50	-75	-20	Lower thresholds of T in H_X
$\Delta T_{0,X}$ [°C]	5	10	10	5	T-interval in H_X: $T_{0,X,min} + \Delta T_{0,X} = T_{0,X,max}$
$S_{i,0,X,min}$ [−]	$1 + 10^y$	1.3	1.2	1.15	Lower threshold of S_i in H_X
$\Delta S_{i,0,X}$ [−]	0.1	0.1	0.1	0.2	S_i-interval in H_X: $S_{i,0,X,min} + \Delta S_{i,0,X} = S_{i,0,X,max}$
$T_{X,min}$ [°C]	-30	-25	/	-5	Lower thresholds of T in ξ
ΔT_X [°C]	20	10	/	3	T -interval in ξ: $T_{X,min} + \Delta T_X = T_{X,max}$
α_X	2/3	$1/3 - 0.03$	/	0.03	Fractional contribution of X to $n_{INP,*}$
$\Omega_{X,*}$ $[m^2/kg]$	$2.0 \cdot 10^{-6}$	$1.0 \cdot 10^{-7}$	$5.6 \cdot 10^{-5}$	$8.9 \cdot 10^{-7}$	Surface area of aerosols with dry diameters 0.1 μm $\div$ 1 μm for X = DU, BC, BIO and $>$ 0.1 μm for X = OC

Table 3.1: Some parameters defined in the P13 parameterization (see Phillips et al., 2008, and Phillips et al., 2013, for a complete list).

3.2 Implementation

The BN09 parameterization has been implemented within the MESSy framework in order to compute the newly-formed ice crystals. The BN09 code constitutes a new Fortran95 module in SMCL (named "messy_cloud_ice_BN09.f90") which can be called by the CLOUD submodel (i.e. the file "messy_cloud_lohmann10.f90") twice, to operate in the cirrus regime and/or in the mixed-phase regime. As shown in Figure 3.2, BN09 computes the new ice crystals nucleated in the cirrus regime when "nicnc=3" and in the mixed-phase regime when "limm_BN09 = .TRUE." (where nicnc and limm_BN09 are variables defined in the namelist-file "cloud.nml"). CLOUD in SMIL has been modified in order to compute also the number concentrations of OC and BIO, besides DU and BC, following the approximations of Hoose et al. (2008b), necessary because aerosols are an external mixture of internally mixed modes.

The output variables of BN09 are the number concentration and the radius of the new ice crystals. The input variables are:

- temperature (T [K]);
- pressure (P [Pa]);
- width of the vertical velocity distribution (w_{sub} $\left[\text{m s}^{-1}\right]$), with upper limit 3 m s^{-1} and lower limit 0.001 m s^{-1};
- number concentrations of activated cloud droplets (N_c $\left[\text{m}^{-3}\right]$);
- diameters (D_c [m]) and standard deviations (σ_c) of aerosols in the soluble Aitken mode;
- number concentrations (N_X $\left[\text{m}^{-3}\right]$), geometric mean dry diameters (D_M [m]), and log-normal standard deviations (σ_M) of interstitial aerosols of the species X (which can be

DU, BC, OC, BIO, depending on the choice of the INP parameterization in BN09) in the aerosol modes M (Aitken (K), accumulation (A), coarse (C), i.e. $M = K, A, C$).

The original BN09 algorithm computes N_c starting from the number concentration of sulfate aerosols in the Aitken mode. However, this option has been removed since the EMAC model can compute N_c via other parameterizations (Abdul-Razzak and Ghan, 2000; Lin and Leaitch, 1997; Karydis et al., 2017), hence, BN09 has been provided with such variable. Nevertheless, these parameterizations do not compute the diameter of the new cloud droplets, therefore, BN09 still computes D_c using the diameter of aerosols in the soluble Aitken mode. Given the internally mixed representation of aerosols in EMAC, the diameters D_M are not distinguished among aerosol types but only among the modes which the aerosol belong to. Similarly, the standard deviations σ_M are constant and depend only on the mode (in GMXe, $\sigma_K = \sigma_A = 1.59$ and $\sigma_C = 2.0$).

During the implementation, the PREICE has been included in the BN09 code. Pre-existing ice crystals act to decrease relative humidity by consuming any water vapour above ice saturation and compete with the updraught velocity, which acts to increase the relative humidity by cooling the air parcel through adiabatic expansion. Therefore, the PREICE can be parameterized by reducing the vertical velocity for ice nucleation (i.e. w_{sub}) by a factor depending on the pre-existing ice crystal number concentration ($\mathrm{ICNC_{pre}}$), so limiting the expansion cooling. Such "corrected" vertical velocity ($w_{sub,pre}$) has been computed as defined in Barahona et al. (2014):

$$w_{sub,pre} = w_{sub} \cdot \max\left[1 - \frac{\mathrm{ICNC_{pre}}}{w_{sub}} A(T) B(s_{hom}) C \; ; \; 0\right],$$

where $A(T)$ is a temperature-dependent parameter, $B(s_{hom})$ is a s_{hom}-dependent factor, and C is a constant.

Additionally, since the CLOUD submodel uses the value -35°C as temperature threshold between the two cloud regimes, the original threshold of BN09 (which was -38°C) has been converted to the value -35°C for consistency.

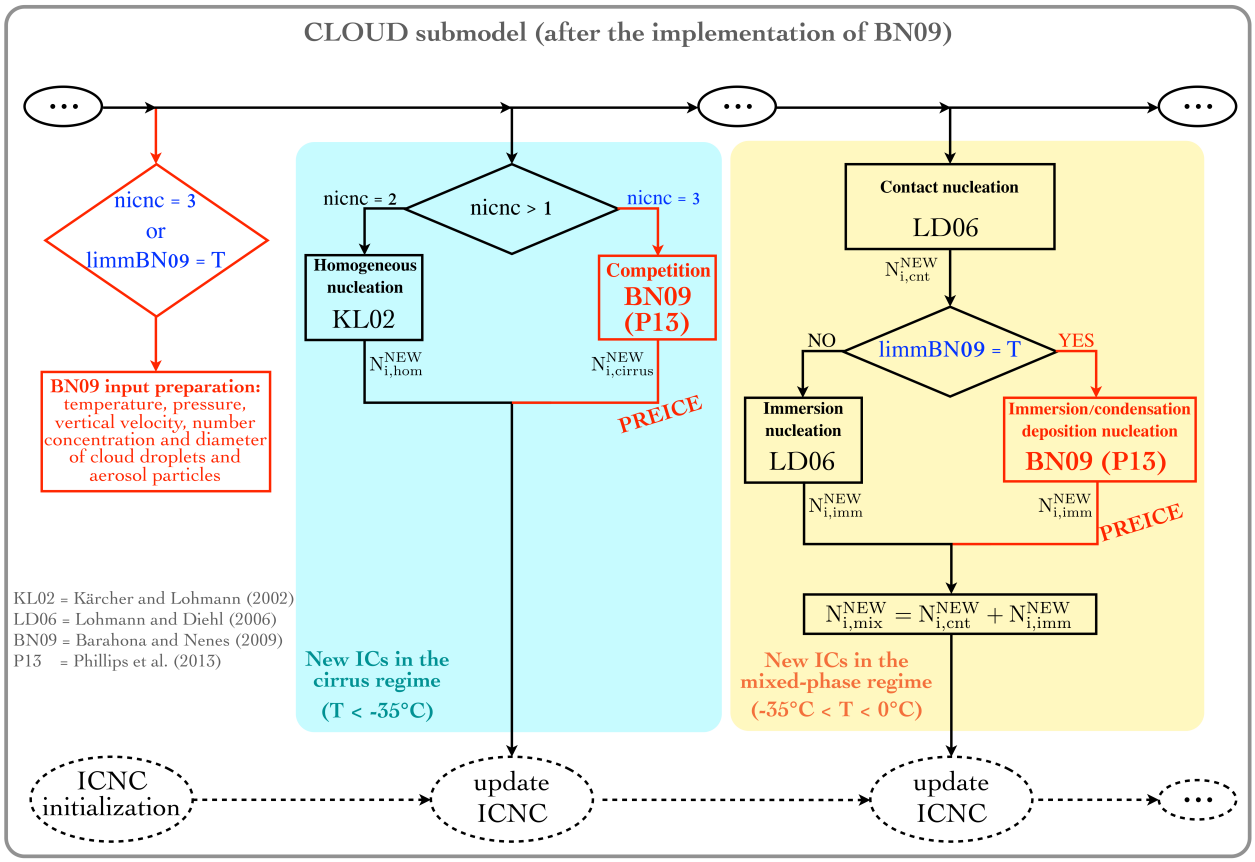

Figure 3.2: Scheme of the new ice crystal formation in the CLOUD submodel. Red parts are new (after the implementation of BN09); three dots indicate other processes coded in CLOUD.

Chapter 4

Model results and evaluation

The BN09 parameterization improves the ice nucleation representation in EMAC by taking into account processes which were previously neglected by KL02 and LD06 (i.e. competition for water vapour between homogeneous and heterogeneous nucleation, influence of polydisperse aerosols, and PREICE). This chapter analyses the model performance obtained using BN09 in different cloud regimes in comparison with the EMAC standard configuration used so far.

The numerical experiments designed for this purpose are specified in Section 4.1. Section 4.2 describes the model results, while Section 4.3 presents the evaluation of the model. The conclusions are given in Section 4.4.

4.1 Simulation setups

All the simulations have been performed at T42L31ECMWF resolution, which corresponds to a spherical truncation of T42 (i.e. quadratic Gaussian grid of approximately $2.8° \times 2.8°$, in latitude and longitude) and 31 vertical hybrid pressure levels up to 10 hPa (about 25 km), as described in Section 2.1. The simulations are 6 years long (with a model time step of 20 minutes), and the last 5 years have been used for the analysis (the first year has been considered spin-up time). Prescribed climatologies (30 years, from 1980 to 2009) of sea surface temperatures (SST) and sea-ice concentrations (SIC) from AMIP have been applied as boundary conditions (Hurrell et al., 2008). Different databases have been used for the emissions.

- Gas emissions.
  Biomass burning emissions have been taken from GFEDv3.1 (van der Werf et al., 2010), anthropogenic and aircraft emissions from CMIP5-RCP4.5 (Clarke et al., 2007), volcanic emissions from AEROCOM (Dentener et al., 2006), and natural ammonia emissions from GEIA (Bouwman et al., 1997). Also, the emissions of halocarbons (Kerkweg et al., 2008), dimethyl sulfide (Kettle et al., 1999), and methyl iodide (Bell et al., 2002) have been used. Instead, soil-biogenic NO_x and VOCs have been computed online.

- Aerosol emissions.
  Like in Pozzer et al. (2012), mineral dust has been emitted offline using monthly emis-

Simulations	Ice nucleation schemes	
	Cirrus regime	Mixed-phase regime
KL+LD (DEF)	KL02: pure homogeneous nucleation	LD06: immersion nucleation
BN+LD	BN09: competition and PREICE	
KL+BN	KL02: pure homogeneous nucleation	BN09: immersion/condensation and deposition nucleation via P13
BN+BN	BN09: competition and PREICE	

Table 4.1: Simulations analysed in this chapter. It must be remembered that contact nucleation is always computed in the mixed-phase regime via LD06.

sion files based on the AEROCOM data set. AEROCOM has been used for secondary organic aerosol and sea salt emissions as well. GFEDv3.1 and CMIP5-RCP4.5 have been employed for the emissions of black carbon and organic carbons with biomass burning and anthropogenic origins, respectively. Aerosol climatologies have been also used for heterogeneous chemistry (Aquila et al., 2011) and interactions with radiation (Tanre et al., 1984).

Radiatively active species have been nudged following the CCMI recommendations (see Subsection 2.2.2).

Cloud droplet formation has been parameterized via the UAF scheme (see Section 2.3), like in Karydis et al. (2017). Contact nucleation has been always computed according to LD06 (see Subsection 2.3.2). Among the INP parameterizations available in the BN09 code, the P13 parameterization has been selected to simulate deposition and immersion/condensation nucleation whenever BN09 is called (see Subsection 3.1.2).

In order to analyse the performance of the model using BN09 in different cloud regimes, four numerical experiments have been carried out (Table 4.1). The default simulation (KL+LD or DEF) is performed with the standard configuration of the EMAC model, i.e. using the parameterizations KL02 in the cirrus regime and LD06 for immersion nucleation in the mixed-phase regime. Other three simulations have been run in such a way that BN09 computes the new ice crystals only in the cirrus regime (BN+LD), only in the mixed-phase regime (KL+BN), and in both cloud regimes (BN+BN).

Since LD06 takes into account only dust and soot for immersion nucleation, the same aerosol components have been considered also in P13, neglecting the potential contribution of bioaerosols and organics.

4.2 Model results

4.2.1 Annual zonal means

The annual zonal means of ICNC and ice water content (IWC) are shown as functions of latitude and pressure in Figure 4.1, where the isolines at 0°C and −35°C indicate the approximate

bounds of the cirrus and mixed-phase regimes. ICNCs show similar patterns in all simulations despite their different setups, indicating the important role of atmospheric dynamics. ICNCs decrease towards lower altitudes (Figure 4.1a) because the ice nucleation rate reduces with increasing temperature. They are much higher over the mid-latitudes in the NH because of larger INP concentrations and the influence of big mountain chains, e.g. Rocky Mountains and the Himalayas, which generate strong updraughts and so high relative humidities.

The relative changes show that the ICNCs computed using BN09 in the cirrus regime are much lower (by $\sim 60\%$) than the default case in the upper troposphere and at high latitudes in the SH (Figure 4.1b). According to the absolute changes of ICNC annual zonal means computed as functions of latitude and temperature (Figure A.1 in Appendix A.2), the ICNCs in BN+KL are lower than the default case at least by 100 L^{-1} at temperatures below $-50°C$. In particular, the globally averaged absolute changes reach a minimum of about -200 L^{-1} between $-60°C$ and $-70°C$ when comparing BN+LD with KL+LD (Figure A.1, last row in Appendix A.2). It has been demonstrated that homogeneous nucleation dominates in the upper troposphere in the tropics and in the SH (Haag et al., 2003; Liu et al., 2012; Barahona et al., 2017), while heterogeneous nucleation is important in the NH (Liu et al., 2012; Kuebbeler et al., 2014; Storelvmo and Tan, 2015; Shi et al., 2015; Gasparini and Lohmann, 2016; Barahona et al., 2017) where cirrus clouds are originated by a combination of homogeneous and heterogeneous nucleation processes. As BN08 and KL02 produce similar orders of magnitude of ICNCs (Barahona and Nenes, 2008), the negative bias in Figure 4.1b is likely due to the newly-introduced PREICE (see Section 3.2). Interestingly, ICNCs at lower altitudes are also influenced by the ice nucleation parameterization used in the cirrus regime. In fact, there is an increase of ICNCs due to a faster sedimentation of the larger ice crystals produced by BN09 in cirrus clouds, especially in the NH where there are larger sources of INPs. In the mixed-phase, the changes are very small (mostly within $\pm 20\%$). Overall, the total ICNC in BN+LD globally decreases in comparison with KL+LD.

The ICNC changes obtained by comparing KL+BN with KL+LD (Figure 4.1c) are especially evident in the NH (more than 40%). As P13 produces fewer new ice crystals than LD06 (as remarked in Subsection 3.1.2), the positive biases in the mixed-phase regime are likely due to influences from the cirrus regime (e.g. ice crystal sedimentation) and convective detrainment. Overall, changing the nucleation scheme in the mixed-phase regime produces smaller deviations (mostly within $\pm 20\%$) than replacing BN09 with KL02 in the cirrus regime. Possibly, the rates of new ICs formed via heterogeneous nucleation in the mixed-phase regime are masked by other processes (e.g. sedimentation) which also influence ICNCs in this regime (this will be discussed in Chapter 7). Finally, the simulation using BN09 in both regimes combines the effects described so far (Figure 4.1d).

The ICNC seasonal zonal means for summer (June-July-August, JJA) and winter (December-January-February, DJF) have been also computed (Figure 4.2). The seasonal analysis helps us to associate the ICNCs to the corresponding cloud regimes, as the ICNC patterns better follow the isotherms.

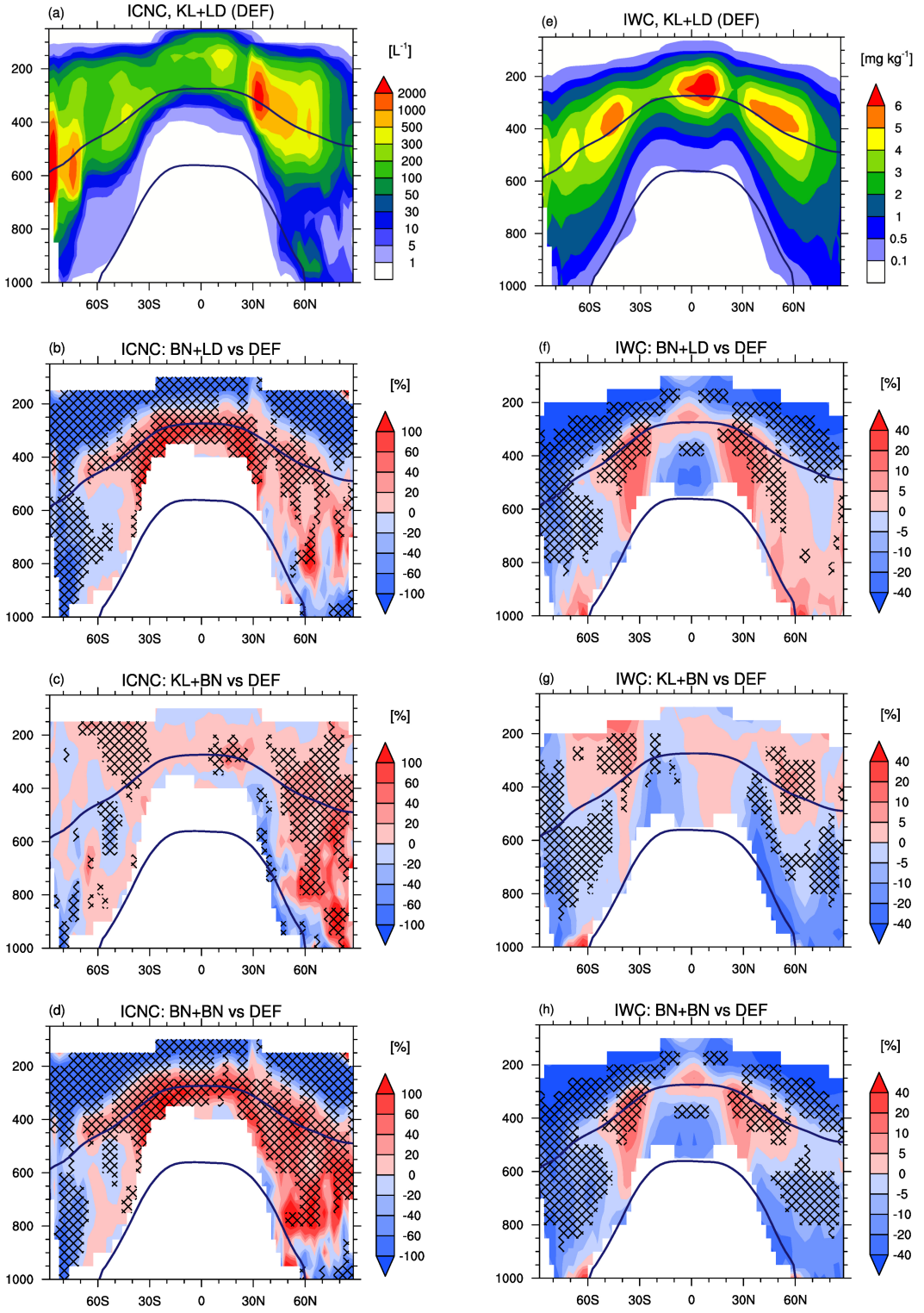

Figure 4.1: Annual zonal means of (grid-averaged) ICNCs and non-precipitable IWC for the default simulation KL+LD and the relative percentage changes of BN+LD, KL+BN, and BN+BN with respect to it (i.e. $(test - \mathrm{DEF})/\mathrm{DEF} \cdot 100$), computed where $\mathrm{ICNC}^{\mathrm{DEF}} \geq 1$ L^{-1} and $\mathrm{IWC}^{\mathrm{DEF}} \geq 0.1$ mg kg^{-1}. The isotherms at 0°C and −35°C are annual means; the crossed pattern indicates areas with a significance level of 95%.

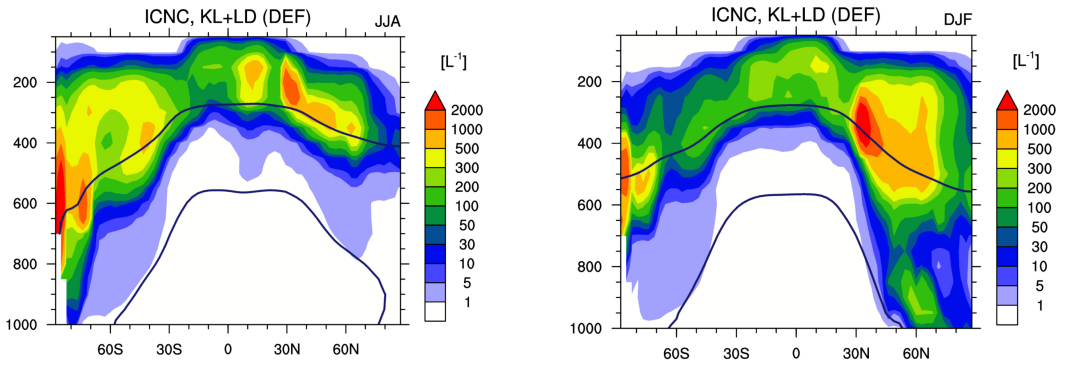

Figure 4.2: Seasonal (summer-*left* and winter-*right*) zonal means of (grid-averaged) ICNCs for the default simulation KL+LD. The isotherms at 0°C and −35°C are seasonal means.

The IWC pattern (Figure 4.1e) qualitatively follows the ICNC distribution. It is quite symmetrical between the two hemispheres except at high latitudes in the NH, where IWC is slightly higher because of the higher values of ICNC. Particularly, IWC exhibits three local maxima: two over the mid-latitudes in both hemispheres and one in the tropics, associated to storm tracks and deep convections, respectively (Li et al., 2012), in agreement with satellite observations (e.g. Waliser et al., 2009; Li et al., 2012). The IWC relative changes in Figure 4.1f show a pattern very similar to Figure 4.1b, therefore, IWC decreases where ICNC reduces (and vice versa) when BN09 is used in the cirrus regime. On the other hand, IWC in KL+BN is slightly reduced (up to 20%) in the mixed-phase regime in areas where ICNC increases, especially in the NH at high latitudes (Figure 4.1g), due to the different size of ice crystals. However, the areas with significant differences are rather small. Finally, BN+BN in Figure 4.1h simulates an overall reduction of IWC, except in the three areas with higher values of IWC described for Figure 4.1e.

4.2.2 Global distributions

Figure 4.3 shows the global distributions of ICNC annual means at two different altitudes: 200 hPa (where temperatures vary between −75°C and −55°C) to represent the cirrus regime and 600 hPa (where temperatures are approximately between −35°C and −15°C) to represent the mixed-phase regime.

ICNCs in the cirrus regime (Figure 4.3a) present high values over land in correspondence with mountainous regions, e.g. the Rocky Mountains, Andes, and Tibetan Plateau with ICNCs > 500 L^{-1}. Such a pattern is strongly related to the turbulent contribution of the vertical velocity (i.e. w_{sub}) and in agreement with Gryspeerdt et al. (2018a), who detected in these areas mostly orographic cirrus clouds. Figure 4.3a also shows higher ICNCs around the edge of the Antarctic ice sheet and over those regions which experience a strong convective activity, i.e. the Inter Tropical Convergence Zone (ITCZ) and the Tropical Warm Pool (TWP), as observed in Sourdeval et al. (2018). The annual global mean of ICNC at 200 hPa is about 200 L^{-1} ($\sim$ 390 L^{-1} over land and $\sim$ 124 L^{-1} over ocean). The fact that concentrations

are higher over continents ($\sim 48 \cdot 10^8$ m^{-2}), where vertical updrafts are stronger and aerosol concentrations more abundant, than over oceans ($\sim 11 \cdot 10^8$ m^{-2}) is also confirmed by the vertically integrated ice crystal number concentrations ($ICNC_{burden}$, Figure A.2 in Appendix A.2).

The ICNC relative changes clearly show that BN09 used in the cirrus regime (Figure 4.3b) reduces ICNC (up to 60%) worldwide with respect to the default experiment, and the ICNC annual global mean drops to 137 L^{-1} (i.e. more than 30%). Such a reduction is probably due to the PREICE and possibly to the differences between BNhom and KL02. Nevertheless, there are some positive biases along the ITCZ and over the TWP area. As the concentrations of new ice crystals produced by BN09 are not particularly remarkable in these regions (not shown), convective detrainment is likely to play a role. Indeed, there is a certain response of the convective activity to the choice of the ice nucleation scheme used in the cirrus regime. On the contrary, KL+BN is characterised by a general increase of ICNC (Figure 4.3c). However, most of the areas with strong positive changes (larger than 60%) correspond to regions characterised by low ICNC (< 30 L^{-1}), thus, the annual global mean increases just up to 218 L^{-1} (i.e. +9%).

At 600 hPa, ICNCs increase towards high latitudes, in particular over Greenland (up to 2000 L^{-1}) and Antarctica (mostly > 2000 L^{-1}) (Figure 4.3e). It must be said that, due to the very low temperatures in the latter region, even at 600 hPa the conditions are typical of the cirrus regime, and the high ICNCs can be related to the high values of both w_{sub} and S_i. Gryspeerdt et al. (2018a) found that cirrus clouds over Antarctica have primarily synoptic origin and partially orographic origin. Differently from Figure 4.3e, observations do not present such a high peak of ICNC over Antarctica (Gryspeerdt et al., 2018b; Sourdeval et al., 2018). The ICNC annual global mean is about 53 L^{-1}, which means about one quarter of the global mean computed at 200 hPa for KL+LD. Figure 4.3f confirms what already noticed in Figure 4.1b, that is the ice nucleation scheme used in the cirrus regime affects the ICNC in the mixed-phase regime, predicting higher ICNCs especially in the NH. Nevertheless, the largest differences occur in areas where ICNCs are very low, and the annual global mean actually decreases to 47 L^{-1} because of the negative contributions in the SH. Figure 4.3g also shows strong positive biases, but ICNCs do not change globally (52 L^{-1}). Thus, we can reiterate that the ICNC is more sensitive to ice nucleation scheme changes in the cirrus regime than in the mixed-phase regime.

IWC at 200 hPa and 600 hPa (Figure 4.4) present patterns qualitatively similar to the ICNCs at the corresponding pressures. Nevertheless, high IWC values (> 10 mg kg^{-1}) at 200 hPa are evident over the TWP, where ICNCs are not particularly high. This is probably caused by the larger radius of ice crystals simulated in this area. The relative changes of IWC with respect to the default simulation (Figure A.3 in Appendix A.2) approximately follow the changes obtained for ICNC, i.e. IWC reduces where ICNC decreases and vice versa.

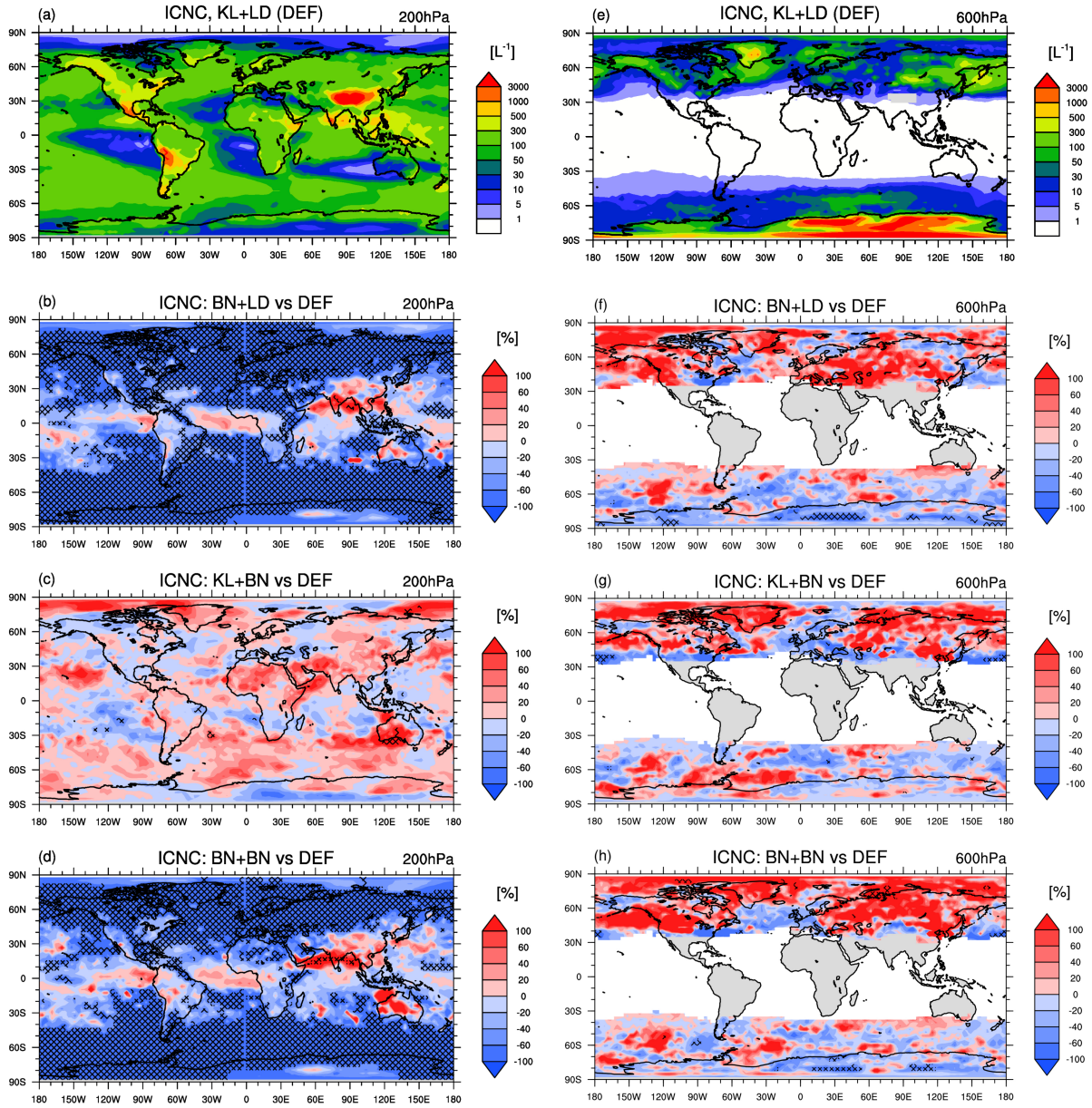

Figure 4.3: Annual means of (grid-averaged) ICNCs at 200 hPa and 600 hPa for the default simulation KL+LD and the relative percentage changes of BN+LD, KL+BN, and BN+BN with respect to it (i.e. $(test - \mathrm{DEF})/\mathrm{DEF} \cdot 100$), computed where $\mathrm{ICNC}^{\mathrm{DEF}} \geq 1\ \mathrm{L}^{-1}$. The crossed pattern indicates areas with a significance level of 95%.

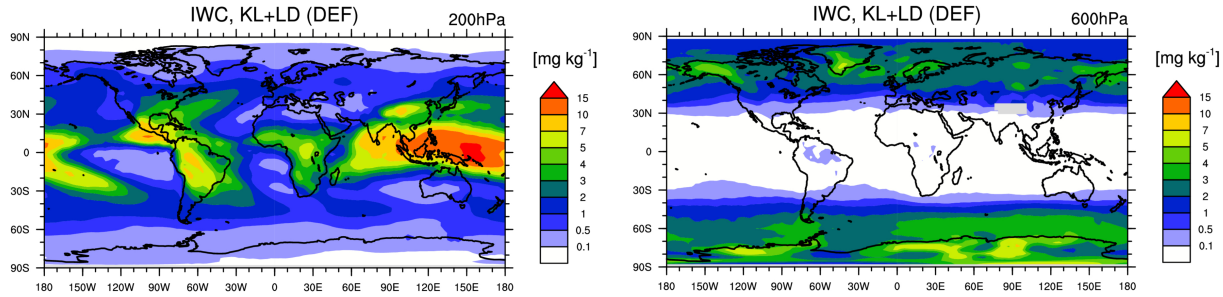

Figure 4.4: Annual means of (grid-averaged) IWC at 200 hPa and 600 hPa for the default simulation KL+LD.

4.3 Comparisons with observations

4.3.1 Annual global means

Table 4.2 shows an overview of the annual global means of cloud microphysical variables and radiative fluxes computed with the model results and satellite observations; the percentage changes with respect to the default simulation are also included.

$ICNC_{burden}$ changes considerably depending on the ice scheme used in the cirrus regime. When BN09 operates in the cirrus regime, $ICNC_{burden}$ decreases by 10% due to the competition between homogeneous and heterogeneous nucleation and the PREICE (a similar result has been found also by Liu et al., 2012, Kuebbeler et al., 2014, and Shi et al., 2015). On the other hand, $ICNC_{burden}$ increases by almost 7% when BN09 is used in the mixed-phase regime, probably because of sedimentation from cirrus clouds and convective detrainment (as remarked in Subsection 4.2.1). On a large scale, these effects offset each other in BN+BN, where the annual global mean is basically unchanged with respect to the default simulation. Overall, the $ICNC_{burden}$ values are very close to the annual global means found by Lohmann et al. (2008) and Kuebbeler et al. (2014), while they are one order of magnitude higher compared to the results of Wang and Penner (2010) and Shi et al. (2015). $ICNC_{burden,cirri}$ and $ICNC_{burden,mixed}$ are vertically integrated ICNCs in the cirrus regime and in the mixed-phase regime, respectively. It is interesting to see quantitatively the different contributions to the total $ICNC_{burden}$: ICNCs in the cirrus regime are about 6 times larger than the ICNCs in the mixed-phase regime when KL02 is used and about 5 times when BN09 is applied in the cirrus regime. In general, the variability of ICNC increases when BN09 is used. Vertically integrated cloud droplet number concentrations ($CDNC_{burden}$) are basically not influenced by the choice of the ice nucleation scheme. The values are comparable with previous modelling studies (e.g. Lohmann et al., 2007b; Hoose et al., 2008a; Salzmann et al., 2010; Wang and Penner, 2010; Kuebbeler et al., 2014; Shi et al., 2015) and observations, although satellite observations are still affected by strong uncertainties (Bennartz and Rausch, 2017).

The ice water path (IWP) decreases by almost 7% when BN09 is used in the cirrus regime, similarly to what has been found in Kuebbeler et al. (2014), who compared simulations as-

	KL+LD (DEF)		BN+LD (2)		KL+BN (3)		BN+BN (4)		Observations	2 vs DEF	3 vs DEF	4 vs DEF
$CDNC_{burden}$	4.15	(0.04)	4.21	(0.05)	4.12	(0.03)	4.18	(0.06)	$4.01^{(A)}$	1.32	-0.72	0.72
$ICNC_{burden}$	21.86	(0.27)	19.61	(0.32)	23.33	(0.24)	21.75	(0.50)		-10.29	6.72	-0.50
$ICNC_{burden,cirri}$	18.95	(0.24)	16.47	(0.31)	20.26	(0.18)	18.40	(0.41)		-13.09	6.91	-2.90
$ICNC_{burden,mixed}$	3.06	(0.10)	3.29	(0.13)	3.23	(0.12)	3.52	(0.16)		7.44	5.52	14.82
LWP	75.38	(0.20)	72.73	(0.24)	76.59	(0.36)	74.62	(0.63)	$87.1^{(B)}$, $23.0^{(C)}$	-3.52	1.61	-1.01
IWP	12.79	(0.04)	11.95	(0.06)	12.70	(0.02)	11.85	(0.03)	$25.8^{(C)}$, $29.0^{(D)}$	-6.57	-0.70	-7.35
$SW_{NET,TOA}$	229.30	(0.11)	232.20	(0.06)	229.10	(0.06)	231.70	(0.26)	$241.70^{(1)}$, $240.50^{(3)}$	1.26	-0.09	1.05
LW_{TOA}	-224.80	(0.20)	-230.70	(0.16)	-224.40	(0.10)	-230.10	(0.12)	$-235.40^{(1)}$, $-239.80^{(3)}$	-2.62	0.18	-2.36
$Imbalance_{TOA}$	4.52	(0.22)	1.53	(0.14)	4.65	(0.14)	1.58	(0.26)	$5.87^{(1)}$, $0.71^{(3)}$	-66.15	2.88	-65.07
SCRE	-57.82	(0.12)	-54.83	(0.08)	-58.07	(0.09)	-55.38	(0.25)	$-48.50^{(1)}$, $-47.14^{(2)}$, $-47.04^{(3)}$	5.17	-0.43	4.22
LCRE	33.95	(0.11)	28.90	(0.10)	34.40	(0.06)	29.53	(0.09)	$29.42^{(1)}$, $26.87^{(2)}$, $26.00^{(3)}$	-14.87	1.33	-13.02
NCRE	-23.87	(0.18)	-25.93	(0.10)	-23.68	(0.14)	-25.86	(0.27)	$-19.07^{(1)}$, $-19.70^{(2)}$, $-21.04^{(3)}$	-8.63	0.80	-8.34
TCC	70.01	(0.13)	69.04	(0.11)	70.04	(0.14)	69.23	(0.16)	$66.83^{(4)}$, $66.70^{(5)}$	-1.39	0.04	-1.11
P_{tot}	2.902	(1.9E-05)	3.032	(1.4E-05)	2.892	(2.6E-05)	3.024	(3.1E-05)	$2.624^{(6)}$, $2.669^{(7)}$	4.48	-0.34	4.20

Table 4.2: Global annual means for model results and observations. Shown are grid-averaged vertically integrated cloud droplet number concentration ($CDNC_{burden}$, $[\ 10^{10}\ m^{-2}\ ]$), vertically integrated ice crystal number concentration ($ICNC_{burden}$, $[\ 10^{8}\ m^{-2}\ ]$), vertically integrated ice crystal number concentration in the cirrus regime ($ICNC_{burden,cirri}$, $[\ 10^{8}\ m^{-2}\ ]$), vertically integrated ice crystal number concentration in the mixed-phase regime ($ICNC_{burden,mixed}$, $[\ 10^{8}\ m^{-2}\ ]$), grid-averaged liquid water path (LWP, $[\ g\ m^{-2}\ ]$) and ice water path (IWP, $[\ g\ m^{-2}\ ]$), net shortwave radiative flux ($SW_{NET,TOA}$, $[\ W\ m^{-2}\ ]$), longwave radiative flux (LW_{TOA}, $[\ W\ m^{-2}\ ]$), and radiative imbalance ($Imbalance_{TOA}$, $[\ W\ m^{-2}\ ]$) at TOA, shortwave cloud radiative effect (SCRE, $[\ W\ m^{-2}\ ]$), longwave cloud radiative effect (LCRE, $[\ W\ m^{-2}\ ]$), net cloud radiative effect (NCRE, $[\ W\ m^{-2}\ ]$), total cloud cover (TCC, $[\ \%\ ]$), total precipitation (P_{tot}, $[\ mm\ day^{-1}\ ]$). The values in brackets are (temporal) standard deviations. The sixth column contains the annual global means computed using the satellite data from ERBE 1985-1990$^{(1)}$ and 2000-2006$^{(4)}$, CERES-SYN1deg 2004-2010$^{(2)}$, CERES-EBAF 2000-2016$^{(3)}$, MODIS-TERRA 2004-2008$^{(5)}$, CMAP 1970-2016$^{(6)}$, GPCP 19790-2009$^{(7)}$, and global means taken from the literature: $^{(A)}$ and $^{(B)}$ are derived from AVHRR data (Gettelman et al., 2010; Han et al., 1994), $^{(C)}$ is derived from CloudSat data (Li et al., 2012) and $^{(D)}$ from ISCCP data (Storelvmo et al., 2008). The last three columns show the percentage changes $[\ \%\ ]$ of the experiments 2, 3, 4 with respect to the default simulation, i.e. $(test - \mathrm{DEF})/\,|\mathrm{DEF}|\ \cdot 100$.

suming pure homogeneous nucleation against simulations including water vapour competition. Overall, the EMAC underestimates the IWP, also found in other studies that applied the same GCM (e.g. Lohmann et al., 2008; Lohmann and Hoose, 2009; Kuebbeler et al., 2014; Gasparini et al., 2018). However, there are still large discrepancies among observational data sets which make problematic the validation of the models (Duncan and Eriksson, 2018). The liquid water path (LWP) estimates derived from satellite observations vary substantially, between 23 g m^{-2} and 87 g m^{-2} (Liu et al., 2012; Han et al., 1994), and the model results lie within this range. The LWP variations among the experiments are much smaller than the IWP variations.

The absolute values of the shortwave cloud radiative effect (SCRE) and longwave cloud radiative effect (LCRE) are higher than those derived from satellite data, especially when KL02 is employed in the cirrus regime. However, when the net cloud radiative effect (NCRE) is computed, the simulations using KL02 in the cirrus regime are closer to the observations. It is evident that the cloud radiative effects are sensitive to the ice nucleation scheme used for cirrus clouds. Indeed, SCRE with in BN+LD becomes weaker (more than 5%) because of the less efficient scattering of shortwave radiation by fewer and larger crystals. More importantly, LCRE decreases up to 15% because cirrus clouds, at the same, can trap less longwave radiation in the Earth-atmosphere system. As a result, NCRE becomes more negative using BN09 in the cirrus regime, with statistically significance over some areas in the tropics and high latitudes (Figure A.4 in Appendix A.2), so the cooling effect is enhanced.

The total cloud cover (TCC) is slightly overestimated by the model (likely explaining why the cloud radiative forcing is high despite IWP being half of the observed values). The changes with respect to the default simulation are very low (below 2%). The largest one is in BN+LD, where TCC reduces by 1.39% since the larger IC radii produced by BN09 in comparison with KL02 lead to higher sedimentation rates.

Finally, the model tends to overestimate the total precipitation (P_{tot}), i.e. the sum of large scale and convective precipitations, but this has also been found with other global models (e.g. Barahona et al. (2014) with GEOS-5, Shi et al. (2015) with CAM5, and Lohmann et al. (2008) and Kuebbeler et al. (2014) with ECHAM-HAM as well). When BN09 is used in the cirrus regime, P_{tot} grows by 4% especially because of the increase of the convective precipitation, due to some feedback mechanisms on the convective activity generated by the different ice nucleation schemes used, as mentioned in Subsection 4.2.2.

Overall, the model performs well with respect to the observations and literature. Mostly, the experiments do not yield evident differences among each other at the global scale, as regional variations may cancel out. In particular, the simulations using the same ice nucleation scheme in the cirrus regime are very close to each other, i.e. KL+LD and KL+BN, and BN+LD and BN+BN (Figure A.5 in Appendix A.2). However, there are clear effects on SCRE and LCRE from changing the ice nucleation scheme for cirrus clouds. As there is not a clear indication which simulation performs better, a statistical comparison with aircraft measurements has been performed in the next subsection.

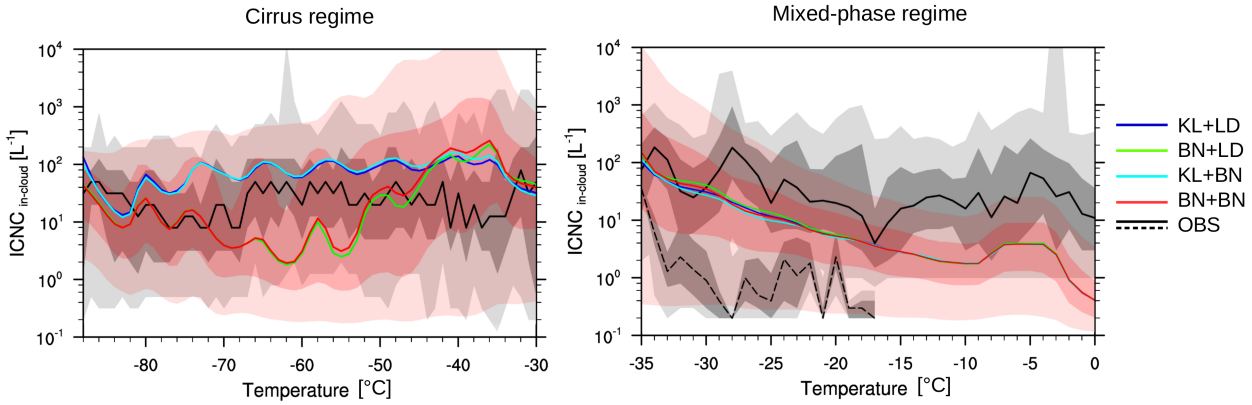

Figure 4.5: In-cloud ice crystal number concentrations versus temperature. Medians are computed for model results (using daily means between 25°S and 75°N, masking $\mathrm{ICNC}_{\mathrm{in-cloud}} < 0.1\ \mathrm{L}^{-1}$, i.e. the minimum observed value) and observations, for each temperature bin of 1°C. Darker gray/red colours indicate the observations/BN+BN between the 25th and 75th percentiles, while lighter gray/red colours indicate the observations/BN+BN between the 5th and 95th. (*Left*) Cirrus regime: the modelled medians are computed approximately in the range of $4 - 20$ km height; the observations come from the JULIA database by Krämer (personal communication). (*Right*) Mixed-phase regime: the modelled medians are computed approximately in the range of $0 - 20$ km height; the observations belong to the projects WISP-94 (solid line) and ICE-L (dashed line) and concern INP concentrations.

4.3.2 Comparison with aircraft measurements

The validation of climate models with in-situ measurements is always limited by the fact that observations are restricted in time and in space and the models have difficulties to capture individual meteorological events. Nevertheless, a large collection of aircraft measurements has been used here for the comparison with modelled in-cloud ICNC ($\mathrm{ICNC}_{\mathrm{in-cloud}}$) in the cirrus regime. The measurements belong to the JULIA database by Krämer (personal communication) and were collected in 15 years, between 1999 and 2014. 18 field campaigns (in total, 113 flights with about 127 hours in cirrus clouds) covered Europe, Australia, Africa, Seychelles, Brazil, USA, Costa Rica, and tropical Pacific between 25°S and 75°N in the temperature range of $-88°\mathrm{C} \div -30°\mathrm{C}$. Instead, only two data sets of flight measurements over North America have been used in the mixed-phase regime. The data sets come from the projects Winter Icing Storms Project (WISP-94, 2011) and Ice in Clouds Experiment-Layer Clouds (ICE-L, 2011), which consider about 99 and 46 flight hours, respectively.

Figure 4.5 (left) highlights, once again, the similarities between the simulations using the same ice nucleation scheme in the cirrus regime. For most of the temperature range, the simulations which use KL02 in the cirrus regime overestimate the observed ICNCs (although they mostly remain below the 75th percentile). The overestimation of ICNCs is common to other modelling studies (e.g. Wang and Penner, 2010; Liu et al., 2012; Shi et al., 2015) and especially in cold cirrus clouds (at $T < -68°\mathrm{C}$).

On the other hand, the simulations which use BN09 in the cirrus regime are very close to the observations at temperatures below −73°C and between −53°C and −43°C, while they underestimate ICNCs between −73°C and −53°C. In this temperature range the simulations can exceed the observed 25th percentile (although remaining within the 5th percentile), likely because of an overestimation of the water vapour competition effect and the PREICE. Barahona et al. (2010) showed that the competition between the ice nucleation mechanisms is small using P13. Also, Liu et al. (2012) found that BN09 (using PDA08 for heterogeneous nucleation) and BNhom produced very similar results in the cirrus regime, suggesting that the water vapour competition was small because of the few ice crystals formed heterogeneously. Thus, the PREICE is the process which is likely overestimated in BN+LD and BN+BN.

Overall, BN+LD and BN+BN always predict lower ICNCs at temperatures below −43°C in comparison with the other two simulations, as expected because of the water vapour competition and the PREICE. All four simulations overestimate the ICNC by one order of magnitude in the temperature range $-43°C \div -33°C$.

Interestingly, the modelled ICNCs in Figure 4.5 (left) do not show any particular trend with respect to temperature, like Kuebbeler et al. (2014) who also used ECHAM5 for the atmospheric dynamics. Disagreeing, other studies found that ICNCs are inversely proportional with temperature, e.g. Liu et al. (2012) and Shi et al. (2015) with CAM5 (using both the ice nucleation scheme of Liu and Penner (2005) and BN09) and Barahona et al. (2010) with GEOS-5 and BN09. Such distinct behaviours are likely derived from the wide model variabilities in reproducing subgrid-scale processes, like vertical velocity, which play a role in ice nucleation.

Figure 4.5 (right) shows the modelled $ICNC_{in-cloud}$ in the mixed-phase regime, considering the same latitudes as the case before (i.e. 25°S – 75°N). The simulations do not show significant differences among each other. The distinctive features are the ICNC decrease with increasing temperatures and a positive "bulge" between −8°C and −3°C caused by the secondary ice production (i.e. rime splintering). The modelled ICNCs are in quite good agreement with the two data sets of flight measurements. It is important to stress that this comparison is less accurate than the previous one because the observations here are much more limited both in time and in space than the extensive observational database used for the cirrus regime. It should be also noted that the measurements actually concern INPs. When the INP number is not high enough to deplete the ambient supersaturation, INP concentrations and ICNCs can correspond, however, it is well known that the two concentrations show discrepancies with increasing temperature because of the secondary ice formation (see Subsection 1.1.1). Furthermore, ICNCs in Figure 4.5 (right) are in good agreement with the results of Heymsfield et al. (2013), also based on flight campaigns. They found that ICNCs decrease as temperature increases and are within the range $5 - 50\ L^{-1}$ in the mixed-phase regime.

Besides the flight measurements, the recent ICNC retrievals from lidar-radar satellite measurements (e.g. Sourdeval et al., 2018; Gryspeerdt et al., 2018b) must be considered. In par-

ticular, Gryspeerdt et al. (2018b) analysed the behaviour of ICNCs within clouds as a function of temperature. Differently from Figure 4.5 (left), they showed that there is a weak temperature dependence of ICNC, which increases with decreasing temperature. On the other hand, similarly to Figure 4.5, they found a small increase of ICNC around −5°C and, interestingly, a small peak at about −40°C due to orographic and frontal regimes, which could explain the higher modelled ICNCs obtained between −45°C and −35°C.

4.4 Summary and discussion

In this chapter, three simulations have been run using the newly-implemented BN09 parameterization in the cirrus and/or in the mixed-phase regimes and have been compared with the default simulation obtained with the standard configuration of EMAC. Additionally, the model results have been compared with observations.

The main effect resulted from the application of BN09 is a strong reduction of the ICNCs in the upper troposphere (at temperatures below −50°C) when BN09 operates in the cirrus regime. ICNCs reduce by up to 300 L^{-1} (i.e. more than 60%) with respect to the default case. Such reduction is ascribed to the water vapour competition between homogeneous and heterogeneous nucleation and, more likely, to the PREICE (this will be proved in the next chapter). By contrast, when BN09 operates in the mixed-phase regime, ICNCs slightly increase, especially in the NH. Nevertheless, the increment is mostly limited to 10 L^{-1} (i.e. 20%) and is probably due to influences from cirrus clouds (e.g. ice crystal sedimentation) and convective detrainment, as P13 actually produces fewer new ice crystals than LD06 (as remarked in Subsection 3.1.2).

In general, we found that changing the ice nucleation scheme in the cirrus regime generates larger differences of ICNC and IWC than changing the parameterization in the mixed-phase regime. Interestingly, it has been observed a certain dependence of ICNC and IWC in the mixed-phase regime on the parameterization used in the cirrus regime, likely due to a faster sedimentation of the larger ice crystals produced by BN09 in cirrus clouds at higher altitudes.

Overall, the model results agree well with global observations and the literature data. The comparison made with a large collection of flight measurements in the cirrus regime (i.e. the JULIA database) has pointed out that ICNCs are overestimated when KL02 is applied. The simulations using BN09 in the cirrus regime well agree with the observations in cold cirrus clouds, however, the PREICE is overestimated causing an underestimation of ICNCs between −73°C and −53°C. In the mixed-phase regime, the simulations are between the observations taken from two airfcraft campaigns (from the projects WISP-94 and ICE-L) and are comparable with other databases in the literature (e.g. Heymsfield et al., 2013). Additionally, the ICNC seasonal zonal means (Figure 4.2) and the ICNC profiles against temperature (Figure 4.5) are qualitatively in agreement with the ICNCs recently retrieved from the DARDAR data set by Sourdeval et al. (2018) and Gryspeerdt et al. (2018b).

As BN09 takes into account processes which were previously neglected by the standard version of the model (i.e. competition for water vapour between the ice nucleation mechanisms, influence of polydisperse aerosols, and PREICE), without additional computational resources, its application is recommended for EMAC simulations. Among the INP parameterizations available in BN09, the selection of P13 is preferred since it simulates both deposition and immersion/condensation nucleation modes and incorporates the ice-nucleating ability of different aerosol types, i.e. dust, soot, bioaerosols, and glassy organics (their influence on heterogeneous nucleation will be discussed in Chapter 6). Therefore, the new configuration BN+BN makes the EMAC model one of the few GCMs which take into account the complexity of ice nucleation in a detailed manner.

Chapter 5

Competition for water vapour in cold clouds

This chapter analyses the competition for water vapour between homogeneous and heterogeneous nucleation and the effect of pre-existing ice crystals. These processes have been already studied by means of different GCMs, for instance, Kuebbeler et al. (2014) used ECHAM5-HAM with the parameterization of Kärcher et al. (2006), Barahona et al. (2014) used GEOS-5 and BN09 (with the CNT), and Shi et al. (2015) used CAM5 and BN09 (with the CNT) or the ice nucleation schemes of Kärcher et al. (2006) and Liu and Penner (2005). Now, thanks to the new configuration BN+BN, the competition for water vapour between the ice nucleation mechanisms and the water vapour depletion by pre-existing ice crystals can be investigated also by means of the EMAC model.

The simulations used in this chapter are described in Section 5.1, their analysis is presented in Section 5.2, while Section 5.3 contains the final discussion of the results.

5.1 Simulation setups

The simulations designed for the analysis of the water vapour competition between the ice nucleation mechanisms and the PREICE apply the new configuration BN+BN, as recommended in Section 4.4. Four numerical experiments have been performed (Table 5.1). The simulation which includes homogeneous nucleation, heterogeneous nucleation, their competition for water vapour, and the PREICE is named PRECOM and represents the state-of-the-art case. The simulation neglecting the PREICE is named COMP, the HOM simulation assumes pure homogeneous nucleation in the cirrus regime, while HET assumes pure heterogeneous nucleation in the cirrus regime. The simulations have been run for 6 years, and the last 5 years have been used for the analysis (the first year has been considered spin-up time).

Differently from the simulations of Chapter 4, the simulations of Table 5.1 consider all the aerosol groups of P13 (i.e. DU, BC, OC, and BIO) for immersion/condensation and deposition nucleation. As this chapter considers only the total ICs produced via heterogeneous nucleation,

Simulations	Ice nucleation schemes	
	Cirrus regime	Mixed-phase regime
HET	P13 (i.e. pure heterogeneous nucleation)	P13
HOM	BN08 (i.e. pure homogeneous nucleation)	P13
COMP	BN09 (i.e. water vapour competition)	P13
PRECOM	BN09 with the PREICE	P13

Table 5.1: Simulations analysed in this chapter. It must be remembered that contact nucleation is always computed in the mixed-phase regime via LD06.

the description of the bioaerosol emissions is included in the next chapter, which instead focuses on the individual contributions of aerosol components to heterogeneous nucleation. Moreover, it must be mentioned that the mean of the Gaussian probability density function of updraught velocities in equation 3.2 has been changed in the BN09 algorithm used for the simulations of Table 5.1. While the mean was previously assumed constant, fixed at 0.1 cm s^{-1} (see Subsection 3.1.1), it is now equal to the grid-mean vertical velocity resolved by the model (i.e. $\overline{w}$).

5.2 Model results

5.2.1 In-cloud ICNCs

The annual zonal means of in-cloud ICNCs computed for the COMP simulation and the absolute changes with respect to the other three simulations are presented in Figure 5.1. The annual zonal means (Figure 5.1a) show a pattern similar to the one already observed in Figure 4.1a. By comparing the simulations PRECOM and COMP (Figure 5.1b), it is evident that the PREICE has a significant impact in the cirrus regime, as found in Barahona et al. (2014), Kuebbeler et al. (2014), Shi et al. (2015), and Zhou et al. (2016). In fact, ICNCs are reduced by more than 100 L^{-1} (i.e. $> 60\%$) in the upper troposphere and at high latitudes, confirming what found in Section 4.2. Differently, the PREICE has a minor effect on ICNCs in the mixed-phase regime, mostly varying within ± 10 L^{-1} (Figure 5.1b). Indeed, the PREICE significantly reduces the formation of new ICs from homogeneous nucleation but decreases only slightly the production of new ICs from heterogeneous nucleation (Shi et al., 2015). The ICNC increment in the NH is likely due to different feedback mechanisms generated in the two simulations, PRECOM and COMP, rather than being a direct influence of the PREICE.

There are no evident changes between HOM and COMP (Figure 5.1c), meaning that heterogeneous nucleation in COMP rarely inhibits homogeneous nucleation, like observed by Liu et al. (2012), Kuebbeler et al. (2014) and Zhou et al. (2016). By contrast, the comparison between HET and COMP (Figure 5.1d) shows wide and significant negative biases in the upper troposphere and at high latitudes. The strong ICNC reduction proves the important role of homogeneous nucleation in producing new ICs in COMP. Thus, it can be inferred that

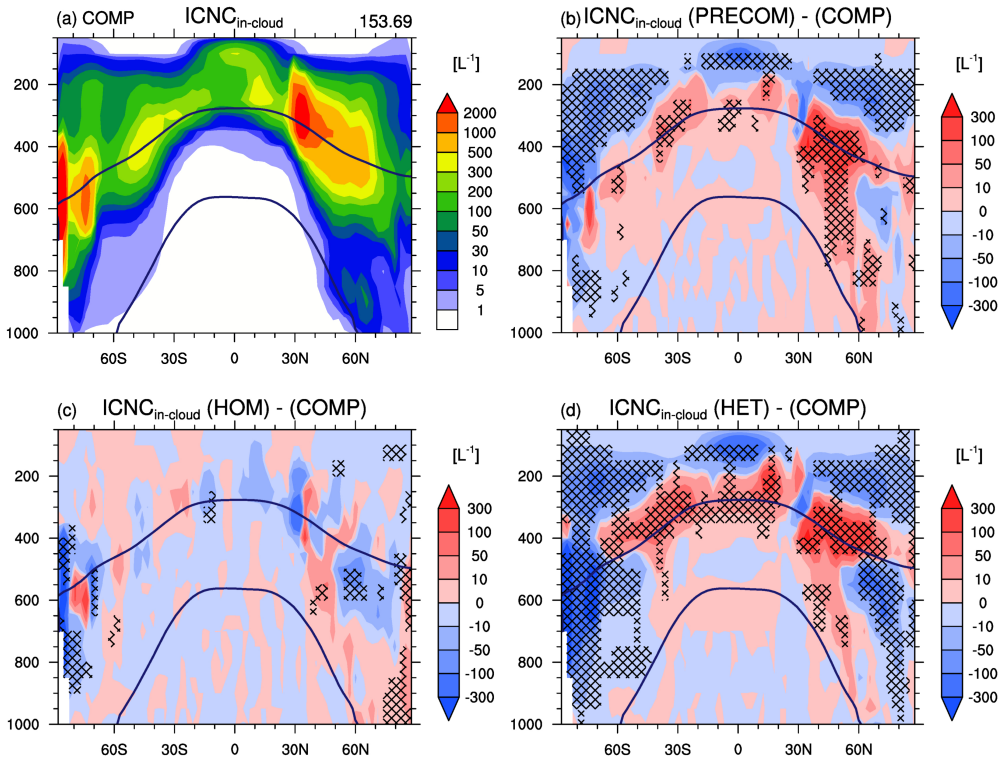

Figure 5.1: Annual zonal means of $\mathrm{ICNC}_{\mathrm{in-cloud}}$ for the simulation COMP and the absolute changes of PRECOM, HOM, and HET with respect to it. The number on the top right of the plot is the global mean (in L^{-1}); the isotherms at 0°C and −35°C are annual means; the crossed pattern indicates areas with a significance level of 95%.

homogeneous nucleation is the dominant ice nucleation mechanism in simulations applying the BN+BN configuration, in line with Haag et al. (2003), Heymsfield et al. (2013), Spichtinger and Krämer (2013), Gettelman et al. (2012), and Barahona et al. (2014).

In-cloud ICNCs have been also presented as functions of temperature in Figure 5.2. These results are not directly comparable with the ones in Figure 4.5 because the former are medians computed with 5-hour means (and not with daily means which can smooth the profiles) and include the latitudes from 90°S to 90°N (and not only the interval 25°S–75°N). Furthermore, the simulations in Figure 5.2 include the effects due to the change of the mean value considered for the Gaussian distribution of updraught velocities from 0.1 cm s^{-1} to $\overline{w}$, as described in Section 5.1.

The profiles in the cirrus regime (Figure 5.2, left) corroborate the previous observations. The PREICE causes a continuous reduction of ICNC, so that the concentrations in PRECOM are constantly lower than in COMP, like in Barahona et al. (2014). This is also in line with the studies of Shi et al. (2015) and Zhou et al. (2016), although their simulations excluding the PREICE gave much higher ICNCs (close to 10^3 L^{-1}) than COMP, and the difference with the simulations including the PREICE was more pronounced (up to a factor of 10).

The weak role of the water vapour competition between homogeneous and heterogeneous

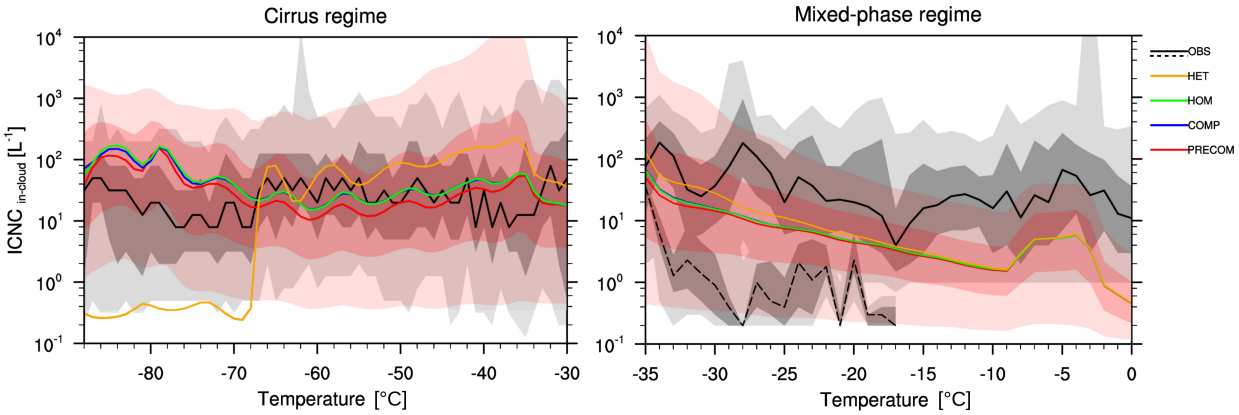

Figure 5.2: In-cloud ice crystal number concentrations versus temperature. Medians for model results are computed using 5-hour means between 90°S and 90°N, masking $\mathrm{ICNC}_{\mathrm{in-cloud}} < 0.1\ \mathrm{L}^{-1}$, for each temperature bin of 1°C. Darker gray/red colours indicate the observations/PRECOM between the 25th and 75th percentiles, while lighter gray/red colours indicate the observations/PRECOM between the 5th and 95th. (*Left*) Cirrus regime: the modelled medians are computed approximately in the range of $4 - 20$ km height; the observations come from the JULIA database by Krämer (personal communication). (*Right*) Mixed-phase regime: the modelled medians are computed approximately in the range of $0 - 20$ km height; the observations belong to the projects WISP-94 (solid line) and ICE-L (dashed line) and concern INP concentrations.

nucleation is confirmed by the fact that the profiles associated to COMP and HOM overlap along the all temperature interval (like in Zhou et al., 2016).

The in-cloud ICNC profile predicted by HET is the one which detaches the most from the other profiles. The concentrations are very low in cold cirrus clouds (at $T < -68$°C), between 0.2 and 0.4 L^{-1}, i.e. about two orders of magnitude lower than the ICNCs resulting from the other simulations. Then, the concentrations undergo a big increase up to values even higher than the ones predicted by the other simulations. The difference between HET and COMP at low temperatures definitely highlights the predominance of homogeneous nucleation over heterogeneous nucleation, associated to very high altitudes (below 350 hPa, see Figure A.6 in Appendix A.3) or polar latitudes (see Figure 5.1d). It has to be noted the unexpected high concentrations at $T > -68$°C, despite the lower formation of new ICs in HET (see Figure 5.3, last row). Therefore, other sources of ICs are responsible for the high ICNCs. The analysis of the tendencies of the physical processes in COMP and HET (not shown) points out that the instantaneous freezing and convective detrainment, two important sources of ICs (as explained in Chapter 7), are more important in HET than in COMP at pressures higher than 350 hPa.

In the mixed-phase regime (Figure 5.2, right), the simulations HOM, COMP, and PRECOM generate similar ICNCs, although it can be inferred a weak influence of the PREICE in the ICNCs predicted by PRECOM. Also in this regime, the ICNCs of HET are the highest (at least until $T < -10$°C).

5.2.2 Newly-formed ice crystals

In order to focus on the concentrations of the new ICs produced via the ice nucleation mechanisms, the next analysis concerns only the products of the BN09 parameterization rather than the ICNCs, which are the result of various processes (e.g. entrainment, sedimentation, aggregation, etc.) besides ice nucleation. As defined in Chapter 3, $N_{i,hom}$ is the result of BNhom in the cirrus regime, while $N_{i,het}$ (or $N_{i,imm}^{NEW}$) is the product of P13 in both cloud regimes.

We emphasise the fact that contact nucleation is not investigated in this thesis. This nucleation mode is computed via LD06 in all simulations and does not show differences in the production of new ICs (i.e. $N_{i,cnt}^{NEW}$, see Figure A.7 in Appendix A.3). Nevertheless, it can be mentioned that the concentrations $N_{i,cnt}^{NEW}$ are larger than $N_{i,imm}^{NEW}$ by one order of magnitude (see $N_{i,het}$ in Figure 5.3). The results in the literature concerning the contributions of different heterogeneous nucleation modes are still controversial. For instance, Yun and Penner (2012) showed that immersion/condensation/deposition nucleation was the dominant process in comparison with contact nucleation, using PDA08 to simulate both mechanisms. However, by using the parameterization of Young (1974) for contact nucleation within the same GCM (CAM3-IMPACT), contact nucleation was the dominant mode.

The concentrations per integration time of the newly-produced ICs via homogeneous and heterogeneous nucleation are shown in Figure 5.3. $N_{i,hom}^{*}$ (where the superscript * indicates the ratio over the integration time) shows two relative maxima between 30°and 40° in both hemispheres, around 800 hPa. These maxima are probably due to the higher values of w_{sub} in these locations (Figure A.8 in Appendix A.3) and were already observed by Liu et al. (2012). $N_{i,het}^{*}$ is characterised by concentrations higher in the NH than in SH, as expected because of higher INP emissions (as in Hoose et al., 2010b; Yun and Penner, 2012; Liu et al., 2012), and in the upper troposphere (as in Barahona et al., 2010). In all simulations, $N_{i,hom}^{*}$ is higher than $N_{i,het}^{*}$ by several order of magnitudes (like in Hendricks et al., 2011; Barahona et al., 2010), up to 10^2 in the tropics at high altitudes and up to 10^4 in the SH at high latitudes. Nevertheless, it must be stressed that $N_{i,het}^{*}$ is highly variable according to the INP parameterization used (Barahona et al., 2010; Sullivan et al., 2016).

As already noted, the PREICE strongly limits the formation of new ICs via homogeneous nucleation in the entire cirrus regime (Figures 5.3a vs. 5.3c), up to one order of magnitude in some areas. On the other hand, the production of new ICs via heterogeneous nucleation is weakly influenced by the PREICE (Figures 5.3b vs. 5.3d). Nevertheless, the PREICE seems to have some effects on $N_{i,het}^{*}$ in the cirrus regime (see the relative changes in Figure A.9, in Appendix A.3). It determines a small reduction of $N_{i,het}^{*}$ at high latitudes in the NH, where ICs mostly derive from dust and black carbon (as it will be shown in Chapter 6), and a small increment near the tropopause, where ICs have organic origin (see Chapter 6).

The concentrations $N_{i,hom}^{*}$ in COMP (Figure 5.3c) and HOM (Figure 5.3e) are very similar, confirming the fact that the competition between the ice nucleation mechanisms does not have significant effects. By contrast, the concentrations $N_{i,het}^{*}$ in HET (Figure 5.3h) are

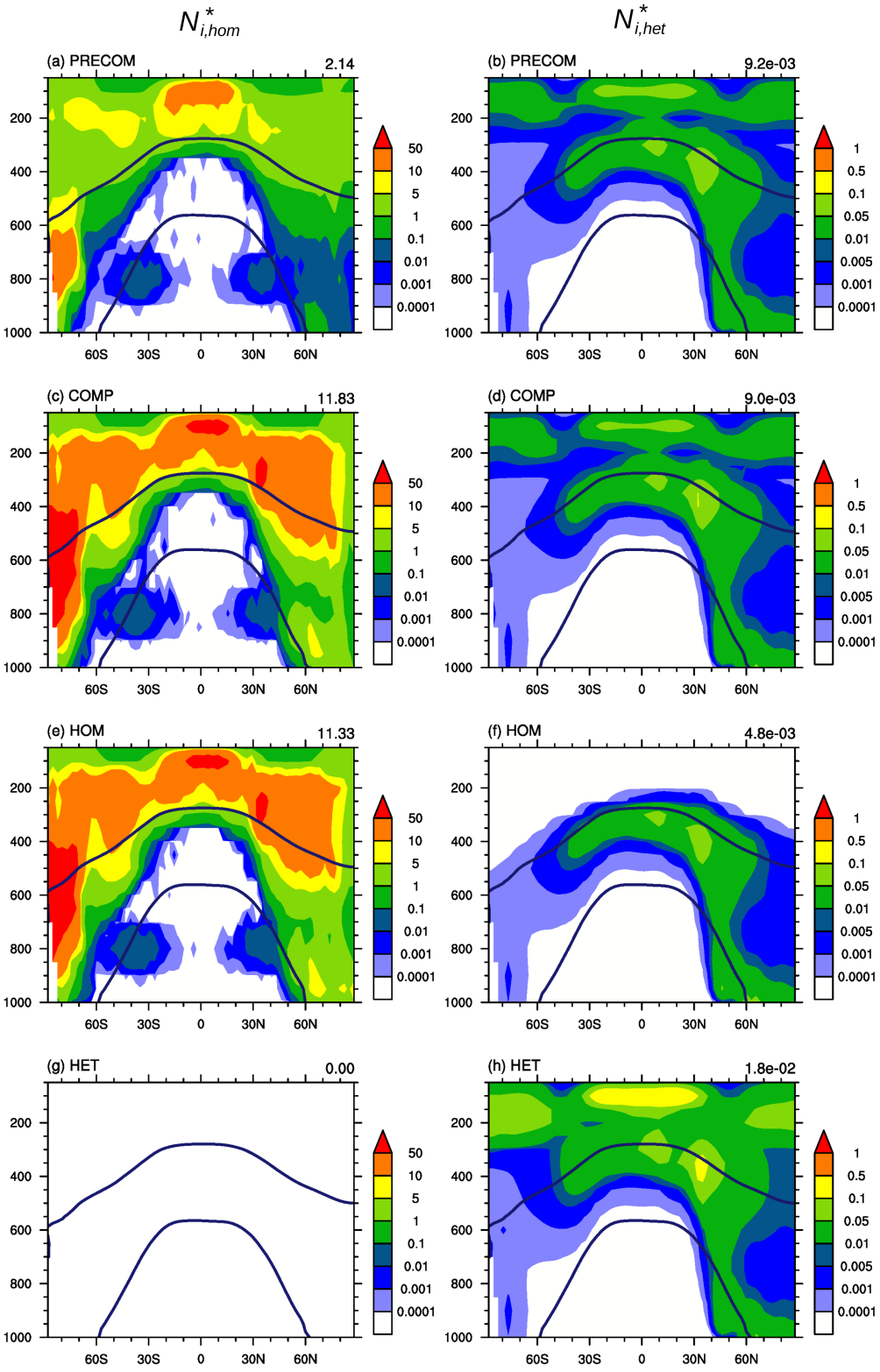

Figure 5.3: Annual zonal means of the new ICs (in L^{-1} per integration time) produced via homogeneous nucleation (*left*) and heterogeneous nucleation (*right*), for the simulations PRECOM, COMP, HOM, and HET. The numbers on the top right of the plots are global means (in L^{-1} per integration time); the isotherms at 0°C and −35°C are annual means.

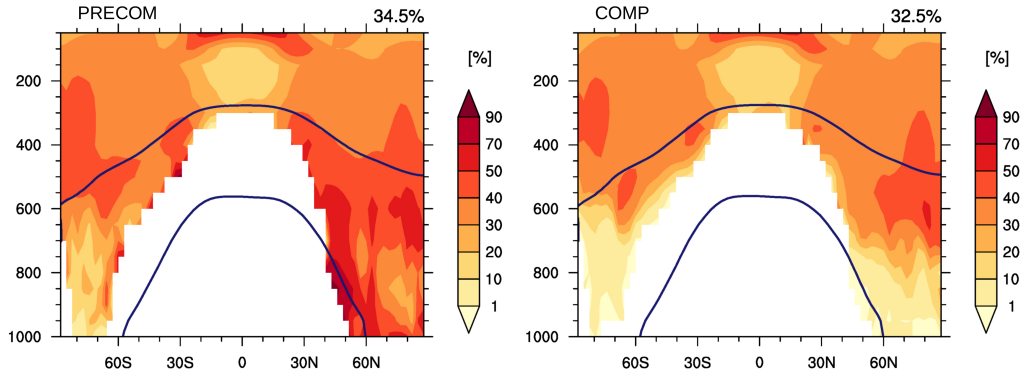

Figure 5.4: Percentage contributions of the new ICs formed heterogeneously to the total new ICs in the cirrus regime, for the simulations PRECOM (*left*) and COMP (*right*). $N^*_{i,het}$ and $N^*_{i,hom}$ have been masked for $T > -35°C$ in the original 5-hour means; the ratio $\left[N^*_{i,het}/(N^*_{i,het} + N^*_{i,hom}) \cdot 100\right]$ has been computed and then averaged over time and longitude. The numbers on the top right of the plots are global means (in %); the isotherms at 0°C and −35°C are annual means.

clearly higher (twice globally) than the concentrations in COMP (Figure 5.3d). Indeed, being homogeneous nucleation excluded in HET, more water vapour is available for ice nucleation from INPs. $N^*_{i,het}$ in the cirrus regime in HOM and $N^*_{i,hom}$ in HET are zero by definition (Figures 5.3f and 5.3g).

Finally, the percentage contribution of heterogeneous nucleation in the cirrus regime has been computed for the simulations PRECOM and COMP (Figure 5.4). The results show that, globally, about 30% of the total new ICs are formed via immersion/condensation and deposition nucleation. The same result was found by Barahona et al. (2014), who used GEOS-5 and BN09 (with P13) and showed that the global relative contribution of homogeneous nucleation was about 70%. We observe that heterogeneous nucleation is more important in the NH, as already noted in Figure 5.3 and by Liu et al. (2012), Barahona et al. (2014), and Shi et al. (2015). Furthermore, it is visible that the heterogeneous nucleation contribution is higher in PRECOM than in COMP. This is another prove of the fact that the PREICE in PRECOM decreases significantly the homogeneous nucleation rates and only slightly the heterogeneous nucleation rates (as remarked in the previous subsection).

5.3 Summary and discussion

The new configuration BN+BN has been applied in order to study the competition for water vapour between homogeneous and heterogeneous nucleation and the water vapour depletion by pre-existing ice crystals in EMAC. For these purposes, the in-cloud ICNCs and the concentrations of newly-formed ICs predicted by the four simulations PRECOM, COMP, HOM, and HET (see Table 5.1) have been analysed.

The results point out the important role of the PREICE and, at the same time, the weak effect of the water vapour competition between the ice nucleation mechanisms. In line with other model results (e.g. Kuebbeler et al., 2014; Shi et al., 2015; Zhou et al., 2016), we found a significant reduction of new ICs produced via homogeneous nucleation because of the PREICE, causing a decrease in the $\mathrm{ICNC}_{\mathrm{in-cloud}}$ as well. By contrast, the PREICE has a very small effect on the new ICs formed heterogeneously, especially in the mixed-phase regime. The weak water vapour competition between homogeneous and heterogeneous implies that homogeneous nucleation is the dominant mechanism in cirrus clouds, as found by Liu et al. (2012), Kuebbeler et al. (2014) and Zhou et al. (2016), and also during some flight campaigns (e.g. Krämer et al., 2016; Voigt et al., 2017). These findings confirm the hypothesis that the main cause of the ICNC reduction in BN+LD and BN+BN with respect to KL+LD and KL+BN (Chapter 4) is the PREICE, rather than the water vapour competition.

Focusing on the newly-formed ICs (per integration time), we observed that $N^*_{i,hom}$ is higher than $N^*_{i,het}$ by orders of magnitudes (up to 10^2 in the tropics at high altitudes and up to 10^4 in the SH at high latitudes). $N^*_{i,het}$ is characterised by higher concentrations in the NH hemisphere, where INPs are more abundant, and also at very high altitudes (the analysis concerning the contributions of different aerosol components to $N^*_{i,het}$ is presented in the next chapter).

Similarly to Barahona et al. (2014), the global mean contribution of new the ICs formed heterogeneously with respect to the total new ICs generated in the cirrus regime is $\sim 32\%$ in COMP and slightly higher in PRECOM, because of the PREICE.

Finally, we found that the $\mathrm{ICNC}_{\mathrm{in-cloud}}$ profile as a function of temperature (and pressure) computed for HET constitutes a particular case. In fact, the concentrations are extremely low ($0.2-0.4\,\mathrm{L}^{-1}$) in cold cirrus clouds and higher than the ones predicted by the other simulations at higher temperatures. It is possible that convective detrainment and instantaneous freezing, two sources of ICs which result to be stronger in HET than in COMP, contribute to cause the observed higher concentrations at relative higher subfreezing temperatures.

Chapter 6

Aerosol contributions on heterogeneous nucleation

The analysis in this chapter focuses on the contributions of different aerosol types (dust, black carbon, glassy organics, and bioaerosols) to immersion/condensation and deposition nucleation. A large number of modelling studies have addressed the influence of aerosols on ice nucleation. Mineral dust has been the most studied species (e.g. Liu et al., 2012; Kuebbeler et al., 2014; Hendricks et al., 2011), as it is considered the most efficient INP, together with black carbon (e.g. Lohmann and Hoose, 2009; Hendricks et al., 2011). Similarly to this thesis, Barahona et al. (2014) took into account the contributions from dust, black carbon, and soluble organics by using GEOS-5 with BN09 and P13, however, they did not simulate biological aerosols. Hoose et al. (2010b) introduced an INP parameterization based on the CNT for the three components dust, soot, and bioaerosols, which were differentiated in bacteria, fungal spores, and pollen. To the best of our knowledge, there are no studies performed with GCMs which include the simultaneous influence of four aerosol types and analyse their individual contributions to heterogeneous ice nucleation. It must be also mentioned that, as far as we know, this is the first time that the individual contribution of glassy organics to heterogeneous nucleation is presented in relation to other aerosol components. In fact, Barahona et al. (2014) studied the impact of OCs via P13 on global radiation, without considering the OC individual contribution to ice nucleation, while Barahona et al. (2010) simulated the concentrations of new ICs derived from OCs using the parameterization of Murray et al. (2010), which considers only the OC component (neglecting DU, BC, and BIO).

By means of the simulation described in Section 6.1, the concentrations of new ice crystals nucleated from dust, black carbon, glassy organics, and bioaerosols are investigated in Section 6.2. The discussion and the presentation of the final results are given in Section 6.3.

6.1 Simulation setup

The simulation PRECOM described in Section 5.1 has been considered again in this chapter to investigate the individual contributions to heterogeneous nucleation by the four aerosol groups defined in the parameterization of Phillips et al. (2013), i.e. DU, BC, OC, and BIO. Actually, PRECOM has been run for 11 years (instead of 6), so 10 years have been considered for the analysis. The emissions of the four aerosol types are briefly described below.

- Dust is emitted offline using monthly emissions from AEROCOM (Dentener et al., 2006);
- Black carbon and organic compounds are emitted offline according to the GFEDv3.1 database (van der Werf et al., 2010) for the emissions of biomass burning and the CMIP5-RCP4.5 database (Clarke et al., 2007) for the anthropogenic emissions;
- Bioaerosols are simulated online as passive tracers, i.e. they do not interact with other aerosols, but their concentrations are influenced by processes such as dry deposition and scavenging. They are divided in three species: bacteria, fungal spores, and pollen. Bacteria are emitted using the constant best-estimate values from Burrows et al. (2009) for different ecosystems, e.g. savanas, crops, and grasslands. Fungal spore emissions are parameterized according to Heald and Spracklen (2009), while pollen emissions follow the parameterization proposed by Jacobson and Streets (2009). These particles are assumed to be spherical and monodisperse, with diameters of 1 μm for bacteria, 5 μm for fungal spores, and 30 μm for pollen, like in Hoose et al. (2010b,a).

6.2 Model results

6.2.1 Aerosol groups

The P13 parameterization computes the concentrations of the new ICs heterogeneously derived via immersion/condensation and deposition nucleation from DU, BC, OC, and BIO. In PRECOM, DU is given by the sum of accumulation and coarse insoluble modes of mineral dust, BC corresponds to the black carbon particles emitted from anthropogenic sources and fires in the insoluble Aitken mode, OC is given by the sum of Aitken, accumulation and coarse soluble modes, and BIO includes the insoluble bacteria, fungal spores, and pollen.

Figure 6.1 illustrates the annual zonal means of the number concentrations associated to the four aerosol groups. Together with Figure A.10 (in Appendix A.4), it is clearly visible that concentrations of DU and BC are higher in the NH, where deserts and anthropogenic sources are more extended, than in the SH. The highest values of DU between 10°N and 30°N are mainly caused by the emissions from the Sahara (Figure A.10 in Appendix A.4). The concentrations of OC are the highest in the upper troposphere due to the abundant presence of OCs in the Aitken mode, while OCs in the accumulation (and coarse) mode are more numerous at lower altitudes (Figure A.11 in Appendix A.4). The zonal means of DU, BC, and OC are

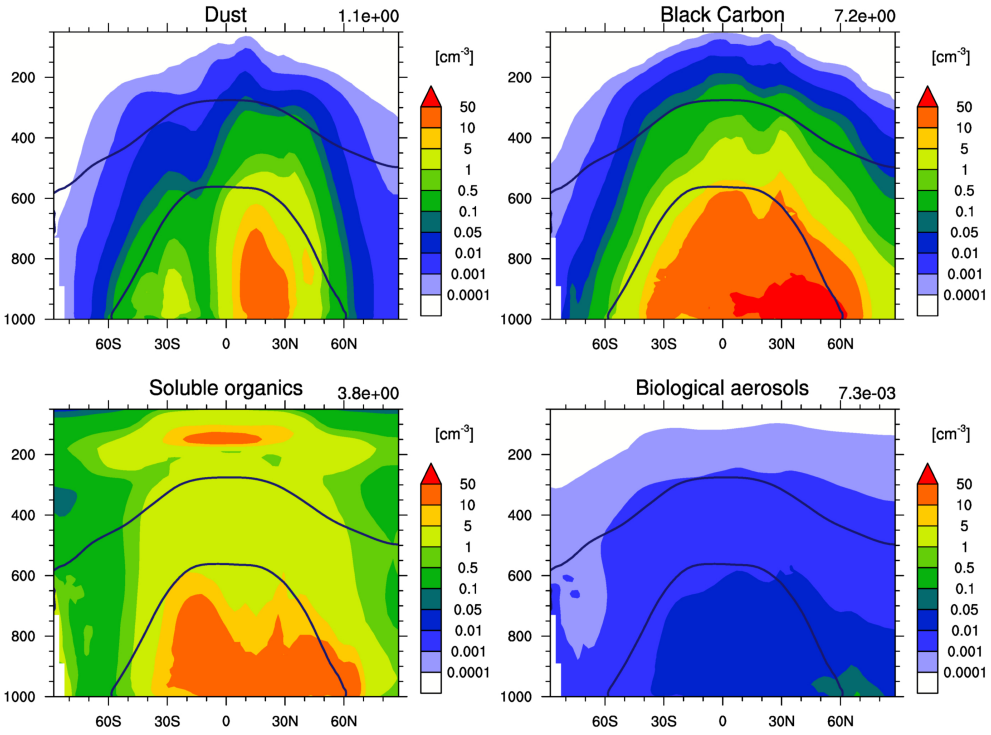

Figure 6.1: Annual zonal means of number concentrations of dust, black carbon, soluble organics, and bioaerosols. The numbers on the top right of the plots are global means (in cm^{-3}); the isotherms at 0°C and −35°C are annual means.

well comparable with the concentrations simulated, for instance, by Yun and Penner (2012), although their OC concentrations do not show a local maximum in the upper troposphere like Figure 6.1. Globally, BIO concentrations are lower than BC concentrations by a factor of 1000 and are higher in the NH, like DU and BC. The concentrations of each bioaerosol species (Figure A.12 in Appendix A.4) are comparable with the concentrations simulated in Hoose et al. (2010b,a). Bacteria are the most numerous bioaerosols: they are more abundant in the NH and can lift up to the upper troposphere. The concentrations of fungal spores are lower than bacteria and are maximum over tropical forests. Pollen particles cannot lift to high altitudes given their big size and, thus, their fast sedimentation, and their concentrations are several orders of magnitude lower than bacteria and fungal spore concentrations.

We recall that only a small subset of the aerosols shown in Figure 6.1 serve as INPs. Furthermore, P13 assumes that only a fraction of soluble OCs becomes glassy (i.e. $g_{glass} = 0.5$, see Subsection 3.1.2) at temperatures lower than −65°C, thus, all the OCs at higher temperatures do not play a role as INPs.

6.2.2 Global means of new ICs

The relative contributions of the four aerosol groups to the total new ICs formed heterogeneously are shown in Figure 6.2, with the means of $N^*_{i,het}$ (i.e. $N_{i,het}$ per integration time) also listed. The means are higher in the NH than in the SH. Especially the relative contribution of

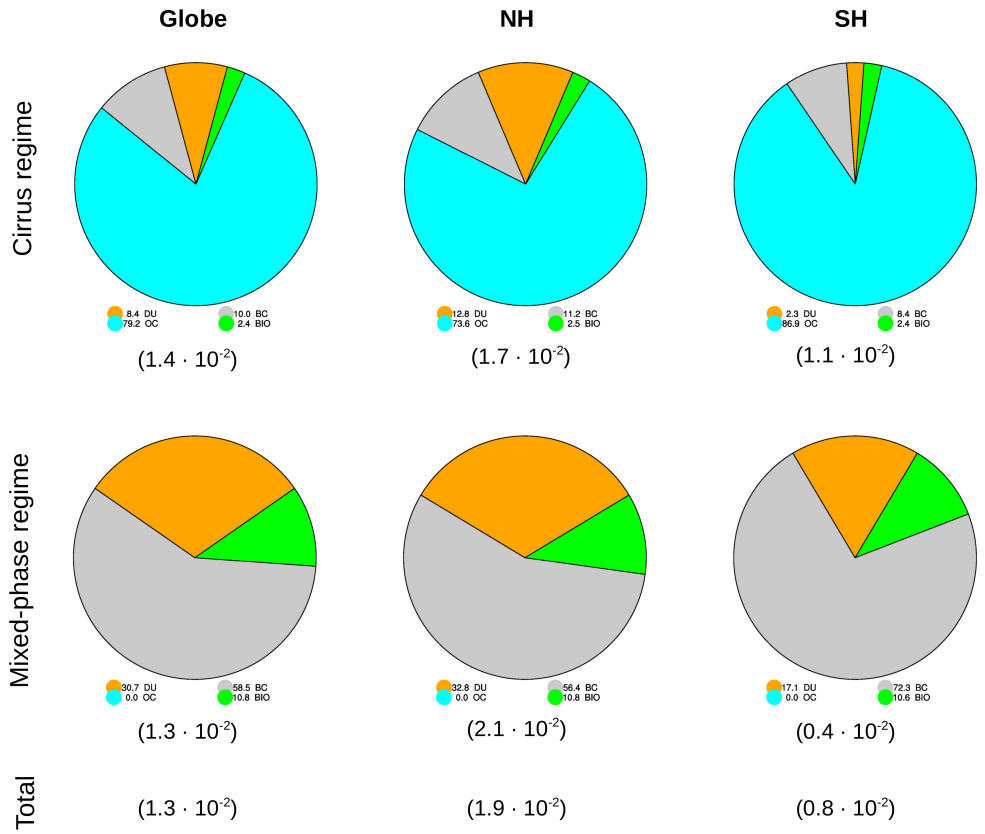

Figure 6.2: The pie charts represent the relative contributions (in %) of dust, black carbon, soluble organics, and bioaerosols to the total $N^*_{i,het}$ in the cirrus regime (*first row*) and in the mixed-phase regime (*second row*), considering the entire globe, the NH, and the SH. The numbers in brackets are the means of the total $N^*_{i,het}$ (in L^{-1} per integration time) computed in the cirrus regime, in the mixed-phase regime, and without differentiation between cloud regimes (*last row*). Note that the means of $N^*_{i,het}$ are computed considering only areas where $N^*_{i,het} > 0$.

DU is higher in the NH, at the expense of BC in the mixed-phase regime and OC in the cirrus regime. Indeed, DU presents the most asymmetric distribution between the two hemispheres, as shown in Figure 6.1.

It is evident that the new ICs formed from BC dominate in the mixed-phase regime ($> 55\%$), while the ones formed from OC prevail in the cirrus regime ($> 70\%$). This result is influenced by the fact BC is the most abundant aerosol type in the lower troposphere, while OC is the main provider of INP in the upper troposphere (Figure 6.1). Phillips et al. (2013) showed that BC can actually comprise most of the INPs in the mixed-phase regime, instead of DU. Nevertheless, the only modelling study (to our knowledge) which presents the individual aerosol contributions to the total new ICs by using P13 (Sullivan et al., 2016) shows that DU is the most important INP. Interestingly, BIO is responsible for the formation of $\sim 10\%$ and $\sim 2\%$ of the new ICs in the mixed-phase regime and in the cirrus regime, respectively, in contrast to Hoose et al. (2010b) who found that the bioaerosol contribution is

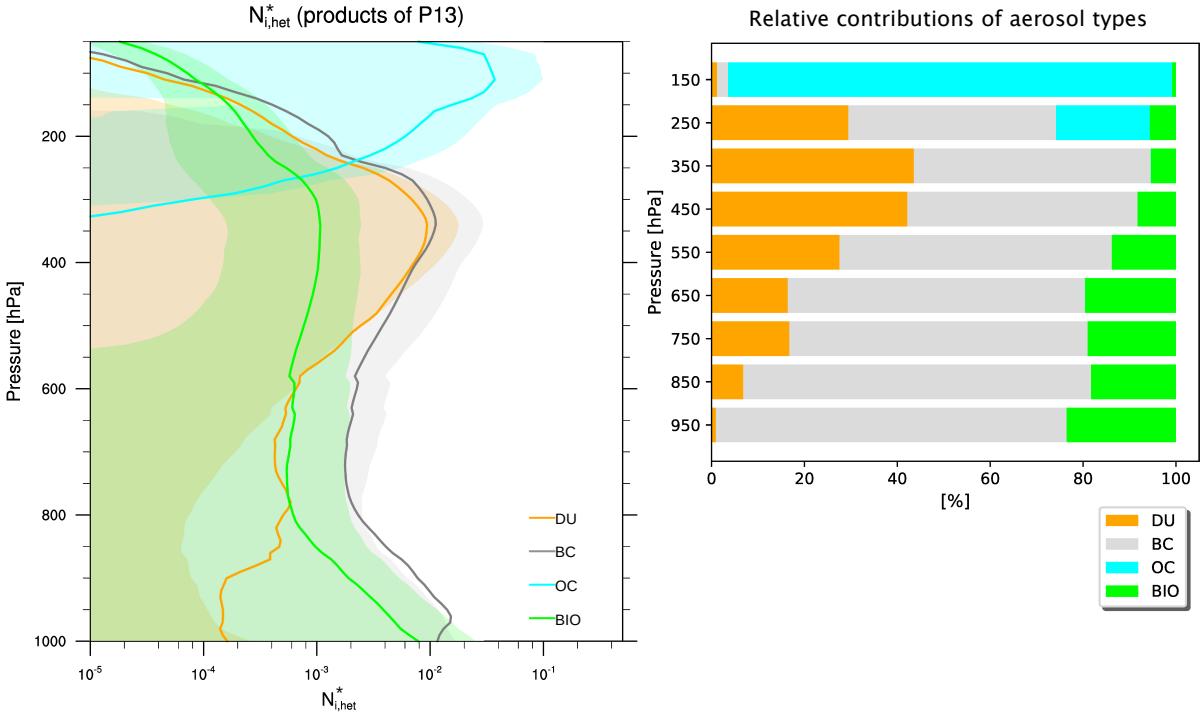

Figure 6.3: (*Left*) Global means of $N^*_{i,het}$ (in L^{-1} per integration time) derived from dust, black carbon, soluble organics, and bioaerosols as functions of pressure. The means are computed considering only areas where $N^*_{i,het} > 0$ in bins of 10 hPa. Coloured shadows indicate the 10th and 90th percentiles. (*Right*) Percentage contributions of DU, BC, OC, and BIO to the total $N^*_{i,het}$ computed in bins of 100 hPa.

marginal (10^{-5}%).

The concentrations per integration time of the new heterogeneously-formed ICs are shown as functions of pressure in Figure 6.3. It is interesting to note that the large OC contribution in the cirrus regime observed in Figure 6.2 is due to the fact that OC is the only responsible of heterogeneous nucleation at pressures lower than 200 hPa. Below 500 hPa, DU and BC produce similar concentrations of new ICs, with peak at 350 hPa. At higher pressures, the contribution of DU becomes less important, while the one of BC remains the most dominant. Furthermore, relative contributions of BIO increase towards low altitudes, so BIO is responsible for more than 20% of the new ICs formed between 900 and 1000 hPa.

6.2.3 Zonal means of new ICs

In order to analyse how the new ICs are globally distributed, the annual zonal means are considered in this subsection. Figure 6.4 shows the annual zonal means of the vertically integrated concentrations (per integration time) of the new ICs derived from the four aerosol groups. The singular feature is given by the new ICs originated from OC. In fact, their concentrations are much higher than the other groups almost everywhere, although they are limited in the upper troposphere (as observed in Figure 6.3). Furthermore, they are symmetric between the two

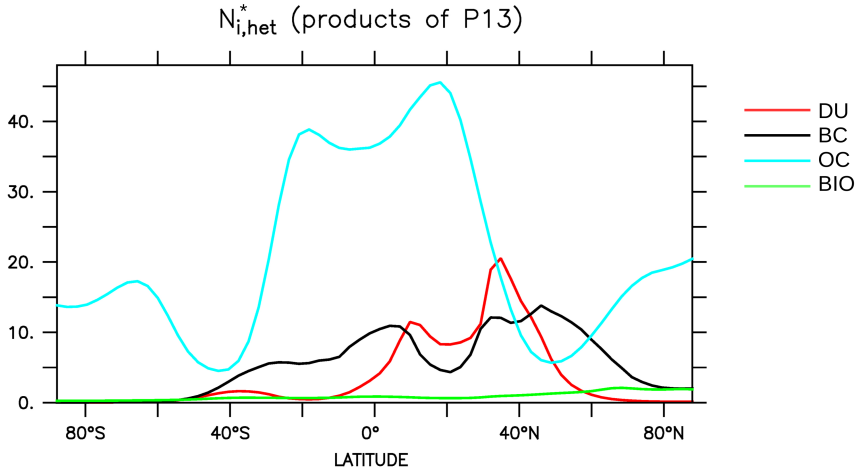

Figure 6.4: Annual zonal means of the vertically integrated $N^*_{i,het}$ derived from dust, black carbon, soluble organics, and bioaerosols. The unit of the vertical axis is: 10^4 m^{-2} per integration time.

hemispheres and especially high between the tropics, with two peaks at 20°S and 20°N. The new ICs derived from DU and BC are in similar concentrations. Nevertheless, the ones from DU are more concentrated in the NH with two peaks around 10°N and 35°N, in correspondence with the dust emissions from the Sahara and the Asian deserts (Figure A.10 in Appendix A.4). Finally, the new ICs from BIO present very low concentrations, which slightly increase towards higher latitudes in the NH.

The annual zonal means in Figure 6.5 better explain $N^*_{i,het}$ derived from different aerosol types as function of pressure, and their ratios over the annual zonal mean of the total $N^*_{i,het}$ in Figure 6.6 show the individual relative contributions of each aerosol component. The peak observed in Figure 6.3 for the new ICs derived from DU at around 350 hPa is principally due to the new ICs formed in the NH. More than 60% of the new ICs between the equator and 40°N derives from DU. Such ICs are spread over the Sahara and, in particular, the Gobi Desert (Figure A.13 in Appendix A.4).

As already observed, BC results to be an INP more important than DU, especially in the mixed-phase regime. In fact, BC is basically the only INP between 40°N and 70°N at low altitudes, probably due to the high BC emissions from South Asia and East Asia (Figure A.10 in Appendix A.4). It is also responsible for more than 70% of the new ICs between the equator and 30°S, because of the high concentrations over the Amazonian and Congo regions (Figure A.13 in Appendix A.4).

On the other hand, OC plays definitely a more important role in the upper troposphere, so that it is the only source of new ICs heterogeneously-formed at pressures lower than 200 hPa. The new ICs derived from glassy organics show a large maximum between the tropics as Barahona et al. (2010), who used the parameterization of Murray et al. (2010) for glassy organics. From the annual zonal means as a function of temperature (Figure A.14 in Appendix

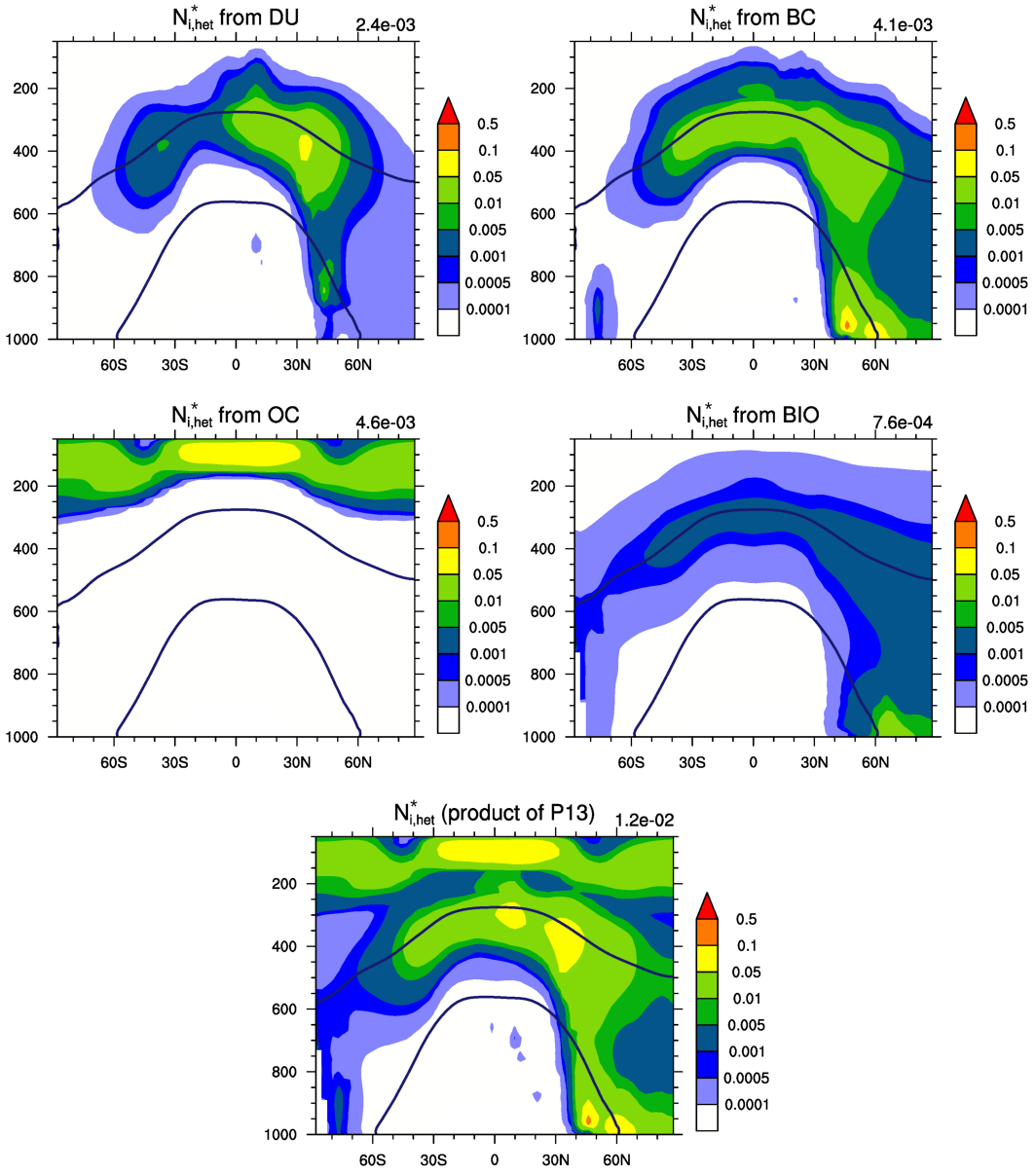

Figure 6.5: Annual zonal means of $N^*_{i,het}$ (in L^{-1} per integration time) derived from dust, black carbon, soluble organics, and bioaerosols and the total $N^*_{i,het}$ as functions of latitude and pressure. The means are computed considering only areas where $N^*_{i,het} > 0$. The numbers on the top right of the plots are global means (in L^{-1} per integration time); the isotherms at 0°C and −35°C are annual means.

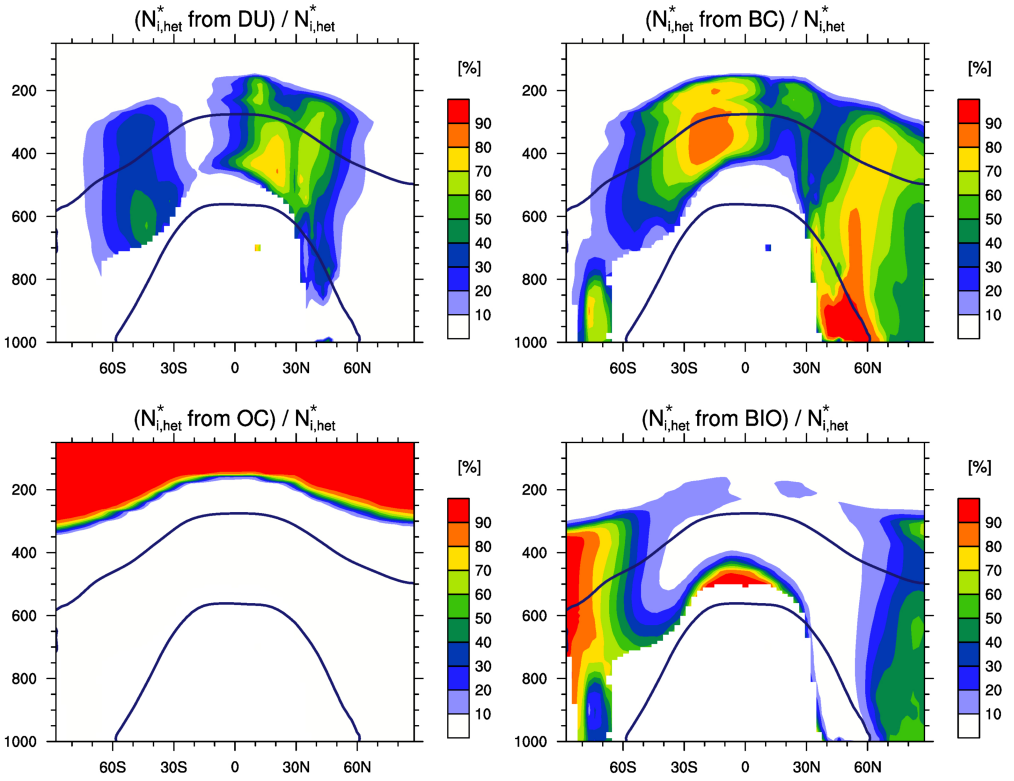

Figure 6.6: Percentage contributions of the new ICs derived from the aerosol groups DU, BC, OC, and BIO to the total $N^*_{i,het}$. They are the ratios of the plots of Figure 6.5, displayed for areas where $N^*_{i,het} > 10^{-4}$ L^{-1} per integration time.

A.4) it is easy to discern the important contribution of OC at temperatures lower than −60°C in the TTL, as predicted by Wilson et al. (2012).

Finally, BIO generates new ICs along all the latitudes, especially in the mixed-phase regime and in the NH. Its individual contribution to the total $N^*_{i,het}$ is very small between 40°S and 60°N but can increase locally, up to 60% at higher latitudes in the NH and more than 70% in the SH (at pressures higher than 200 hPa where OCs do not play a role as INPs). This is likely due to the high onset temperature associated to BIO in P13 with respect to DU and BC (see Table 3.1).

6.3 Summary and discussion

The concentrations of the new ice crystals formed via immersion/condensation and deposition nucleation from dust, black carbon, glassy organics, and bioaerosols have been investigated by means of the 10 year-long PRECOM simulation.

We found that DU contribution is larger in the NH than in the SH because of the emissions from the Sahara and the Gobi Desert. However, DU is not the principal source for heteroge-

neous nucleation, rather BC is the main INP. This is contrast with many modelling studies (e.g. Hoose et al., 2010b; Yun and Penner, 2012; Kuebbeler et al., 2014; Sullivan et al., 2016) and field measurements (e.g. Pratt et al., 2009; Cziczo et al., 2013). Nevertheless, Murray et al. (2012) in their review concluded that dust and soot are of comparable importance for atmospheric ice nucleation at temperatures below −15°C because, despite the higher ice-nucleating ability of dust, soot particles are more numerous than mineral dust. In addition, our results are coherent with Phillips et al. (2013), who showed that BC can actually comprise most of the active INPs in the mixed-phase regime, instead of DU.

The contribution of OC to heterogeneous nucleation is predominant at pressures lower than 200 hPa. The new ICs derived from OC show a large maximum between the tropics, similarly to Barahona et al. (2010). Wilson et al. (2012) proved that heterogeneous nucleation by glassy aerosols may compete with ice nucleation on mineral dust particles in mid-latitudes cirrus of the TTL.

Finally, we found that the contribution of BIO plays always a role at global scale. BIO determines the formation of $\sim 10\%$ and $\sim 2\%$ of the new ICs in the mixed-phase regime and in the cirrus regime, respectively, and is responsible for $\sim 20\%$ of the new ICs formed at pressures higher than 600 hPa. The importance of BIO in nucleating ice in the atmosphere is still uncertain. Other modelling studies (e.g. Hoose et al., 2010a) and some field campaigns (e.g. Cziczo et al., 2013) suggest that bioaerosols cannot play a role as INP because of their limited emissions and their large dimensions which prevent them from lifting to freezing altitudes. However, other field campaigns, such as Pratt et al. (2009) and Voigt et al. (2017), found that bioaerosols constitute a considerable fraction (33% and 6%, respectively) of the ice residuals.

A large number of modelling studies have addressed the influence of aerosols on ice nucleation in the atmosphere (e.g. Lohmann and Hoose, 2009; Hoose et al., 2010b; Hendricks et al., 2011; Liu et al., 2012; Kuebbeler et al., 2014; Barahona et al., 2014), however, these studies are still controversial, as the quantification of the new heterogeneously-formed ICs is challenging. To the best of our knowledge, this is the first modelling study which analyses the individual contributions of four aerosol types to heterogeneous nucleation at the same time, including glassy organics. It must be mentioned that also other aerosol species have been identified as INPs. Abbatt et al. (2006) showed that solid ammonium sulfate aerosols can generate ice nucleation. More recently, Wilson et al. (2015) suggested that marine organic material may be an important source of INPs in remote marine environments, such as the Southern Ocean, North Pacific Ocean, and North Atlantic Ocean.

Chapter 7

Tendencies of cold cloud (micro)physical processes

The tendencies of physical and microphysical processes related to ICNC in cold clouds are analysed in this chapter (the concept of tendency has been defined in Subsection 2.2.1). In this way, the contributions of the ice nucleation mechanisms are compared to the ones of other processes which lead to production or removal of ICs.

The sources and sinks of ICs identified in the CLOUD submobel are described in Section 7.1. The model results are presented in Section 7.2 and the conclusions in Section 7.3.

7.1 Methods

7.1.1 Identification of the partial ICNC tendencies

ICNC is a prognostic variable whose evolution is described via the equation 2.1. The CLOUD submodel defines the physical and microphysical evolution of ICNC, thus, it computes all the the R-terms of the equation apart the rate related to advective, turbulent, and convective transport. Every time a (micro)physical process i affects the number of ICs in CLOUD, ICNC is updated by a quantity ΔICNC_i.

We define the *partial ICNC tendency due to a specific cold cloud (micro)physical process* i (in $\text{m}^{-3}\ \text{s}^{-1}$) as:

$$\partial_t \text{ICNC}_i = \frac{\Delta\text{ICNC}_i}{\Delta t} \ ,$$

where Δt is the model integration time. Thus, the *individual tendency of ICNC* due to CLOUD (see Subsection 2.2.1) is given by the sum of the partial ICNC tendencies:

$$\partial_t \text{ICNC}_{CLOUD} = \sum_i \partial_t \text{ICNC}_i \ .$$

In order to investigate the influence of the single processes affecting ICNCs, all ΔICNC_i have been identified within the code of CLOUD, and the corresponding partial tendencies (i.e. $\partial_t\text{ICNC}_i$) have been stored as output variables.

7.1.2 Description of the partial ICNC tendencies

The cold cloud (micro)physical processes associated to the partial ICNC tendencies identified in CLOUD are described below and listed in Table 7.1, divided in sources and sinks of ICs. Note that these processes and their parameterizations have been already introduced in Section 2.3.

Sources of ICs

- Convective detrainment.
  The new ICs originated from convective detrainment are estimated from the detrained cloud condensate in the ice phase (i.e. when $T < -35°C$) by assuming a temperature dependent radius. The detrainment of ICs is included in the transport term in equation 2.1 (Roeckner et al., 2004) but here is considered as an individual source.

- Ice nucleation in the cirrus regime.
  The new ICs formed via ice nucleation in the cirrus regime are the product of the ice nucleation parameterization used in this regime (i.e. BN09 with P13 in the PRECOM simulation). New ICs must be zero at the minimum and equal to the number concentration of the activated cloud droplets at the maximum.

- Ice nucleation in the mixed-phase regime.
  The new ICs formed via heterogeneous nucleation in the mixed-phase regime are the result of the ice nucleation parameterization(s) used in such regime: they are the sum of the ICs originated from contact, immersion/condensation, and deposition nucleation modes (i.e. the results of LD06 and P13 in PRECOM). The value of the new ICs has the number concentration of total aerosols as upper bound and must be zero when there is no cloud cover and cloud liquid water and CDNC are lower than some minimal values (i.e. 10^{-12} kg kg^{-1} and 40 cm^{-3}).

- Instantaneous freezing.
  This process refers to the instantaneous freezing of supercooled cloud droplets when $T < -35°C$: as soon as temperatures are below $-35°C$, all cloud droplets freeze. It is a sort of homogeneous nucleation which is not included in equation 2.1 but is considered as an individual source within the CLOUD submodel.

- Secondary ice production.
  The new ICs formed via secondary ice production are the ones derived from the Hallet-Mossop process (or rime splintering) between $-8°C$ and $-3°C$.

Sinks of ICs

- Melting.
  As soon as temperatures are above 0°C, all ICs melt.

Tendency	Description	Sign	Temperature
DETR	Convective detrainment	> 0	$T < -35°C$
NCIR	Ice nucleation in the cirrus regime	> 0	$T < -35°C$
NMIX	Ice nucleation in the mixed-phase regime	> 0	$-35°C < T < 0°C$
FREE	Instantaneous freezing	> 0	$T < -35°C$
SECP	Secondary ice production	> 0	$-8°C < T < -3°C$
MELT	Melting	< 0	$T > 0°C$
AGGR	Aggregation	< 0	$T < 0°C$
ACCR	Accretion	< 0	$T < 0°C$
SELF	Self-collection	< 0	$T < 0°C$
SEDI	Sedimentation	both	$T < 0°C$
MINMAX	Adjustments	both	$T < 0°C$

Table 7.1: Partial ICNC tendencies defined in the CLOUD submodel. The first column contains the abbreviations associated to each tendency; the second column describes the (micro)physical processes associated to the tendencies; the third column indicates the sign of the tendency (positive for sources and negative for sinks of ICs); the forth column specifies the temperature range in which the processes occur.

- Aggregation.
  By collision–coalescence, ICs can aggregate to produce snow planar flakes (IC + IC → Snow).

- Accretion.
  ICs can aggregate with falling snow flakes, thus, snow grows by accretion of ICs (Snow + IC → Snow).

- Self-collection.
  This process describes the collision–coalescence among hydrometeors of the same type (in this case ICs) leading to the formation of hydrometeors of the same type (IC + IC → IC).

Sources & sinks of ICs

- Sedimentation.
  This process impacts the ICNC vertical distribution and includes also sublimation of falling ICs which encounter an ice subsaturated region. Sedimentation is mainly a sink of ICs but also a source at low altitudes.

- "Adjustments".
  ICNCs are sometimes updated not because of the action of physical processes but to avoid unphysical situations arising from numerical instability, hence, some minimal and maximal ICNC values are imposed. We refer to these updates as "adjustments". Their sum is named "MINMAX" and is considered in this chapter, while the individual adjustments are described in Appendix A.5.

7.2 Model results

The 10 year-long PRECOM simulation described in Sections 5.1 and 6.1 has been considered for the analysis in this section. For simplicity, the abbreviations specified in Table 7.1 are used in the text.

7.2.1 Zonal medians

The partial ICNC tendencies associated to sources and sinks of ICs have been represented as functions of latitude and pressure. Given their asymmetric distribution, with a pronounced tail towards high values, the annual zonal medians are considered in Figures 7.1 and 7.2, while the annual zonal means are shown in Figures A.15 and A.16 (in Appendix A.5).

Among the sources of ICs in Figure 7.1, we observe that NCIR is the only source of ICs in the upper troposphere at pressures lower than 350 hPa and presents a maximum ($5 - 10$ m^{-3} s^{-1}) between the tropics (as expected from Figure 5.3). DETR contributes to produce ICs at pressures generally higher than 350 hPa (at $T < -35$°C) and shows a maximum (> 10 m^{-3} s^{-1}) above the equator. FREE is the highest source of ICs beyond the tropics at pressures where temperatures are just below -35°C. Globally, FREE is roughly two orders of magnitude higher than NCIR and one higher than DETR. We performed the same computations (not shown) with the KL+LD simulation (i.e. the one obtained with the standard configuration of the model, see Chapter 4), and we found that FREE is higher (more than double) than NCIR also in KL+LD. Hence, the instantaneous freezing plays an important role in EMAC regardless of the ice nucleation scheme applied for cirrus clouds.

In the mixed-phase regime, SEDI is the major source of ICs. It concerns the entire mixed-phase regime (i.e. the area between the two isotherms) and is globally of the order of 10^{-1} m^{-3} s^{-1} (like DETR and NCIR). NMIX affects the whole mixed-phase regime and is symmetric between the hemispheres. By definition, NMIX is the rate of ice crystal formation via immersion/condensation and deposition nucleation as well as contact nucleation. As the concentrations of the new heterogeneously-formed ICs are higher for contact nucleation than immersion nucleation (see Subsection 5.2.2), the NMIX pattern is similar to the one of the CDNCs (not shown). SECP is more concentrated at lower altitudes, as the secondary ice production occurs at -8°C $< T < -3$°C. Furthermore, SECP shows a maximum in the SH and a local maximum above the equator, as a consequence of the snow crystal distribution (not shown). NMIX and SECP are globally of the order of magnitude of 10^{-2} m^{-3} s^{-1}.

We found that the zonal means of the partial ICNC tendencies (Figure A.15, Appendix A.5) are higher than the zonal medians in Figure 7.1. While the means of NCIR are close to the medians, the means of FREE are one order of magnitude higher than the medians. This implies that very high concentrations of supercooled cloud droplets can sometimes freeze instantaneously (as it will be remarked in the next subsection). Furthermore, the zonal means of NCIR are characterised by two local maxima between 30° and 40° in both hemispheres around 800 hPa, like $N^*_{i,hom}$ in Figure 5.3. Interestingly, also FREE presents similar local

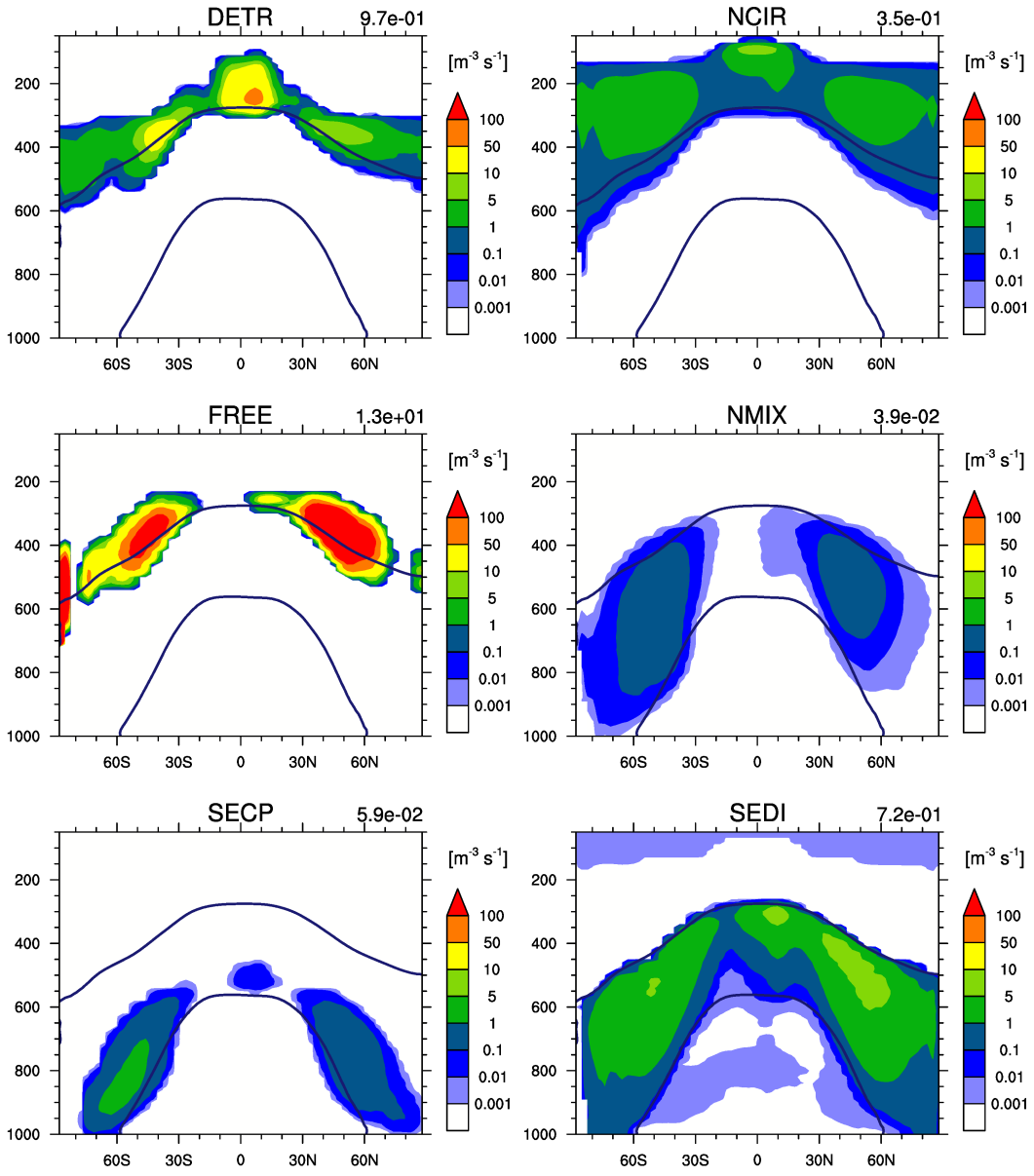

Figure 7.1: Annual zonal medians of the partial ICNC tendencies associated to cold cloud IC sources. The numbers on the top right of the plots are means of the illustrated zonal medians (in $m^{-3}\ s^{-1}$); the isotherms at 0°C and −35°C are annual means; the titles are described in Table 7.1. Note that SEDI takes into account only positive values.

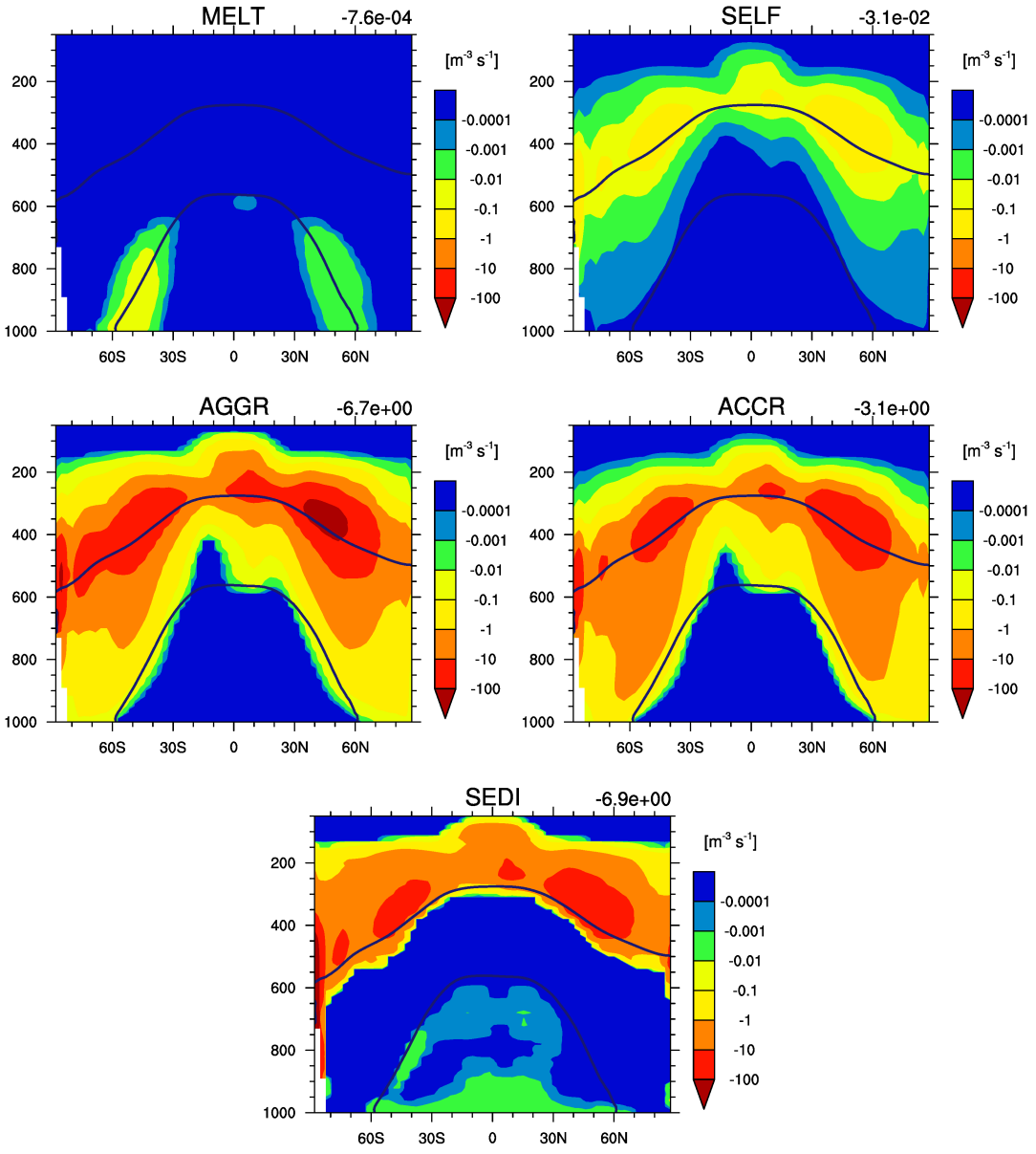

Figure 7.2: Like Figure 7.1 but for cold cloud IC sinks. Note that SEDI takes into account only negative values.

maxima.

Globally, SEDI is the most important sink of ICs and is efficient especially in the upper troposphere (Figure 7.2). AGGR and ACCR are also important, of the same order of magnitude as SEDI (10^0 m^{-3} s^{-1}). Their patterns are symmetric between the hemispheres, with higher values over the equator and between 30° and 60°, along the border of the cloud regime transition (this feature will be stressed in Figure 7.3, bottom). SELF presents a similar pattern to AGGR and ACCR but is generally two orders of magnitude lower. Finally, MELT is the weakest sink of ICs (four orders of magnitude lower than AGGR and ACCR).

As found for the sources of ICs, the zonal means of the IC sinks (Figure A.16 in Appendix A.5) are also higher than the zonal medians in Figure 7.2. Interestingly, the zonal means of all sinks are higher in the NH than in the SH, with a peak around 30°N in correspondence of the Tibetan Plateau, where ICNCs are also higher (see Figure 4.1a). Indeed, mountain chains affect ICNCs (see Section 4.2), which in turn impact the removal processes.

7.2.2 Vertical profiles

The partial ICNC tendencies have been further investigated by computing their global medians and their relative contributions as functions of pressure and temperature (Figure 7.3).

As expected from Figures 7.1 and 7.2, in the upper troposphere (at pressures < 200 hPa) NCIR and SEDI are the only acting processes, competing against each other (Figure 7.3, top). Below, ACCR and AGGR start to become important, with a peak around 350 hPa, DETR is also maximum around 350 hPa, and SEDI shifts from sink to source of ICs between 400 hPa and 450 hPa. Only some of the 75th percentiles of NMIX, FREE, SECP, MELT, and SELF can be distinguished, while their relative contributions (in the bar chart) are negligible in comparison to the other processes. To be noted that the profiles of the tendencies could substantially change if considering specific areas instead of the entire globe, as shown in Gettelman et al. (2013). Interestingly, we found that the contributions of the so-called MINMAX tendency (plotted only in the bar charts) are around 4% in most of the pressure levels, and so higher than the contributions of DETR, FREE, SECP, MELT, and SELF, and much higher at pressures > 700 hPa.

Although the profiles as functions of temperature in Figure 7.3 (bottom) are global medians of the same tendencies analysed before, some interesting features can be observed. NCIR and SEDI are the only acting processes at $T < -50$°C, while the other processes compete against each other at higher temperatures. AGGR, ACCR, SELF, SEDI, FREE, and DETR present their maximum between -30°C and -40°C, although the relative contributions (in the bar chart) of SELF and DETR are negligible. Another distinctive feature is the huge peak of FREE, which makes the instantaneous freezing the main source of ICs in this temperature range (i.e. -40°C $< T < -30$°C). At higher temperatures, SEDI becomes the main source (as already observed in Figure 7.1), NMIX has only a marginal contribution, and SECP is important only at $T > -10$°C.

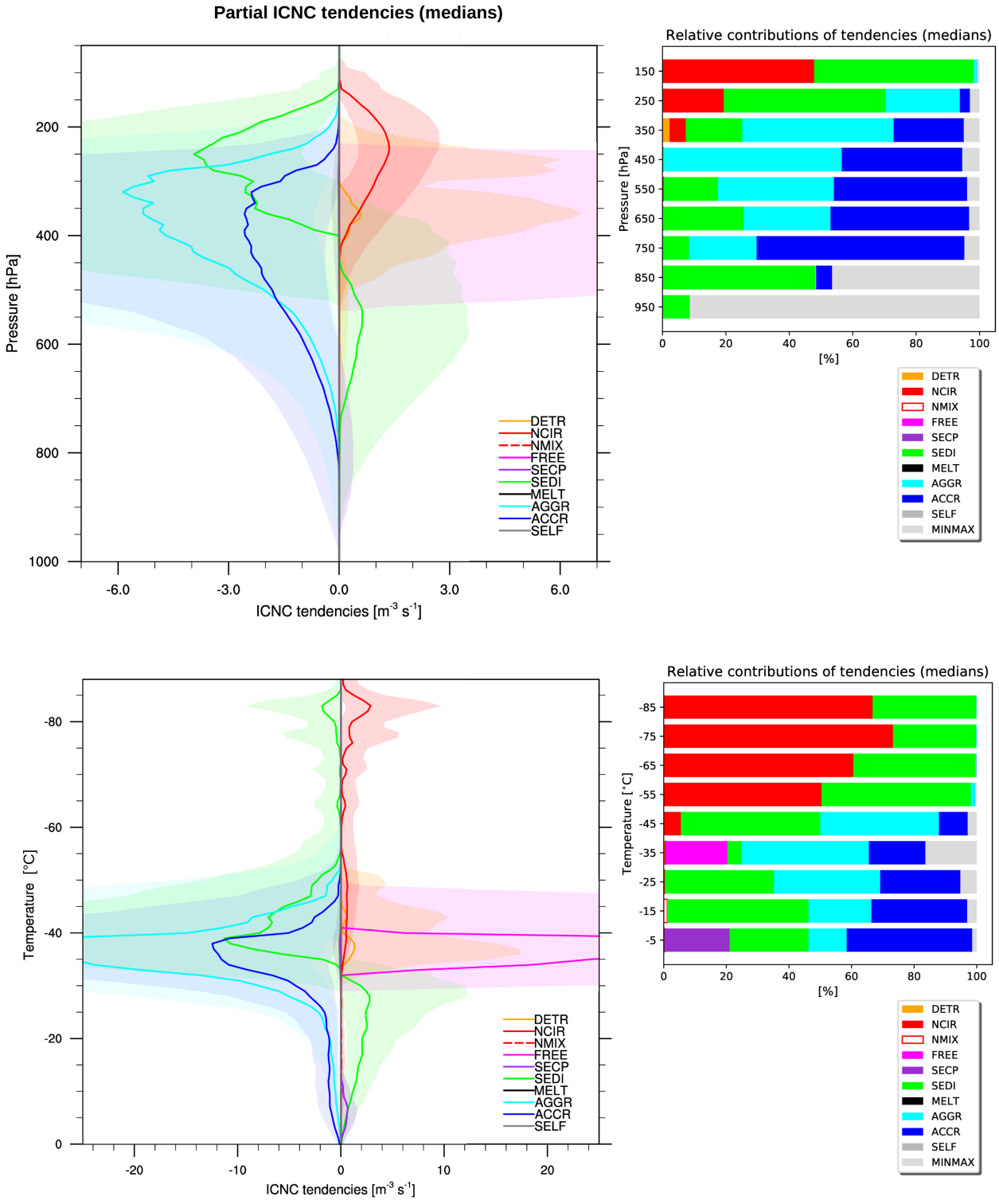

Figure 7.3: Partial ICNC tendencies as functions of pressure (*top*) and as functions of temperature (*bottom*). The vertical profiles (*left*) are annual global medians and the coloured shadows mark the areas between the 25th and 75th percentiles. The profiles on the left hand side of the plot are sinks of ICs, while the ones on the right hand side are sources of ICs. The bar charts (*right*) represent the percentage contributions of the partial ICNC tendencies to the individual tendency of ICNC (including MINMAX) based on global medians computed in bins of 100 hPa (*top*) and in bins of 10°C (*bottom*).

The global means of the ICNC partial tendencies computed as functions of pressure and temperature (Figure A.17 in Appendix A.5) point out that all the means are well beyond the 75th percentiles (apart the case of NCIR). Furthermore, it is remarkable how the FREE contributions change from considering global medians, where FREE contributes by $\sim 20\%$ only between $-40°C$ and $-30°C$ (Figure 7.1, bottom), to considering global means, where FREE contributes by $\sim 50\%$ in the intervals $250 \div 950$ hPa and $-60°C \div -20°C$. Similarly, also the global medians and global means of MINMAX vary considerably.

7.3 Summary and discussion

The partial ICNC tendencies of physical and microphysical processes related to ICNC in cold clouds have been identified in the CLOUD submodel and investigated. The tendencies have been divided in sources of ICs (convective detrainment – DETR, ice nucleation in the cirrus regime – NCIR, ice nucleation in the mixed-phase regime – NMIX, instantaneous freezing – FREE, secondary ice production – SECP, and sedimentation – SEDI) and sinks of ICs (melting – MELT, aggregation – AGGR, accretion – ACCR, self-collection – SELF, and SEDI). Additionally, all the tendencies not associated to physical processes have been identified (and described in Appendix A.5). To the best of our knowledge, this is the first study where all the (micro)physical processes related to ICNCs have been considered. In fact, Lohmann et al. (1999) computed only the vertically integrated tendencies associated to sources and sinks of cloud droplets, while Gettelman et al. (2013) presented only some of the tendencies associated to the cold cloud microphysical processes because they principally focused on rain formation processes.

We found that NCIR is the only source of ICs in the upper troposphere, while both NCIR and DETR are sources in the cirrus regime at pressures higher than 350 hPa, with a peak between the tropics. Beyond the tropics, at temperatures just below $-35°C$, FREE is the most efficient source of ICs. In the mixed-phase regime, the main source of ICs is SEDI, while NMIX and SECP are in absolute the weakest sources of ICs.

The most efficient sinks of ICs are SEDI (especially in the upper troposphere), AGGR, and ACCR, which are globally of the order of 10^0 m^{-3} s^{-1}. In comparison with these, SELF is much less important ($\sim 10^{-2}$ m^{-3} s^{-1}), and MELT is negligible ($\sim 10^{-4}$ m^{-3} s^{-1}).

Large differences in the tendency distributions have been found: some are very skewed (like the case of FREE), others are more balanced (like the case of NCIR). Specifically, the vertical profiles of FREE show that its global median counts only for $\sim 20\%$ between $-40°C$ and $-30°C$, while its global mean counts for $\sim 50\%$ in the interval $-60°C \div -20°C$ (and $250 \div 950$ hPa). This implies that very high concentrations of supercooled cloud droplets can sometimes freeze instantaneously in EMAC.

Overall, the production of ICs is more efficient in the cirrus regime than in the mixed-phase regime. In particular, NMIX and SECP are the lowest sources of ICs. As a consequence, the

effects due to changes in the parameterizations of heterogeneous nucleation and secondary ice production can be strongly smoothed by the action of other (micro)physical processes. This aspect must be taken into account, for instance, when one investigates the influence of different aerosol components to the total ICNCs or cloud radiative effects (rather than to the total new ICs formed heterogeneously, as in Chapter 6). Nevertheless, this is valid for the EMAC model run with the setup of PRECOM. It has been mentioned that changing the ice nucleation scheme in the cirrus regime, NCIR changes and, consequentially, also the relative contributions of the other processes. Therefore, this study points out the importance of performing the analysis of the partial ICNC tendencies in order to correctly identify the main processes responsible for production and removal of ICs. Moreover, the study has pointed out the presence of some physical constraints (i.e. the MINMAX tendency) which can have impact as much as some (micro)physical processes.

Chapter 8

Summary and outlook

Summary

In this thesis, we discussed the implementation of a comprehensive ice nucleation parameterization in the global chemistry-climate model EMAC and the analysis of the modelled ice crystal number concentrations. In particular, the ice nucleation scheme of Barahona and Nenes (2009b, BN09) has been implemented in EMAC in order to improve the numerical representation of ice nucleation and ice crystal number concentration. The standard EMAC configuration used so far simulates ice nucleation via the parameterizations of Kärcher and Lohmann (2002b, KL02) and Lohmann and Diehl (2006, LD06). The first one assumes that homogeneous nucleation is the only mechanism which nucleates ice in cirrus clouds, while LD06 simulates heterogeneous nucleation in mixed-phase clouds, i.e. immersion nucleation due to dust and black carbon and contact nucleation with dust. On the other hand, without additional computational resources, the BN09 parameterization takes into account processes which are neglected by KL02 and LD06 (Section 3.1). In fact, BN09 computes the competition for water vapour between homogeneous and heterogeneous nucleation in the cirrus regime. By applying the INP parameterization of Phillips et al. (2013), BN09 considers the influence of four aerosol types (dust, black carbon, soluble organics, and bioaerosols) to immersion/condensation and deposition nucleation. Additionally, the BN09 algorithm has been modified in order to include the water vapour depletion due to depositional growth of pre-existing ice crystals (Section 3.2). Therefore, applying BN09 makes the EMAC model one of the few GCMs which take into account the complexity of ice nucleation in a detailed manner.

The model performance obtained by using BN09 in different cloud regimes (i.e. in the cirrus and/or in the mixed-phase regime) has been analysed and compared with the standard configuration of EMAC (Chapter 4). We found that BN09 operating in the cirrus regime determines a strong reduction of ICNCs in the upper troposphere because of the water vapour competition between the ice nucleation mechanisms but especially because of the pre-existing ice crystal effect (PREICE). Changing the ice nucleation scheme in the cirrus regime generates larger differences of ICNC and IWC than changing parameterization in the mixed-phase

regime.

The comparison against a large collection of flight measurements in cirrus clouds has pointed out that KL02 overestimates ICNCs. Differently, BN09 applied in the cirrus regime predicts ICNCs which well agree with the observations in cold cirrus clouds but are underestimated between $-73°C$ and $-53°C$, because of an overestimation of the PREICE.

Overall, the model configuration which applies BN09 in both cloud regimes allows a better description of the ice nucleation mechanisms and well agrees with the observations, thus, it has been used for further investigations.

By studying the competition for water vapour between homogeneous and heterogeneous nucleation and the effect of pre-existing ice crystals (Chapter 5), we found that the PREICE is the main cause of the ICNC reduction in the upper troposphere and high latitudes. Indeed, the PREICE strongly reduces the concentrations of the new ICs nucleated homogeneously. On the other hand, the competition for water vapour between the ice nucleation mechanisms is very weak, therefore, homogeneous nucleation is the dominant mechanism in cirrus clouds.

Focusing on the concentrations of the new ICs, we found that the new ICs formed homogeneously are definitely more numerous (of about two orders of magnitude) than the new ICs formed heterogeneously. Nevertheless, the last ones contribute for about 30% to the total new ICs in the cirrus regime, globally.

To the best of our knowledge, the simultaneous contributions of four aerosol types (dust, black carbon, soluble organics, and bioaerosols) to immersion/condensation and deposition nucleation have been investigated for the first time in this thesis (Chapter 6). Globally, the mean concentration of the new heterogeneously-formed ICs in the Northern Hemisphere (NH) is twice the mean in the Southern Hemisphere (SH). Most of the new ICs derive from glassy OC in the cirrus regime and from BC in the mixed-phase regime. DU contribution is larger in the NH than in the SH, but it is not the principal source for heterogeneous ice nucleation. The global contribution of BIO amounts to $\sim 20\%$ in the lower troposphere.

Finally, for the first time all the tendencies associated to the cold cloud (micro)physical processes and related to ICNCs have been considered (Chapter 7). The ice nucleation mechanisms have been compared with the other processes which lead to the production or removal of ICs. The following sources of ICs have been identified in the CLOUD submodel: convective detrainment – DETR, ice nucleation in the cirrus regime – NCIR, ice nucleation in the mixed-phase regime – NMIX, instantaneous freezing – FREE, secondary ice production – SECP, and sedimentation – SEDI, while the sinks of ICs are: melting – MELT, aggregation – AGGR, accretion – ACCR, self-collection – SELF, and SEDI.

We found that the main sources of ICs in the cirrus regime are NCIR, DETR, and FREE. NCIR is the only source of ICs in the upper troposphere, while both NCIR and DETR are sources in the cirrus regime at pressures higher than 350 hPa. Although limited to temper-

atures just below −35°C and beyond the tropics, FREE plays an important role in EMAC. SEDI is the major source of ICs in the mixed-phase regime, while it is the main removal mechanism of ICs in the cirrus regime. NMIX as well as SECP are the weakest sources of ICs. This implies that the effects due to changes in the parameterizations of heterogeneous nucleation and secondary ice production can be strongly smoothed by the action of other (micro)physical processes. Therefore, performing the analysis of the partial ICNC tendencies is useful in order to identify the main processes responsible for production and removal of ICs.

Outlook

From the results obtained in this thesis, a number of open questions still remains. This thesis can be seen as a starting point for further developments and analyses, like the ones listed below.

- As mentioned in Subsection 4.3.2, the modelled ICNCs should be compared with lidar-radar satellite retrievals, which offer a global coverage. By a first qualitative comparison, the results presented in this thesis agree with the ICNCs recently retrieved from the DARDAR database and published in Sourdeval et al. (2018) and Gryspeerdt et al. (2018b).

- The climate effects due to long timescale changes in cloud radiative effects and aerosol–cloud interactions under perturbations of anthropogenic emissions should be studied with the state-of-the-art model configuration.

- It is known that the representation of the vertical velocity in GCMs constitutes a large uncertainty in the calculation of ice nucleation rates (Guo et al., 2008; Barahona et al., 2017). In the CLOUD submodel, the subgrid vertical velocity (i.e. w_{sub}) is parameterized via a turbulent kinetic energy scheme which was actually defined for the atmospheric boundary layer (Brinkop and Roeckner, 1995). Given the fundamental role of vertical motions to determine the maximum relative humidity and drive ice nucleation, an improvement of the subgrid-scale vertical velocity representation would be desirable. It has been shown that improvements on this front can be achieved by defining w_{sub} via a subgrid distribution of vertical velocity determined by the grid-mean vertical velocity and its standard deviation (Barahona et al., 2017).

- The analysis of the cold cloud (micro)physical tendencies in Chapter 7 has shown that ICNCs can undergo important changes due to physical constraints which are not associated to the known (micro)physical processes but impose some minimal and maximal ICNC values. This is an aspect which is worth to be further investigated.

- The representation of bioaerosols, which have been simulated as passive tracers, can be improved so that they can interact with other aerosols (e.g. dust) via the aerosol model GMXe. Such a development would let a better estimation of the transport of bioaerosols,

which can be transported for long (intercontinental) distances when associated to dust particles (Kellogg and Griffin, 2006). An accurate description of bioaerosol dispersal would be also useful for studies of health effects due to allergens and pathogens.

Appendix A

Supplementary material

A.1 Acronyms and symbols

Acronyms	Meaning
AIDA	Aerosol Interaction and Dynamics in the Atmosphere (cloud chamber)
BC	Black Carbon
BIO	Bioaeorosols
BN08	Parameterization of Barahona and Nenes (2008)
BN09	Parameterization of Barahona and Nenes (2009b)
BNhom	Homogeneous nucleation parameterized in Barahona and Nenes (2009b)
CCMI	Chemistry–Cimate Model Initiative
CCN	Cloud Condensation Nuclei
CDNC	Cloud Droplet Number Concentration
$CDNC_{burden}$	vertically integrated CDNC
CFDC	Continuous Flow Diffusion Chamber
CNT	Classical Nucleation Theory
DU	Mineral DUst
ESM	Earth System Model
FSSP	Forward Scattering Spectrometer Probe
GCM	General Circulation Mmodel
IC	Ice Crystal
ICNC	Ice Crystal Number Concentration
$ICNC_{burden}$	vertically integrated ICNC
$ICNC_{pre}$	pre-existing ice crystal number concentration
IS	Impaction Scavenging
INP	Ice Nucleating Particle
ITCZ	Inter Tropical Convergence Zone
IWC, IWP	Ice Water Content, Ice Water Path
JULIA	JUeLich In-situ Airborne database
KL02	Parameterization of Kärcher and Lohmann (2002b)
LCRE	Longwave Cloud Radiative Effect
LD06	Parameterization of Lohmann and Diehl (2006)

LWC, LWP	Liquid Water Content, Liquid Water Path
NCRE	Net Cloud Radiative Effect
NH	Northern Hemisphere
NS	Nucleation Scavenging
OC	Organic Compound
P_{tot}	Total Precipitation
P13	Parameterization of Phillips et al. (2013)
PDA08	Parameterization of Phillips et al. (2008)
PBAP	Primary Biological Aerosol Particle
PREICE	PRe-Existing Ice Crystal Effect
SCRE	Shortwave Cloud Radiative Effect
SH	Southern Hemisphere
SIC	Sea-Ice Concentration
SST	Sea Surface Temperature
T	Triangular truncation
TCC	Total Cloud Cover
TKE	Turbulent Kinetic Energy
TOA	Top Of the Atmosphere
TTL	Tropical Tropopause Layer
TWP	Tropical Warm Pool
UAF	Unified Activation Framework (Karydis et al. (2011))
UTLS	Upper Troposphere and Lower Stratosphere

Symbols	Meaning
D_c	diameter of activated liquid cloud droplets
D_M	diameter aerosol mode
D_X	diameter of aerosol group X
$f(w)$	output variable of BN09 which depends on vertical velocity
$f_c,\ f_{c,hom}$	fractions of frozen droplets at s_{hom} with and without the presence of INPs
e	ambient water vapour pressure
$e_{s,w}$	saturation vapour pressure over (liquid) water
$e_{s,i}$	saturation vapour pressure over ice
g_{glass}	fraction of soluble organic aerosols which become glassy (= 0.5)
G	Gibbs free energy
ΔG	Gibbs free energy change associated to homogeneous nucleation
ΔG^{act}	energy activation barrier
ΔG^*	energy barrier to form a critical ice embryo in liquid (pure) water
ΔG^*_{het}	energy barrier to form an critical ice embryo on an INP surface
ΔG_{surf}	interfacial Gibbs free energy
ΔG_{vol}	volume Gibbs free energy
H	term which describes the scarcity of heterogeneous nucleation in P13
$J_{hom},\ J_{het}$	homogeneous and heterogeneous nucleation rates
k	Boltzmann constant
m	mass
M	aerosol mode
$n_{INP,*}$	reference activity spectrum
$n_{INP,X}$	conc. of active INPs in the group X
N_c	conc. of activated liquid cloud droplets
N_X	conc. of aerosol group X
$N_{i,het}$	conc. of the new ICs formed via heterogeneous nucleation (via BN09)
$N^*_{i,het}$	$N_{i,het}$ per integration time
$N_{i,hom}$	conc. of the new ICs formed via homogeneous nucleation (via BN09)
$N^*_{i,hom}$	$N_{i,hom}$ per integration time
$\mathrm{N}^{\mathrm{NEW}}_{\mathrm{i,cirrus}}$	conc. of the new ICs formed in the cirrus regime
$\mathrm{N}^{\mathrm{NEW}}_{\mathrm{i,cnt}}$	conc. of the new ICs formed via contact nucleation (via LD06)
$\mathrm{N}^{\mathrm{NEW}}_{\mathrm{i,hom}}$	conc. of the new ICs formed via homogeneous nucleation (via KL02)
$\mathrm{N}^{\mathrm{NEW}}_{\mathrm{i,imm}}$	conc. of the new ICs formed via immersion nucleation (via LD06 or P13)
$\mathrm{N}^{\mathrm{NEW}}_{\mathrm{i,mix}}$	conc. of the new ICs formed in the mixed-phase regime
N_{lim}	conc. of INPs needed to inhibit homogeneous nucleation
P	pressure
$P(w)$	Gaussian probability density function
q_v, q_w, q_i	mixing ratios of water vapour, cloud liquid water, and cloud ice
r	radius
r^*	critical radius of the ice embryo
r_d	cloud droplet radius
r_{insol}	equivalent radius of the insoluble fraction in INP
s_i	ice supersaturation ($= S_i - 1$)

s_{max}	maximum ice supersaturation
s_{hom}	ice supersaturation threshold for homogeneous nucleation
S_i	ice saturation ratio ($= e_v/e_{s,i}$)
S_w	water saturation ratio ($= e_v/e_{s,w}$)
t	time
T	temperature
T_{th}	temperature threshold for the onset of homogeneous nucleation
V_d	cloud droplet volume
w	updraught velocity associated to the whole grid cell
$\overline{w}$	grid-mean vertical velocity resolved by the model
w_{sub}	subgrid-scale variability of w
$w_{sub,pre}$	w_{sub} which includes the PREICE
α_X	fractional contribution of X to INP numbers in the background scenario
μ_X	mean number of activated ice embryos per insoluble aerosol particle with D_X
Ω_X	total surface area of aerosols with $1 > D_X > 0.1$ μm
$\Omega_{X,*}$	total surface area of aerosols with $D_X > 0.1$ μm in the background scenario
σ_M	standard deviation of aerosol mode M
σ_c	standard deviation of activated liquid cloud droplets
$\sigma_{i,w}$, $\sigma_{i,v}$	surface tension of ice in liquid water or water vapour
$\sigma_{INP,i}$, $\sigma_{INP,w}$, $\sigma_{INP,w}$	surface tensions of INP in ice or liquid water or water vapour
θ	contact angle

A.2 Supplementary figures for Chapter 4

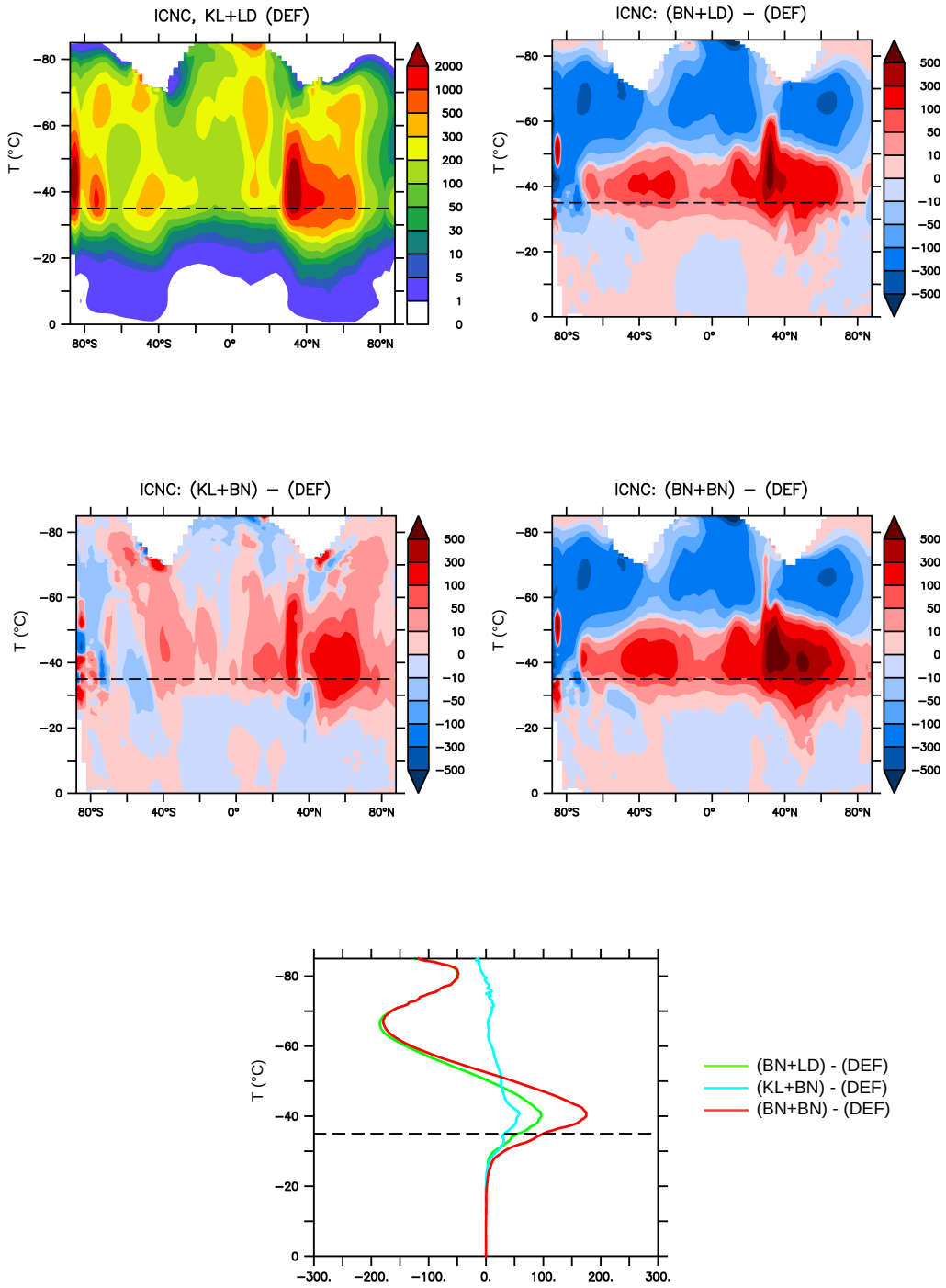

Figure A.1: Annual zonal means of (grid-averaged) ICNCs (L^{-1}) for the default simulation KL+LD and the absolute changes of BN+LD, KL+BN, and BN+BN with respect to it as functions of latitude and temperature. (*Last row*) Absolute changes of annual zonal means averaged along the latitude.

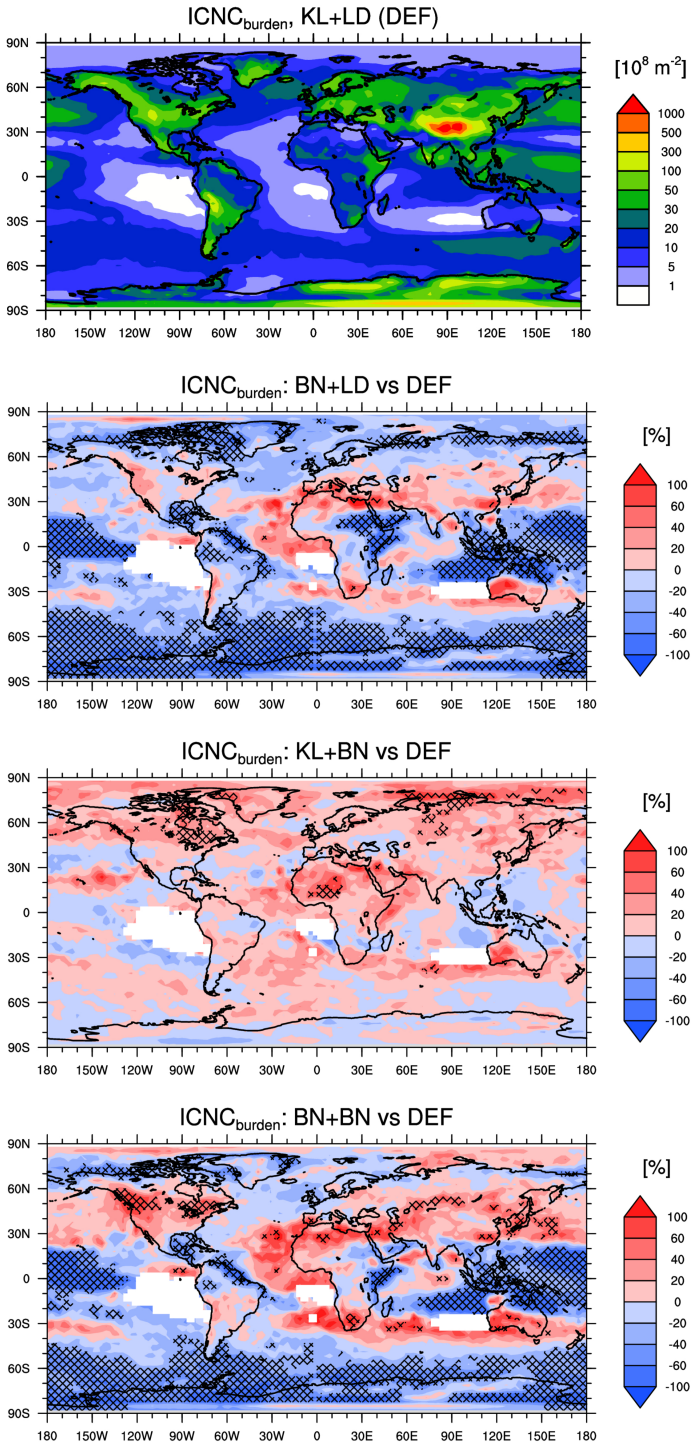

Figure A.2: Annual means of vertically integrated ice crystal number concentration for the default simulation KL+LD and the relative percentage changes of BN+LD, KL+BN, and BN+BN with respect to it (i.e. $(test - \mathrm{DEF})/\mathrm{DEF} \cdot 100$), computed where $\mathrm{ICNC}_{\mathrm{burden}}^{\mathrm{DEF}} \geq 10^8$ m^{-2}. The crossed pattern indicates areas with a significance level of 95%.

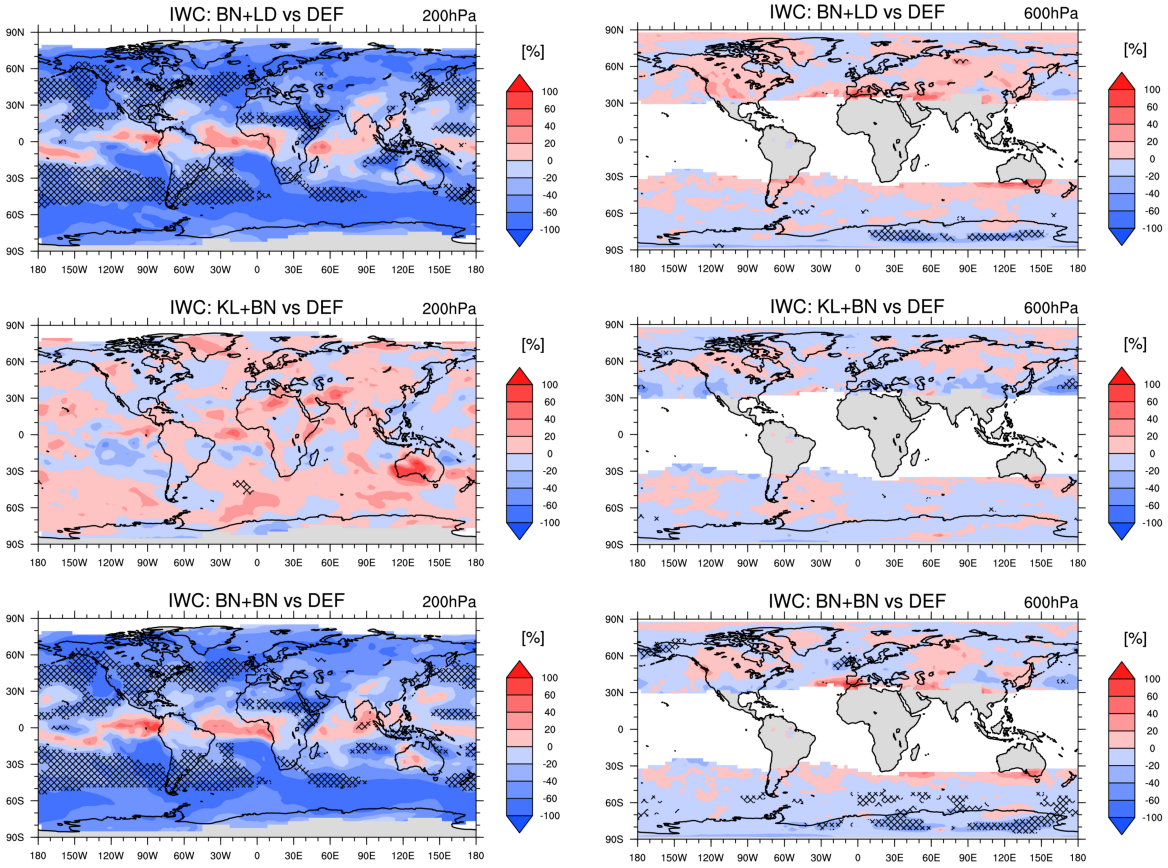

Figure A.3: Relative percentage changes of annual means of (grid-averaged) IWC at 200 hPa and 600 hPa of BN+LD, KL+BN, and BN+BN with respect to the default simulation (i.e. $(test - \mathrm{DEF})/\mathrm{DEF} \cdot 100$), computed where $\mathrm{IWC}^{\mathrm{DEF}} \geq 0.1$ mg kg^{-1}. The crossed pattern indicates areas with a significance level of 95%.

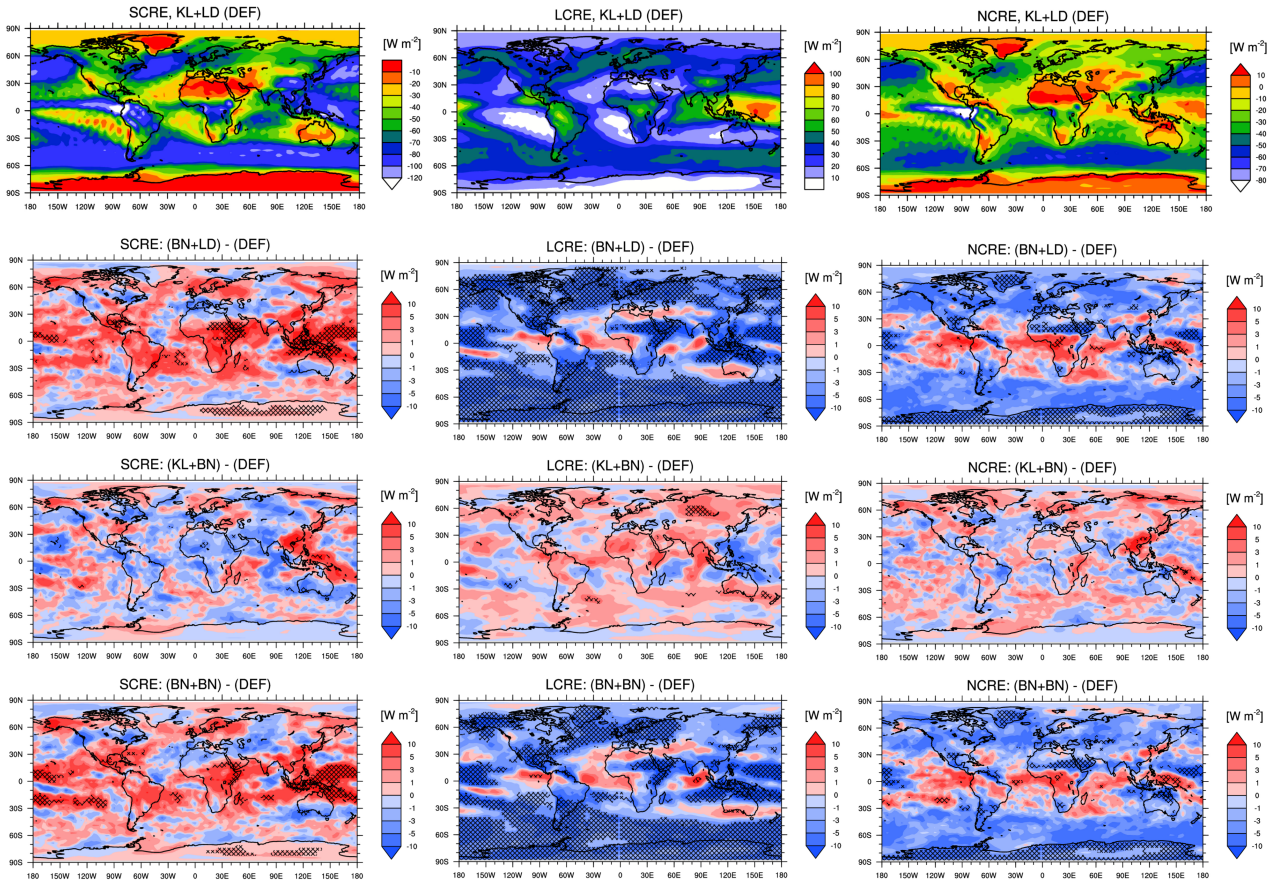

Figure A.4: Annual means of shortwave, longwave, net cloud radiative effects (SCRE, LCRE, NCRE) for the default simulation KL+LD and the absolute changes of BN+LD, KL+BN, and BN+BN with respect to it. The crossed pattern indicates areas with a significance level of 95%.

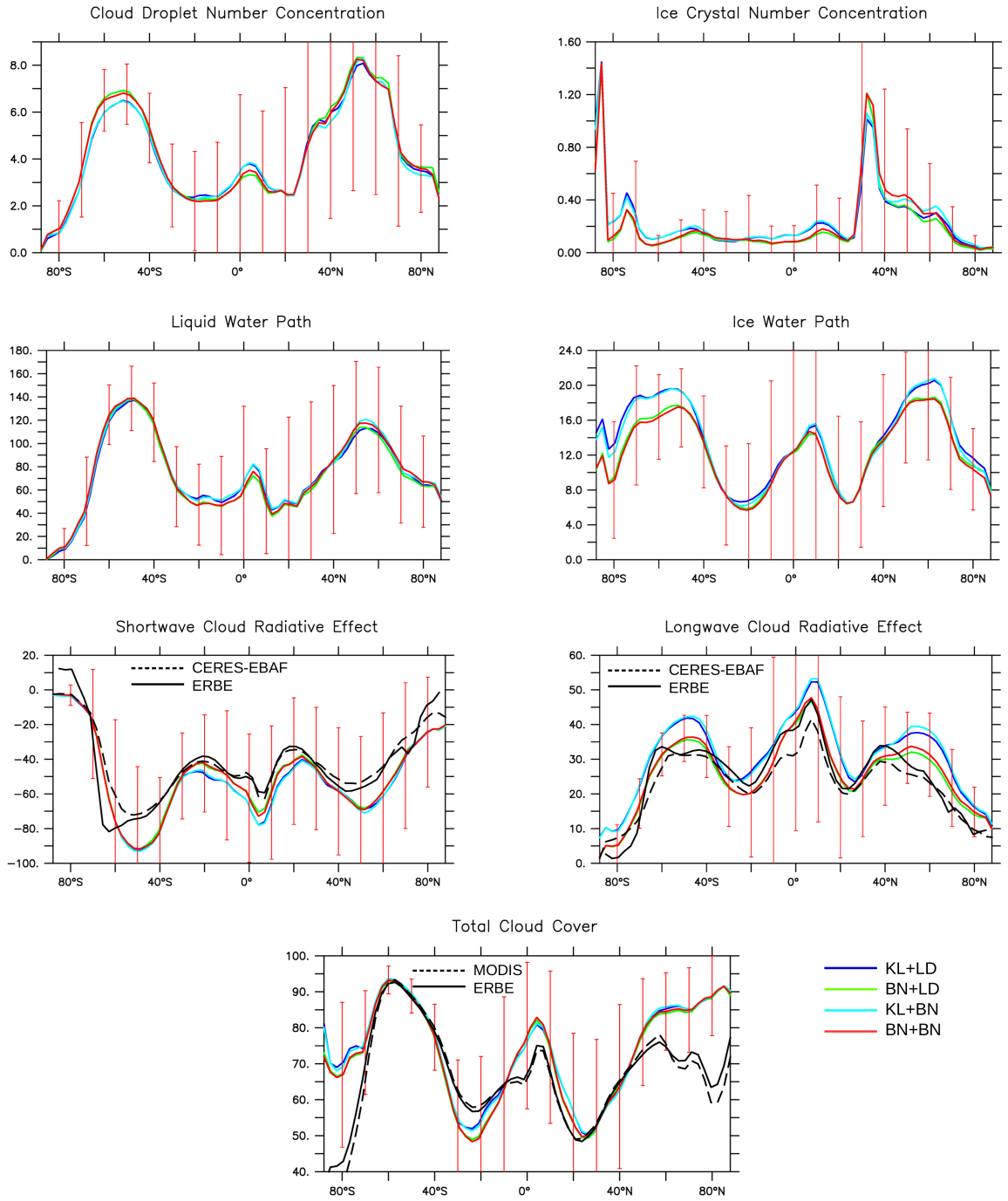

Figure A.5: Annual zonal means of $CDNC_{burden}$ (10^{10} m^{-2}), $ICNC_{burden}$ (10^{10} m^{-2}), non-precipitable LWP (g m^{-2}), and IWP (g m^{-2}) averaged over the whole grid-boxes, SCRE (W m^{-2}), LCRE (W m^{-2}), and TTC (%). Black lines refer to satellite observations, from ERBE 1985-1990, CERES-EBAF-L3B-Ed2.8 2000-2016, MODIS-TERRA-v6 2004-2008. Error bars are ± one standard deviation.

A.3 Supplementary figures for Chapter 5

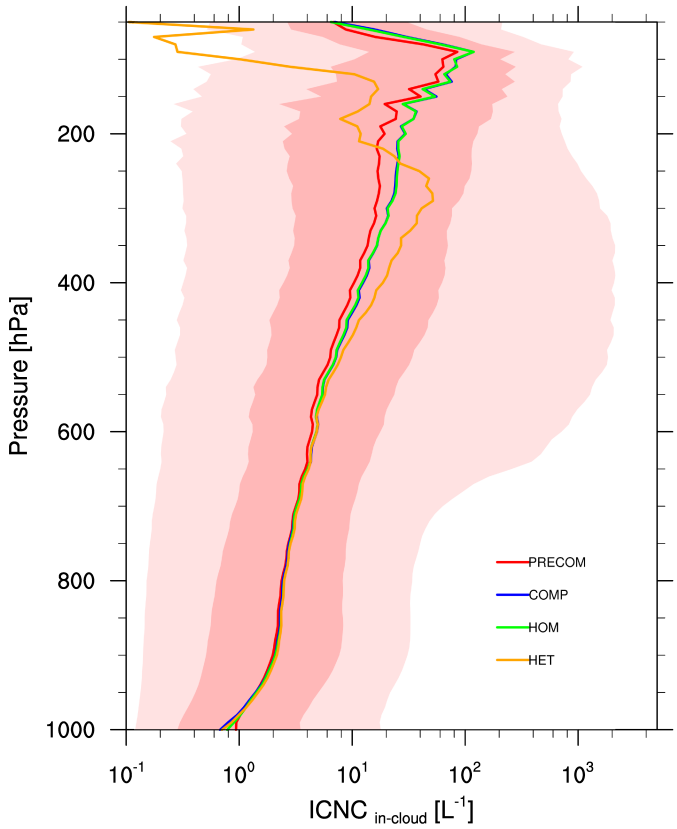

Figure A.6: In-cloud ice crystal number concentrations versus pressure. Medians for model results are computed using 5-hour means between 90°S and 90°N, masking $\mathrm{ICNC}_{\mathrm{in-cloud}} < 0.1\ \mathrm{L}^{-1}$, for each pressure bin of 10 hPa. Darker red colour indicates the 25th and 75th percentiles of PRECOM, while lighter red colour indicates the 5th and 95th percentiles of PRECOM.

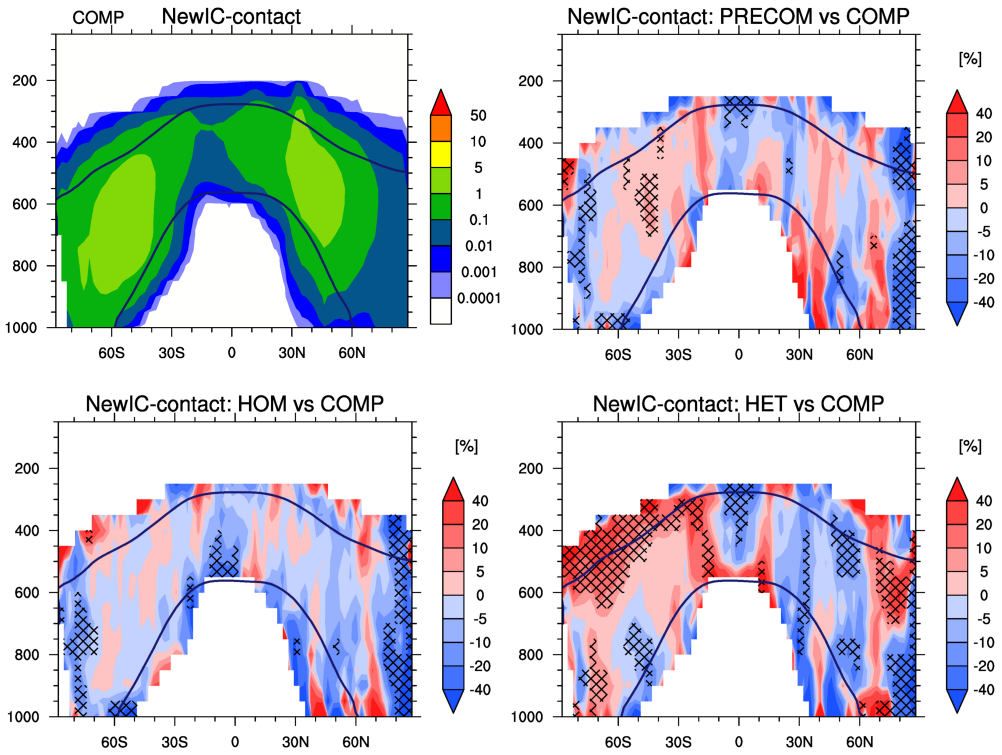

Figure A.7: Annual zonal means of the new ICs (in L^{-1} per integration time) produced via contact nucleation (through LD06) in COMP and the relative percentage changes of PRECOM, HOM, and HET with respect to it (i.e. $(test - \mathrm{COMP})/\mathrm{COMP} \cdot 100$), computed where $N_{i,cnt}^{NEW,COMP} \geq 0.0001\ L^{-1}$ per integration time. The isotherms at 0°C and −35°C are annual means; the crossed pattern indicates areas with a significance level of 95%.

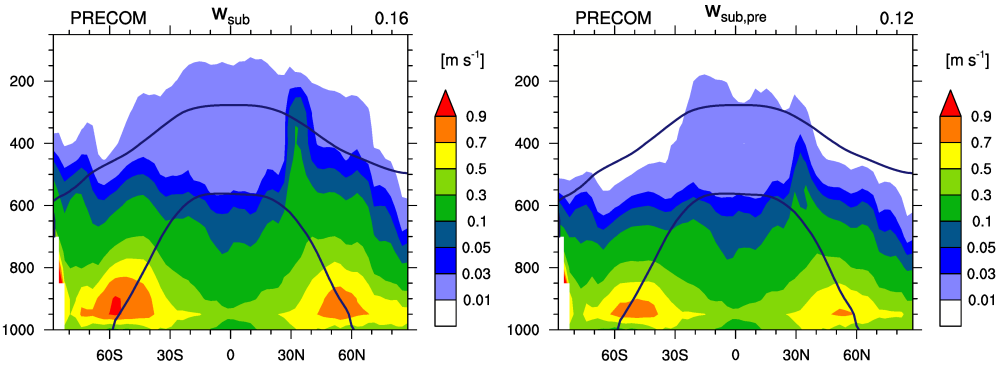

Figure A.8: Annual zonal means of (*left*) the subgrid-scale vertical velocity (i.e. w_{sub}) and (*right*) the w_{sub} which includes the PREICE (i.e. $w_{sub,pre}$) for the PRECOM simulation. The numbers on the top right of the plots are global means (in m s^{-1}); the isotherms at 0°C and −35°C are annual means. The values are comparable with the results of Barahona et al. (2017). It can be easily noted that when the PREICE is taken into account there is a general reduction of w_{sub}.

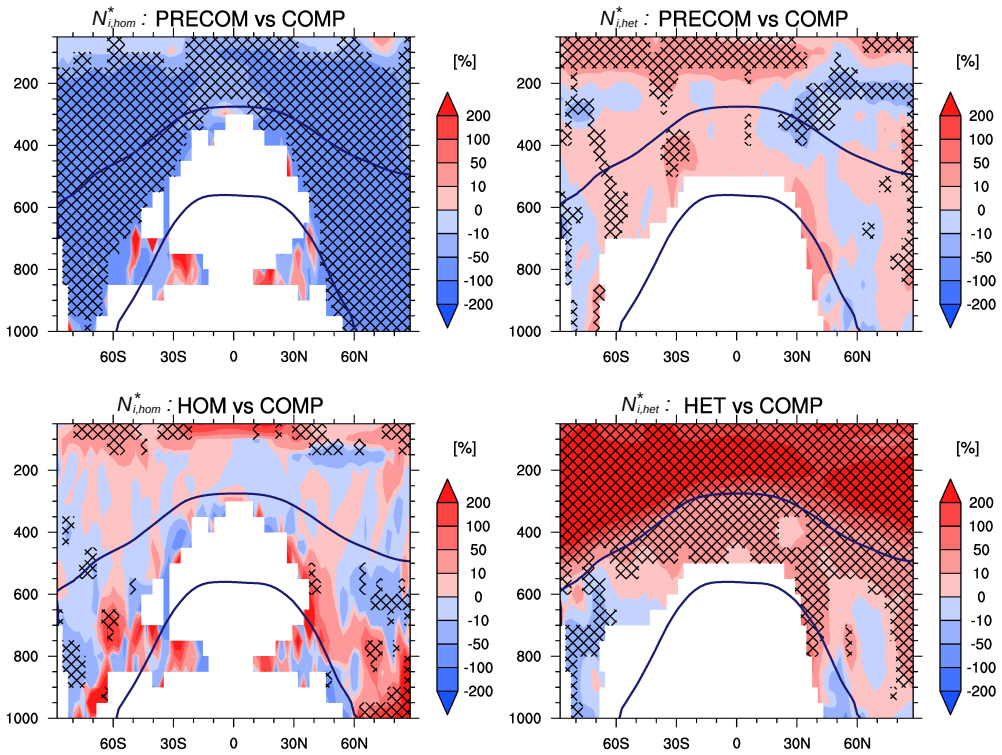

Figure A.9: Relative percentage changes of the annual zonal means of the simulations PRECOM, HOM, and HET with respect to COMP (i.e. $(test - \text{COMP})/\text{COMP} \cdot 100$) for $N^*_{i,hom}$ and $N^*_{i,het}$, computed where $N^*_{i,hom}$ and $N^*_{i,het}$ are ≥ 0.0001 L^{-1} per integration time. The isotherms at 0°C and −35°C are annual means; the crossed pattern indicates areas with a significance level of 95%.

A.4 Supplementary figures for Chapter 6

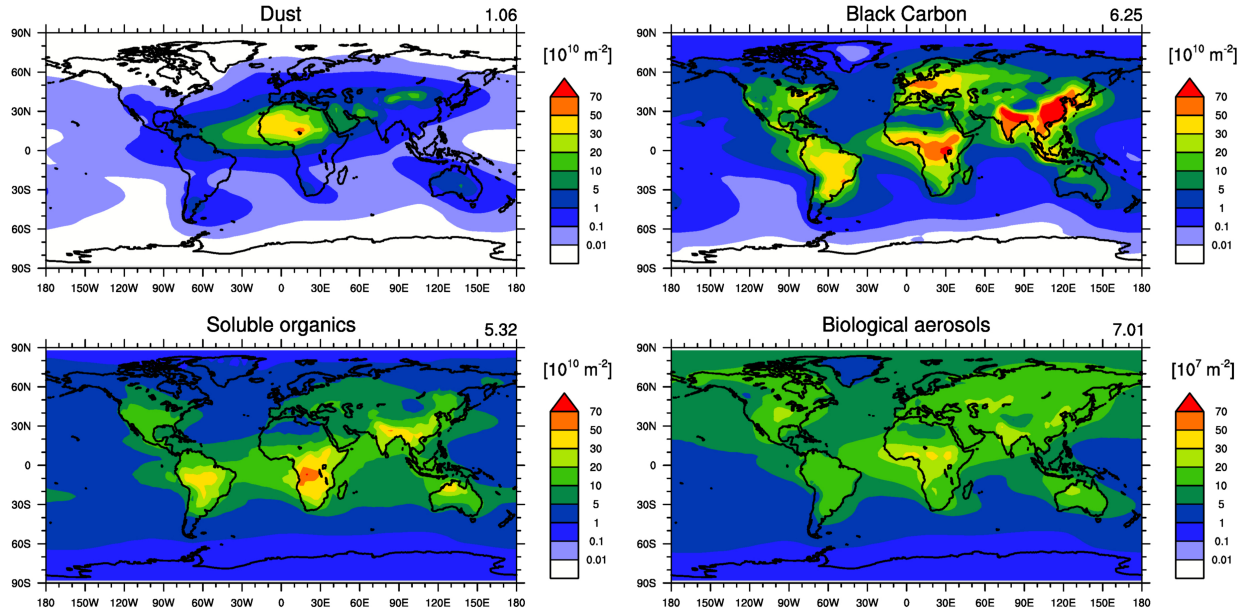

Figure A.10: Annual means of vertically integrated number concentrations of dust, black carbon, soluble organics, and bioaerosols. The numbers on the top right of the plots are global means (in 10^{10} m^{-2} and 10^{7} m^{-2} for bioaerosols).

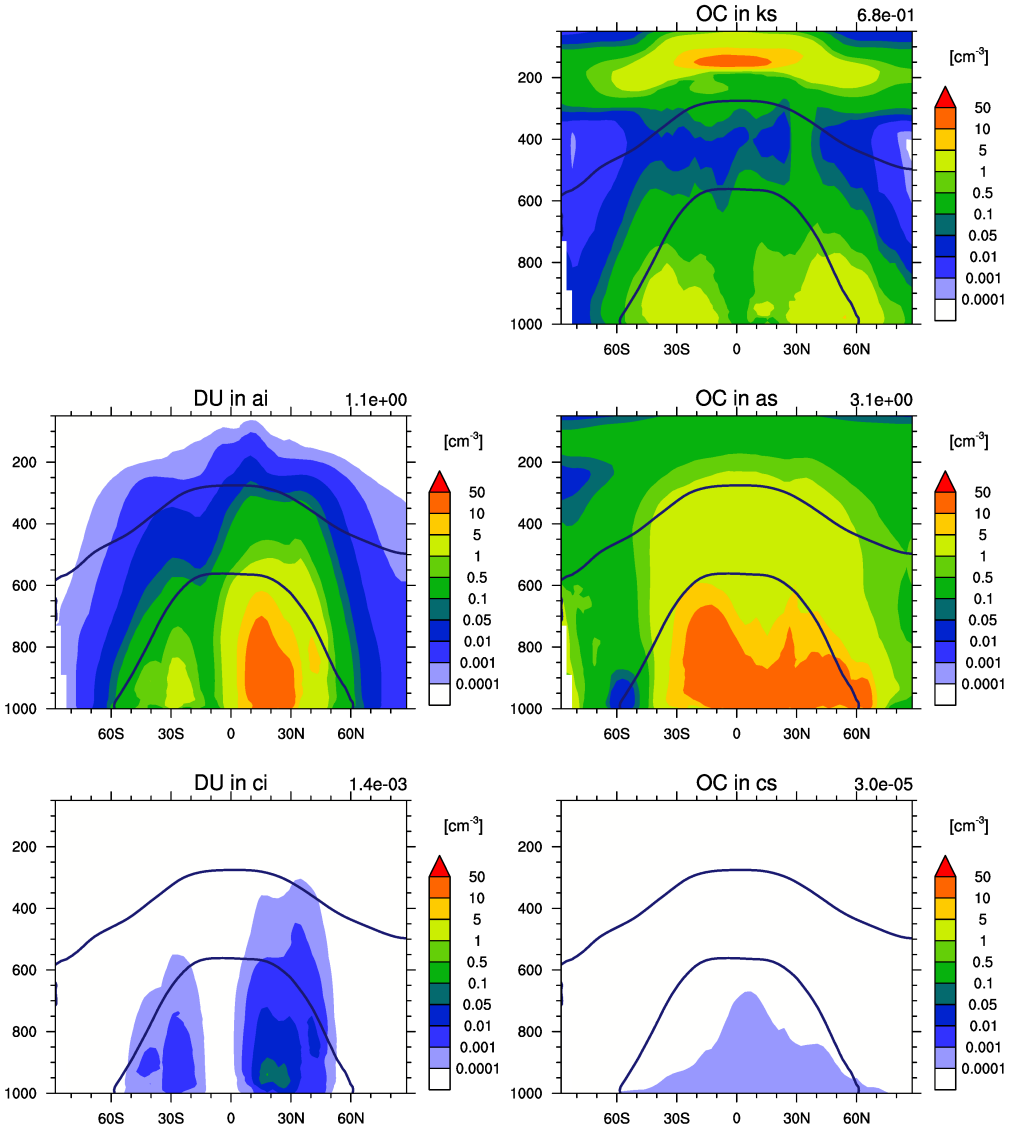

Figure A.11: Annual zonal means of number concentrations of dust (*left*) in accumulation and coarse insoluble modes, and soluble organics (*right*) in Aitken, accumulation, and coarse soluble modes. The numbers on the top right of the plots are global means (in cm^{-3}); the isotherms at 0°C and −35°C are annual means.

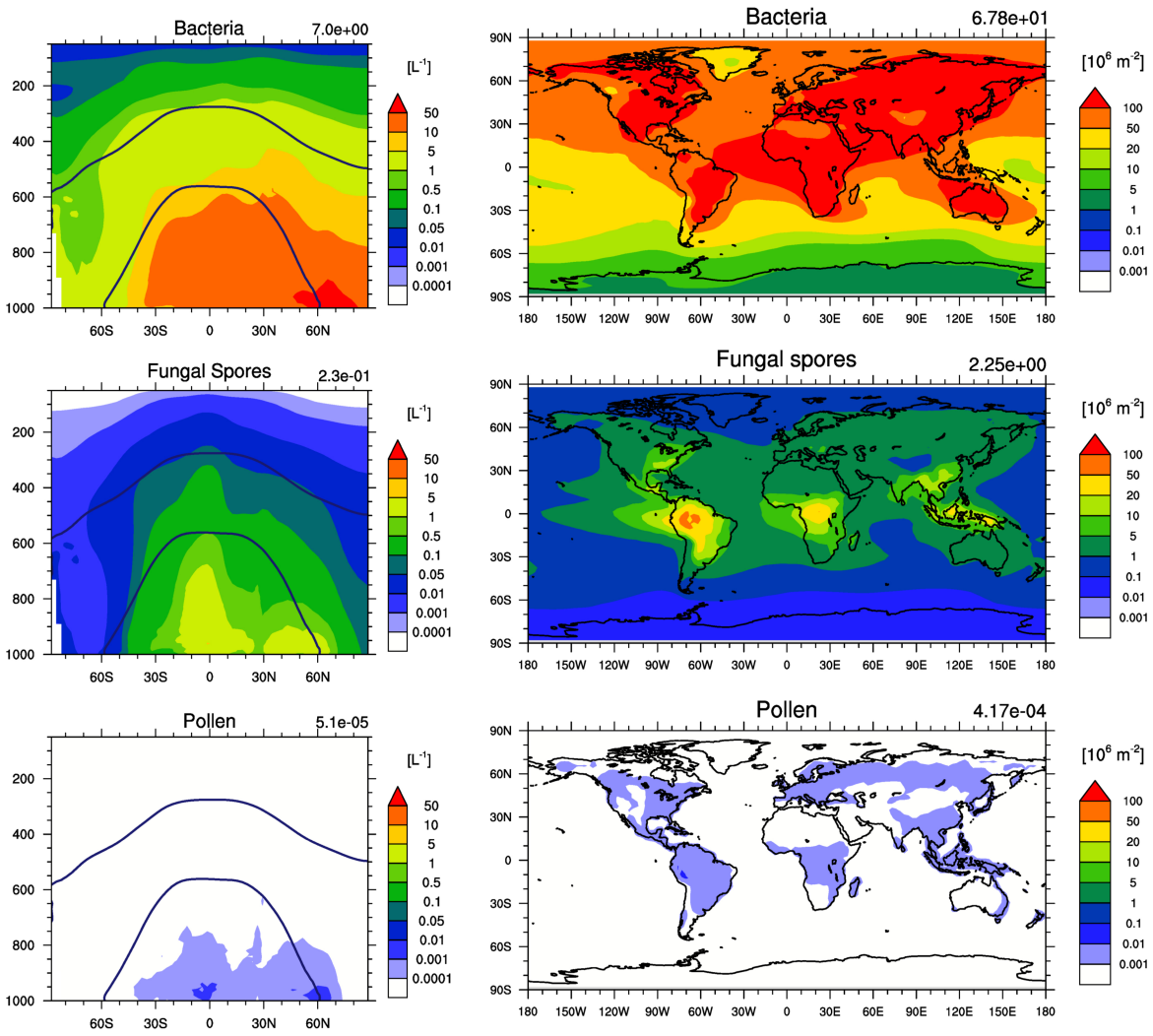

Figure A.12: (*Left*) Annual zonal means of number concentrations of bacteria, fungal spores, and pollen. The numbers on the top right of the plots are global means (in L^{-1}); the isotherms at 0°C and −35°C are annual means. (*Right*) Vertically integrated number concentrations of bacteria, fungal spores, and pollen. The numbers on the top right of the plots are global means (in 10^6 m^{-2}).

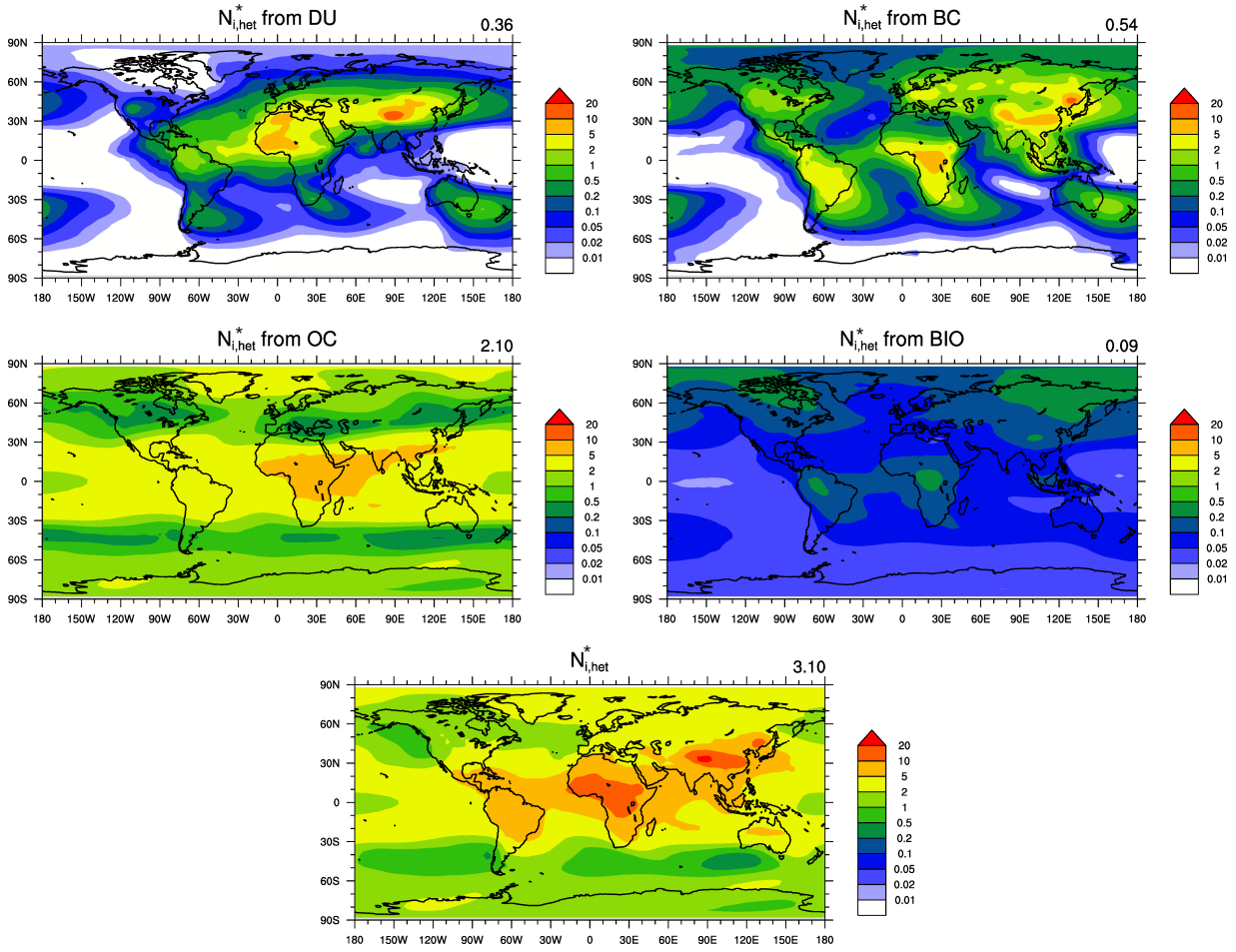

Figure A.13: Global distributions of the vertically integrated $N^*_{i,het}$ (in 10^5 m^{-2} per integration time) derived from dust, black carbon, soluble organics, and bioaerosols and the vertically integrated total $N^*_{i,het}$. The numbers on the top right of the plots are global means (in 10^5 m^{-2} per integration time).

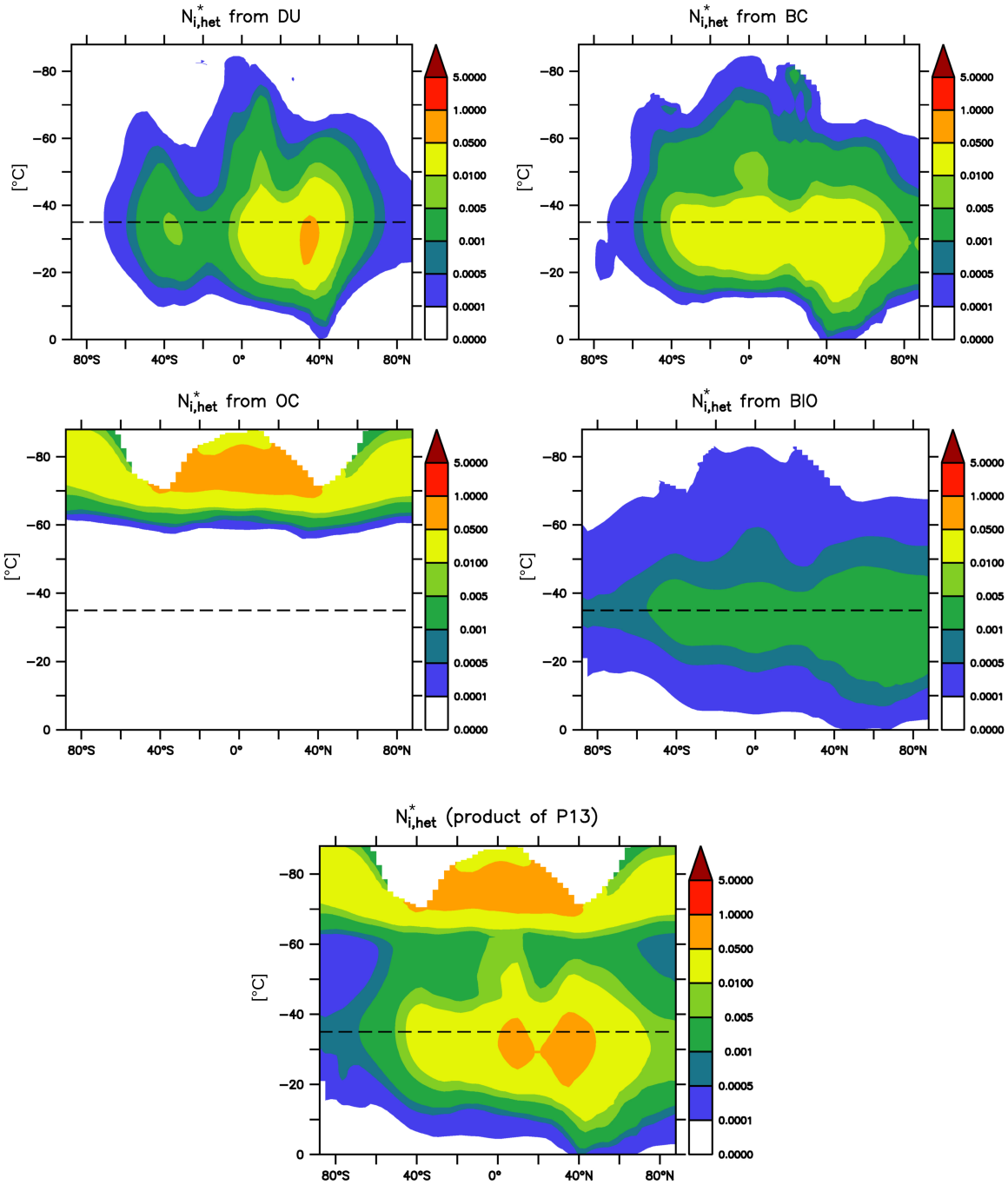

Figure A.14: Annual zonal means of $N^*_{i,het}$ (in L^{-1} per integration time) derived from dust, black carbon, organics, and bioaerosols and the total $N^*_{i,het}$ as functions of latitude and temperature.

A.5 Supplementary information and figures for Chapter 7

Individual "adjustments"

The partial ICNC tendencies due to the "adjustments" are listed below, together with the description of their origin. The brackets contain the sign of the tendency followed by the global mean of the annual zonal medians (in m^{-3} s^{-1}), which can be compared with the global means of Figures 7.1 and 7.2.

- **Minmax0 (> 0; 10^{-16})**
  The minimal value (10^{-12} m^{-3}) allowed for ICNC is imposed.
- **Minmax1 (< 0; 10^{0}) and Minmax2 (> 0; 10^{-3}).**
  The maximal (Minmax1) and minimal (Minmax2) values for ICNC are defined as 10^{7} m^{-3} and 10 m^{-3}, respectively.
- **Minmax3 (< 0; 10^{-3}).**
  If cloud cover > 0, $q_i > 10^{-12}$ kg kg^{-1}, and ICNC$\leq$ 10 m^{-3}, thus, ICNCs must be equal to concentrations of the new ICs produced in the cirrus regime.
- **Minmax4 (> 0; 10^{-3}).**
  The minimum 10 m^{-3} is again imposed.
- **Minmax5 (< 0; 10^{-1}).**
  If the condition cloud cover > 0 and $q_i > 10^{-12}$ kg kg^{-1} is not satisfied, then ICNC must be equal to the minimum 10^{-12} m^{-3}, otherwise it remains unchanged.
- **Minmax6 ($= 0$).**
  ICNC must be at least equal to 10^{-12} m^{-3}. It never happens that ICNC $< 10^{-12}$ m^{-3}, hence, this tendency is null.
- **Minmax7 ($= 0$).**
  ΔICNC can be at maximum equal to the ICNC just before the removal processes (SELF, AGGR, and ACCR) take place. It never happens that ΔICNC $>$ ICNC, thus, the tendency is null.
- **Minmax8 (> 0; 10^{-23}).**
  The minimum possible for ICNC (10^{-12} m^{-3}) is again guaranteed.
- **Minmax9 (> 0; 10^{-3}).**
  The minimum 10 m^{-3} is again imposed.

We observe that some of the tendencies are globally comparable with the sources and sinks of ICs in Figures 7.1 and 7.2. Minmax1 is the strongest (negative) tendency, of the same order of magnitude of AGGR, ACCR, and SEDI. Interestingly, the zonal meadians of Minmax1 show a pattern similar to FREE (not shown). Minmax5 is also a negative tendency, of the same order of magnitude of DETR and NCIR. Minmax2, Minmax3, Minmax4, Minmax9 are of the order of 10^{-3}, greater only than MELT. The zonal medians of Minmax3 and Minmax4 (not shown) reveal that one tendency is the opposite of the other one, so their sum is almost zero (10^{-6} m^{-3} s^{-1}) and their contribution is basically zero.

Figures

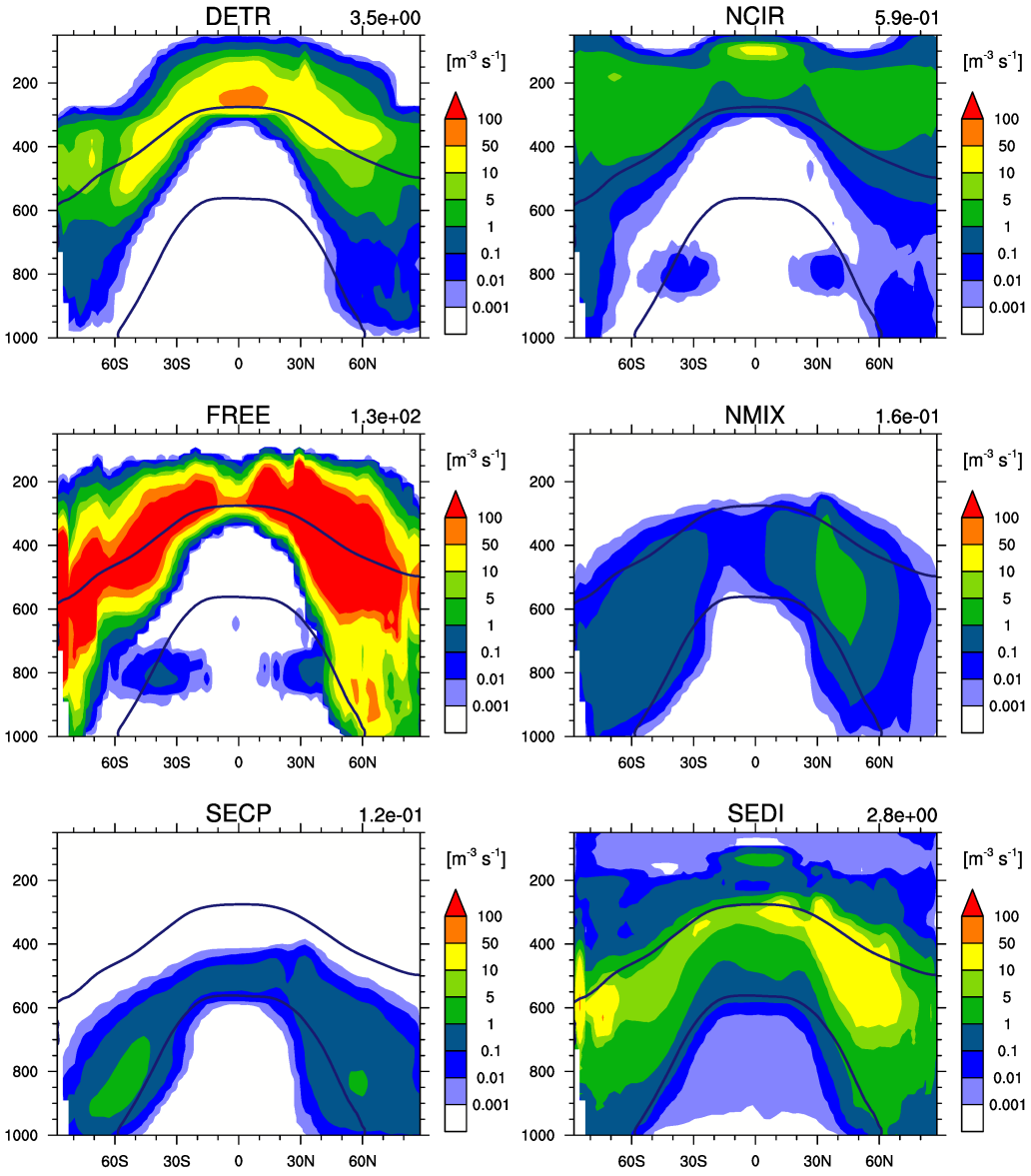

Figure A.15: Annual zonal means of the partial ICNC tendencies associated to cold cloud microphysical sources. The numbers on the top right of the plots are global means (in m^{-3} s^{-1}); the isotherms at 0°C and −35°C are annual means; the titles are described in Table 7.1. Note that SEDI takes into account only positive values.

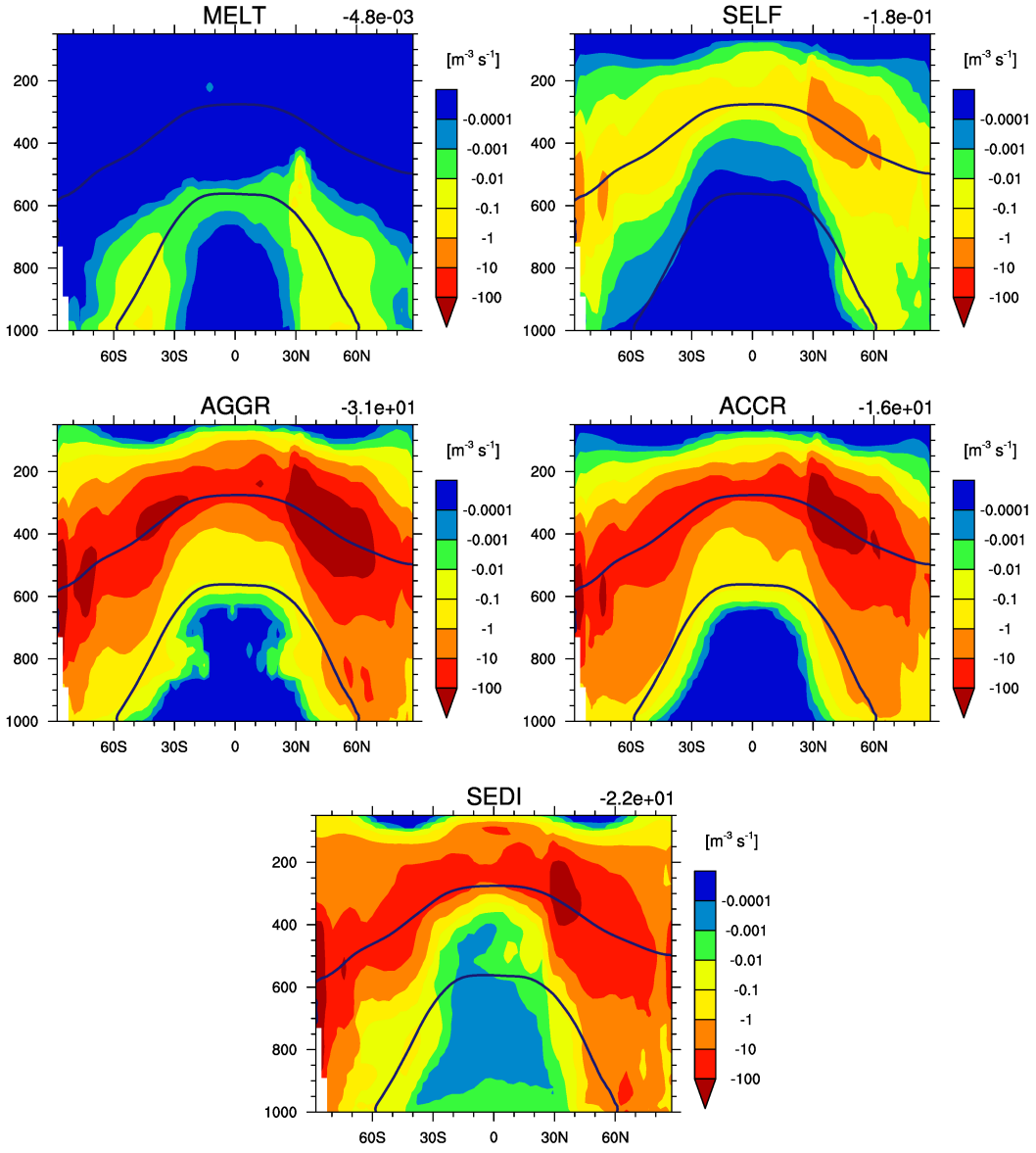

Figure A.16: Like Figure A.15 but for cold cloud microphysical sinks. Note that SEDI takes into account only negative values.

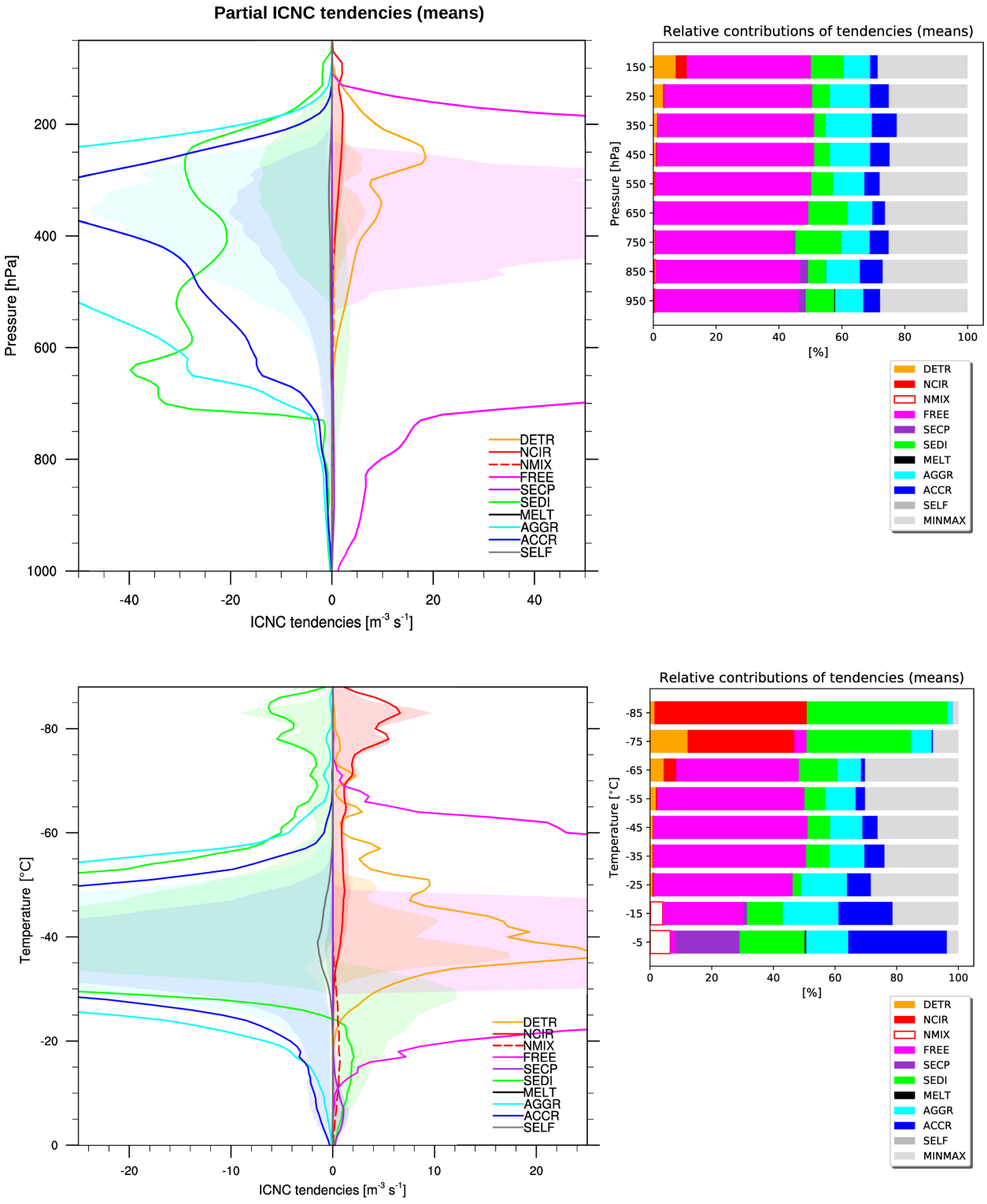

Figure A.17: Partial ICNC tendencies as functions of pressure (*top*) and as functions of temperature (*bottom*). The vertical profiles (*left*) are annual global means and the coloured shadows mark the areas between the 25th and 75th percentiles. The profiles on the left hand side of the plot are sinks of ICs, while the ones on the right hand side are sources of ICs. The bar charts (*right*) represent the percentage contributions of the partial ICNC tendencies to the individual tendency of ICNC (including MINMAX) based on global means computed in bins of 100 hPa (*top*) and in bins of 10°C (*bottom*).

Bibliography

Abbatt, J. P. D., Benz, S., Cziczo, D. J., Kanji, Z., Lohmann, U., and Möhler, O.: *Solid Ammonium Sulfate Aerosols as Ice Nuclei: A Pathway for Cirrus Cloud Formation*, Science, 313, 1770–1773, 2006.

Abdul-Razzak, H. and Ghan, S. J.: *A parameterization of aerosol activation: 2. Multiple aerosol types*, Journal of Geophysical Research: Atmospheres, 105, 6837–6844, 2000.

Ackermann, I. J., Hass, H., Memmesheimer, M., Ebel, A., Binkowski, F. S., and Shankar, U.: *Modal aerosol dynamics model for Europe: development and first applications*, Atmospheric Environment, 32, 2981–2999, 1998.

Aquila, V., Hendricks, J., Lauer, A., Riemer, N., Vogel, H., Baumgardner, D., Minikin, A., Petzold, A., Schwarz, J. P., Spackman, J. R., Weinzierl, B., Righi, M., and Dall'Amico, M.: *MADE-in: a new aerosol microphysics submodel for global simulation of insoluble particles and their mixing state*, Geoscientific Model Development, 4, 325–355, 2011.

Asselin, R.: *Frequency filter for time integrations*, Monthly Weather Review, 100, 487?–490, 1972.

Bacer, S., Sullivan, S. C., Karydis, V. A., Barahona, D., Krämer, M., Nenes, A., Tost, H., Tsimpidi, A. P., Lelieveld, J., and Pozzer, A.: *Implementation of a comprehensive ice crystal formation parameterization for cirrus and mixed-phase clouds in the EMAC model (based on MESSy 2.53)*, Geoscientific Model Development, 11, 4021–4041, 2018.

Bacon, N. J., Swanson, B. D., Baker, M. B., and Davis, E. J.: *Breakup of levitated frost particles*, Journal of Geophysical Research: Atmospheres, 103, 13 763–13 775, 1998.

Barahona, D. and Nenes, A.: *Parameterization of cirrus cloud formation in large-scale models: Homogeneous nucleation*, Journal of Geophysical Research: Atmospheres, 113, n/a–n/a, 2008.

Barahona, D. and Nenes, A.: *Parameterizing the competition between homogeneous and heterogeneous freezing in cirrus cloud formation - monodisperse ice nuclei*, Atmospheric Chemistry and Physics, 9, 369–381, 2009a.

Barahona, D. and Nenes, A.: *Parameterizing the competition between homogeneous and heterogeneous freezing in ice cloud formation - polydisperse ice nuclei*, Atmospheric Chemistry and Physics, 9, 5933–5948, 2009b.

Barahona, D., Rodriguez, J., and Nenes, A.: *Sensitivity of the global distribution of cirrus ice crystal concentration to heterogeneous freezing*, Journal of Geophysical Research: Atmospheres, 115, 2010.

Barahona, D., Molod, A., Bacmeister, J., Nenes, A., Gettelman, A., Morrison, H., Phillips, V., and Eichmann, A.: *Development of two-moment cloud microphysics for liquid and ice within the NASA Goddard Earth Observing System Model (GEOS-5)*, Geoscientific Model Development, 7, 1733–1766, 2014.

Barahona, D., Molod, A., and Kalesse, H.: *Direct estimation of the global distribution of vertical velocity within cirrus clouds*, Scientific Reports, 7, 1–11, 2017.

Baumgardner, D., Abel, S. J., Axisa, D., Cotton, R., Crosier, J., Field, P., Gurganus, C., Heymsfield, A., Korolev, A., Krämer, M., Lawson, P., McFarquhar, G., Ulanowski, Z., and Um, J.: *Cloud Ice Properties: In Situ Measurement Challenges*, Meteorological Monographs, 58, 9.1–9.23, 2017.

Bell, N., Hsu, L., Jacob, D. J., Schultz, M. G., Blake, D. R., Butler, J. H., King, D. B., Lobert, J. M., and Maier-Reimer, E.: *Methyl iodide: Atmospheric budget and use as a tracer of marine convection in global models*, Journal of Geophysical Research: Atmospheres, 107, ACH 8–1–ACH 8–12, 2002.

Bennartz, R. and Rausch, J.: *Global and regional estimates of warm cloud droplet number concentration based on 13 years of AQUA–MODIS observations*, Atmospheric Chemistry and Physics, 17, 9815–9836, 2017.

Bouwman, A. F., Lee, D. S., Asman, W. A. H., Dentener, F. J., Van Der Hoek, K. W., and Olivier, J. G. J.: *A global high-resolution emission inventory for ammonia*, Global Biogeochemical Cycles, 11, 561–587, 1997.

Brinkop, S. and Roeckner, E.: *Sensitivity of a general circulation model to parameterizations of cloud–turbulence interactions in the atmospheric boundary layer*, Tellus A, 47, 197–220, 1995.

Brownscombe, J. L. and Thorndike, N. S. C.: *Freezing and Shattering of Water Droplets in Free Fall*, Nature, 220, 687–689, 1968.

Bühl, J., Alexander, S., Crewell, S., Heymsfield, A., Kalesse, H., Khain, A., Maahn, M., Van Tricht, K., and Wendisch, M.: *Remote Sensing*, Meteorological Monographs, 58, 10.1–10.21, 2017.

Burkhardt, U. and Sölch, I.: Cirrus Clouds and Their Representation in Models, Springer–Verlag Berlin Heidelberg, 2012.

Burrows, S. M., Butler, T., Jöckel, P., Tost, H., Kerkweg, A., Pöschl, U., and Lawrence, M. G.: *Bacteria in the global atmosphere – Part 2: Modeling of emissions and transport between different ecosystems*, Atmospheric Chemistry and Physics, 9, 9281–9297, 2009.

Cantrell, W. and Heymsfield, A.: *Production of Ice in Tropospheric Clouds: A Review*, Bulletin of the American Meteorological Society, 86, 795–807, 2005.

Chen, J.-P. and Lamb, D.: *Simulation of Cloud Microphysical and Chemical Processes Using a Multicomponent Framework. Part I: Description of the Microphysical Model*, Journal of the Atmospheric Sciences, 51, 2613–2630, 1994.

Chen, J.-P. and Lamb, D.: *Simulation of Cloud Microphysical and Chemical Processes Using a Multicomponent Framework. Part II: Microphysical Evolution of a Wintertime Orographic Cloud*, Journal of the Atmospheric Sciences, 56, 2293–2312, 1999.

Chen, T., Rossow, W. B., and Zhang, Y.: *Radiative Effects of Cloud-Type Variations*, Journal of Climate, 13, 264–286, 2000.

Clarke, L., Edmonds, J., Jacoby, H., Pitcher, H., Reilly, J., and Richels, R.: *Scenarios of Greenhouse Gas Emissions and Atmospheric Concentrations, Sub-report 2.1A of Synthesis and Assessment Product 2.1 by the US Climate Change Science Program and the Subcommittee on Global Change Research, Department of Energy, Office of Biological & Environmental Research*, Washington, DC, USA, p. 260, 2007.

Courant, R., Friedrichs, K., and Lewy, H.: *Über die partiellen Differenzengleichungen der mathematischen Physik*, Mathematische annalen, 100, 32–74, 1928.

Cziczo, D. J., Froyd, K. D., Hoose, C., Jensen, E. J., Diao, M., Zondlo, M. A., Smith, J. B., Twohy, C. H., and Murphy, D. M.: *Clarifying the Dominant Sources and Mechanisms of Cirrus Cloud Formation*, Science, 340, 1320–1324, 2013.

Cziczo, D. J., Ladino, L., Boose, Y., Kanji, Z. A., Kupiszewski, P., Lance, S., Mertes, S., and Wex, H.: *Measurements of Ice Nucleating Particles and Ice Residuals*, Meteorological Monographs, 58, 8.1–8.13, 2017.

Delanoë, J. and Hogan, R.: *Combined CloudSat-CALIPSO-MODIS retrievals of the properties of ice clouds*, Journal of Geophysical Research: Atmospheres, 115, D00H29, 2010.

DeMott, P. J., Prenni, A. J., Liu, X., Kreidenweis, S. M., Petters, M. D., Twohy, C. H., Richardson, M. S., Eidhammer, T., and Rogers, D. C.: *Predicting global atmospheric ice nuclei distributions and their impacts on climate*, Proceedings of the National Academy of Sciences, 107, 11 217–11 222, 2010.

Dentener, F., Kinne, S., Bond, T., Boucher, O., Cofala, J., Generoso, S., Ginoux, P., Gong, S., Hoelzemann, J. J., Ito, A., Marelli, L., Penner, J. E., Putaud, J.-P., Textor, C., Schulz, M., van der Werf, G. R., and Wilson, J.: *Emissions of primary aerosol and precursor gases in the years 2000 and 1750 prescribed data-sets for AeroCom*, Atmospheric Chemistry and Physics, 6, 4321–4344, 2006.

Després, V. R., Huffman, J. A., Burrows, S. M. Jaenicke, R., S., S. A., Buryak, G., Frˆhlich-Nowoisky, J., Elbert, W., Andreae, M. O., Pöschl, U., and Jaenicke, R.: *Primary biological aerosol particles in the atmosphere: a review*, Tellus B: Chemical and Physical Meteorology, 64, 15 598, 2012.

Diehl, K. and Wurzler, S.: *Heterogeneous Drop Freezing in the Immersion Mode: Model Calculations Considering Soluble and Insoluble Particles in the Drops*, Journal of the Atmospheric Sciences, 61, 2063–2072, 2004.

Dietmüller, S., Jöckel, P., Tost, H., Kunze, M., Gellhorn, C., Brinkop, S., Frömming, C., Ponater, M., Steil, B., Lauer, A., and Hendricks, J.: *A new radiation infrastructure for the Modular Earth Submodel System (MESSy, based on version 2.51)*, Geoscientific Model Development, 9, 2209–2222, 2016.

Donner, L. J., O'Brien, T. A., Rieger, D., Vogel, B., and Cooke, W. F.: *Are atmospheric updrafts a key to unlocking climate forcing and sensitivity?*, Atmospheric Chemistry and Physics, 16, 12 983–12 992, 2016.

Duncan, D. I. and Eriksson, P.: *An update on global atmospheric ice estimates from satellite observations and reanalyses*, Atmospheric Chemistry and Physics, 18, 11 205–11 219, 2018.

Eichinger, R. and Jöckel, P.: *The generic MESSy submodel TENDENCY (v1.0) for process-based analyses in Earth system models*, Geoscientific Model Development, 7, 1573–1582, 2014.

Field, P. R., Lawson, R. P., Brown, P. R. A., Lloyd, G., Westbrook, C., Moisseev, D., Miltenberger, A., Nenes, A., Blyth, A., Choularton, T., Connolly, P., Buehl, J., Crosier, J., Cui, Z., Dearden, C., DeMott, P., Flossmann, A., Heymsfield, A., Huang, Y., Kalesse, H., Kanji, Z. A., Korolev, A., Kirchgaessner, A., Lasher-Trapp, S., Leisner, T., McFarquhar, G., Phillips, V., Stith, J., and Sullivan, S.: *Secondary Ice Production: Current State of the Science and Recommendations for the Future*, Meteorological Monographs, 58, 7.1–7.20, 2017.

Fletcher, N. H.: *Surface structure of water and ice*, The Philosophical Magazine: A Journal of Theoretical Experimental and Applied Physics, 7, 255–269, 1962.

Fountoukis, C. and Nenes, A.: *ISORROPIA II: a computationally efficient thermodynamic equilibrium model for K^+-Ca^{2+}-Mg^{2+}-NH_4^+-Na^+-SO_4^{2-}-NO_3^--Cl^--H_2O aerosols*, Atmospheric Chemistry and Physics, 7, 4639–4659, 2007.

Fuchs, N.: The Mechanics of aerosols, New York, 1964.

Ganzeveld, L. N., van Aardenne, J. A., Butler, T. M., Lawrence, M. G., Metzger, S. M., Stier, P., Zimmermann, P., and Lelieveld, J.: *Technical Note: Anthropogenic and natural offline emissions and the online EMissions and dry DEPosition submodel EMDEP of the Modular Earth Submodel system (MESSy)*, Atmospheric Chemistry and Physics Discussions, 6, 5457–5483, 2006.

Gasparini, B. and Lohmann, U.: *Why cirrus cloud seeding cannot substantially cool the planet*, Journal of Geophysical Research: Atmospheres, 121, 4877–4893, 2016.

Gasparini, B., Meyer, A., Neubauer, D., Münch, S., and Lohmann, U.: *Cirrus Cloud Properties as Seen by the CALIPSO Satellite and ECHAM-HAM Global Climate Model*, Journal of Climate, 31, 1983–2003, 2018.

Gettelman, A., Liu, X., Ghan, S. J., Morrison, H., Park, S., Conley, A. J., Klein, S. A., Boyle, J., Mitchell, D. L., and Li, J.-L. F.: *Global simulations of ice nucleation and ice supersaturation with an improved cloud scheme in the Community Atmosphere Model*, Journal of Geophysical Research: Atmospheres, 115, n/a–n/a, 2010.

Gettelman, A., Liu, X., Barahona, D., Lohmann, U., and Chen, C.: *Climate impacts of ice nucleation*, Journal of Geophysical Research: Atmospheres, 117, n/a–n/a, 2012.

Gettelman, A., Morrison, H., Terai, C. R., and Wood, R.: *Microphysical process rates and global aerosol–cloud interactions*, Atmospheric Chemistry and Physics, 13, 9855–9867, 2013.

Greenfield, S. M.: *Rain scavenging of radioactive particulate matter from the atmosphere*, Journal of Meteorology, 14, 115–125, 1957.

Grewe, V., Brunner, D., Dameris, M., Grenfell, J., Hein, R., Shindell, D., and Staehelin, J.: *Origin and variability of upper tropospheric nitrogen oxides and ozone at northern mid-latitudes*, Atmospheric Environment, 35, 3421–3433, 2001.

Gryspeerdt, E., Quaas, J., Goren, T., Klocke, D., and Brueck, M.: *An automated cirrus classification*, Atmospheric Chemistry and Physics, 18, 6157–6169, 2018a.

Gryspeerdt, E., Sourdeval, O., Quaas, J., Delanoë, J., Krämer, M., and Kühne, P.: *Ice crystal number concentration estimates from lidar–radar satellite remote sensing – Part 2: Controls on the ice crystal number concentration*, Atmospheric Chemistry and Physics, 18, 14 351–14 370, 2018b.

Guo, H., Liu, Y., Daum, P. H., Senum, G. I., and Tao, W.-K.: *Characteristics of vertical velocity in marine stratocumulus: comparison of large eddy simulations with observations*, Environmental Research Letters, 3, 1–8, 2008.

Haag, W., Kärcher, B., Ström, J., Minikin, A., Lohmann, U., Ovarlez, J., and Stohl, A.: *Freezing thresholds and cirrus cloud formation mechanisms inferred from in situ measurements of relative humidity*, Atmospheric Chemistry and Physics, 3, 1791–1806, 2003.

Hagen, M., Höller, H., and Schmidt, K.: Cloud and Precipitation Radar, Springer–Verlag Berlin Heidelberg, 2012.

Hallett, J. and Mossp, S. C.: *Production of secondary ice particles during the riming process*, Nature, 249, 26–28, 1974.

Han, Q., Rossow, W. B., and Lacis, A. A.: *Near-Global Survey of Effective Droplet Radii in Liquid Water Clouds Using ISCCP Data*, Journal of Climate, 7, 465–497, 1994.

Heald, C. L. and Spracklen, D. V.: *Atmospheric budget of primary biological aerosol particles from fungal spores*, Geophysical Research Letters, 36, 2009.

Hendricks, J., Kärcher, B., and Lohmann, U.: *Effects of ice nuclei on cirrus clouds in a global climate model*, Journal of Geophysical Research: Atmospheres, 116, n/a–n/a, 2011.

Heymsfield, A. J., Bansemer, A., Heymsfield, G., and Fierro, A. O.: *Microphysics of Maritime Tropical Convective Updrafts at Temperatures from −20° to −60°*, Journal of the Atmospheric Sciences, 66, 3530–3562, 2009.

Heymsfield, A. J., Schmitt, C., and Bansemer, A.: *Ice Cloud Particle Size Distributions and Pressure-Dependent Terminal Velocities from In Situ Observations at Temperatures from 0° to -86°C*, Journal of the Atmospheric Sciences, 70, 4123–4154, 2013.

Heymsfield, A. J., Krämer, M., Luebke, A., Brown, P., Cziczo, D. J., Franklin, C., Lawson, P., Lohmann, U., McFarquhar, G., Ulanowski, Z., and Van Tricht, K.: *Cirrus Clouds*, Meteorological Monographs, 58, 2.1–2.26, 2017.

Hong, Y., Liu, G., and Li, J.-L. F.: *Assessing the Radiative Effects of Global Ice Clouds Based on CloudSat and CALIPSO Measurements*, Journal of Climate, 29, 7651–7674, 2016.

Hoose, C. and Möhler, O.: *Heterogeneous ice nucleation on atmospheric aerosols: a review of results from laboratory experiments*, Atmospheric Chemistry and Physics, 12, 9817–9854, 2012.

Hoose, C., Lohmann, U., Bennartz, R., Croft, B., and Lesins, G.: *Global simulations of aerosol processing in clouds*, Atmospheric Chemistry and Physics, 8, 6939–6963, 2008a.

Hoose, C., Lohmann, U., Erdin, R., and Tegen, I.: *The global influence of dust mineralogical composition on heterogeneous ice nucleation in mixed-phase clouds*, Environmental Research Letters, 3, 025 003, 2008b.

Hoose, C., Kristjánsson, J. E., and Burrows, S. M.: *How important is biological ice nucleation in clouds on a global scale?*, Environmental Research Letters, 5, 024 009, 2010a.

Hoose, C., Kristjánsson, J. E., Chen, J.-P., and Hazra, A.: *A Classical-Theory-Based Parameterization of Heterogeneous Ice Nucleation by Mineral Dust, Soot, and Biological Particles in a Global Climate Model*, Journal of the Atmospheric Sciences, 67, 2483–2503, 2010b.

Hurrell, J. W., Hack, J. J., Shea, D., Caron, J. M., and Rosinski, J.: *A New Sea Surface Temperature and Sea Ice Boundary Dataset for the Community Atmosphere Model*, Journal of Climate, 21, 5145–5153, 2008.

ICE-L: *Continuous Flow Diffusion Chamber Ice Nuclei. Version 1.0. UCAR/NCAR - Earth Observing Laboratory*, 2011.

Ickes, L., Welti, A., Corinna, H., and Lohmann, U.: *Classical nucleation theory of homogeneous freezing of water: thermodynamic and kinetic parameters*, Physical Chemistry Chemical Physics, 17, 5514–5537, 2015.

IPCC: Climate Change 2013: The Physical Science Basis, Cambridge University Press, 2013.

Jacobson, M. Z. and Streets, D. G.: *Influence of future anthropogenic emissions on climate, natural emissions, and air quality*, Journal of Geophysical Research: Atmospheres, 114, D08 118, 2009.

Jensen, E. J., Diskin, G., Lawson, R. P., Lance, S., Bui, T. P., Hlavka, D., McGill, M., Pfister, L., Toon, O. B., and Gao, R.: *Ice nucleation and dehydration in the Tropical Tropopause Layer*, Proceedings of the National Academy of Sciences, 110, 2041–2046, 2013.

Jöckel, P.: Earth System Modeling, Springer, Berlin, Heidelberg, 2012.

Jöckel, P., Sander, R., Kerkweg, A., Tost, H., and Lelieveld, J.: *Technical Note: The Modular Earth Submodel System (MESSy) - a new approach towards Earth System Modeling*, Atmospheric Chemistry and Physics, 5, 433–444, 2005.

Jöckel, P., Tost, H., Pozzer, A., Brühl, C., Buchholz, J., Ganzeveld, L., Hoor, P., Kerkweg, A., Lawrence, M. G., Sander, R., Steil, B., Stiller, G., Tanarhte, M., Taraborrelli, D., van Aardenne, J., and Lelieveld, J.: *The atmospheric chemistry general circulation model ECHAM5/MESSy1: consistent simulation of ozone from the surface to the mesosphere*, Atmospheric Chemistry and Physics, 6, 5067–5104, 2006.

Jöckel, P., Kerkweg, A., Buchholz-Dietsch, J., Tost, H., Sander, R., and Pozzer, A.: *Technical Note: Coupling of chemical processes with the Modular Earth Submodel System (MESSy) submodel TRACER*, Atmospheric Chemistry and Physics, 8, 1677–1687, 2008.

Jöckel, P., Tost, H., Pozzer, A., Kunze, M., Kirner, O., Brenninkmeijer, C. A. M., Brinkop, S., Cai, D. S., Dyroff, C., Eckstein, J., Frank, F., Garny, H., Gottschaldt, K.-D., Graf, P., Grewe, V., Kerkweg, A., Kern, B., Matthes, S., Mertens, M., Meul, S., Neumaier, M., Nützel, M., Oberländer-Hayn, S., Ruhnke, R., Runde, T., Sander, R., Scharffe, D., and Zahn, A.: *Earth System Chemistry integrated Modelling (ESCiMo) with the Modular Earth Submodel System (MESSy) version 2.51*, Geoscientific Model Development, 9, 1153–1200, 2016.

Joos, H., Spichtinger, P., Lohmann, U., Gayet, J.-F., and Minikin, A.: *Orographic cirrus in the global climate model ECHAM5*, Journal of Geophysical Research: Atmospheres, 113, 2008.

Kalnay, E.: Atmospheric Modeling, Data Assimilation and Predictability, Cambridge University Press, 2002.

Kanji, Z. A., Ladino, L. A., Wex, H., Boose, Y., Burkert-Kohn, M., Cziczo, D. J., and Krämer, M.: *Overview of Ice Nucleating Particles*, Meteorological Monographs, 58, 1.1–1.33, 2017.

Kärcher, B. and Lohmann, U.: *A parameterization of cirrus cloud formation: Homogeneous freezing of supercooled aerosols*, Journal of Geophysical Research: Atmospheres, 107, AAC 4–1–AAC 4–10, 2002a.

Kärcher, B. and Lohmann, U.: *A Parameterization of cirrus cloud formation: Homogeneous freezing including effects of aerosol size*, Journal of Geophysical Research: Atmospheres, 107, AAC 9–1–AAC 9–10, 2002b.

Kärcher, B. and Lohmann, U.: *A parameterization of cirrus cloud formation: Heterogeneous freezing*, Journal of Geophysical Research: Atmospheres, 108, n/a–n/a, 2003.

Kärcher, B. and Ström, J.: *The roles of dynamical variability and aerosols in cirrus cloud formation*, Atmospheric Chemistry and Physics, 3, 823–838, 2003.

Kärcher, B., Hendricks, J., and Lohmann, U.: *Physically based parameterization of cirrus cloud formation for use in global atmospheric models*, Journal of Geophysical Research: Atmospheres, 111, n/a–n/a, 2006.

Karydis, V. A., Kumar, P., Barahona, D., Sokolik, I. N., and Nenes, A.: *On the effect of dust particles on global cloud condensation nuclei and cloud droplet number*, Journal of Geophysical Research: Atmospheres, 116, 2011.

Karydis, V. A., Tsimpidi, A. P., Bacer, S., Pozzer, A., Nenes, A., and Lelieveld, J.: *Global impact of mineral dust on cloud droplet number concentration*, Atmospheric Chemistry and Physics, 17, 5601–5621, 2017.

Kellogg, C. A. and Griffin, D. W.: *Aerobiology and the global transport of desert dust*, Trends in Ecology & Evolution, 21, 638–644, 2006.

Kerkweg, A., Buchholz, J., Ganzeveld, L., Pozzer, A., Tost, H., and Jöckel, P.: *Technical Note: An implementation of the dry removal processes DRY DEPosition and SEDImentation in the Modular Earth Submodel System (MESSy)*, Atmospheric Chemistry and Physics, 6, 4617–4632, 2006a.

Kerkweg, A., Sander, R., Tost, H., and Jöckel, P.: *Technical note: Implementation of prescribed (OFFLEM), calculated (ONLEM), and pseudo-emissions (TNUDGE) of chemical species in the Modular Earth Submodel System (MESSy)*, Atmospheric Chemistry and Physics, 6, 3603–3609, 2006b.

Kerkweg, A., Jöckel, P., Pozzer, A., Tost, H., Sander, R., Schulz, M., Stier, P., Vignati, E., Wilson, J., and Lelieveld, J.: *Consistent simulation of bromine chemistry from the marine boundary layer to the stratosphere – Part 1: Model description, sea salt aerosols and pH*, Atmospheric Chemistry and Physics, 8, 5899–5917, 2008.

Kettle, A. J., Andreae, M. O., Amouroux, D., Andreae, T. W., Bates, T. S., Berresheim, H., Bingemer, H., Boniforti, R., Curran, M. A. J., DiTullio, G. R., Helas, G., Jones, G. B., Keller, M. D., Kiene, R. P., Leck, C., Levasseur, M., Malin, G., Maspero, M., Matrai, P., McTaggart, A. R., Mihalopoulos, N., Nguyen, B. C., Novo, A., Putaud, J. P., Rapsomanikis, S., Roberts, G., Schebeske, G., Sharma, S., SimÛ, R., Staubes, R., Turner, S., and Uher, G.: *A global database of sea surface dimethylsulfide (DMS) measurements and a procedure to predict sea surface DMS as a function of latitude, longitude, and month*, Global Biogeochemical Cycles, 13, 399–444, 1999.

Khain, A. P. and Pinsky, M.: Physical processes in clouds and in cloud modeling, Cambridge University Press, 2018.

Koop, T., Luo, B., Tsias, A., and Peter, T.: *Water activity as the determinant for homogeneous ice nucleation in aqueous solutions*, Nature, 406, 611–614, 2000.

Korolev, A.: *Limitations of the Wegener–Bergeron–Findeisen Mechanism in the Evolution of Mixed-Phase Clouds*, Journal of the Atmospheric Sciences, 64, 3372–3375, 2007.

Korolev, A., McFarquhar, G., Field, P. R., Franklin, C., Lawson, P., Wang, Z., Williams, E., Abel, S. J., Axisa, D., Borrmann, S., Crosier, J., Fugal, J., Krämer, M., Lohmann, U., Schlenczek, O., Schnaiter, M., and Wendisch, M.: *Mixed-Phase Clouds: Progress and Challenges*, Meteorological Monographs, 58, 5.1–5.50, 2017.

Krämer, M., Schiller, C., Afchine, A., Bauer, R., Gensch, I., Mangold, A., Schlicht, S., Spelten, N., Sitnikov, N., Borrmann, S., de Reus, M., and Spichtinger, P.: *Ice supersaturations and cirrus cloud crystal numbers*, Atmospheric Chemistry and Physics, 9, 3505–3522, 2009.

Krämer, M., Rolf, C., Luebke, A., Afchine, A., Spelten, N., Costa, A., Meyer, J., Zöger, M., Smith, J., Herman, R. L., Buchholz, B., Ebert, V., Baumgardner, D., Borrmann, S., Klingebiel, M., and Avallone, L.: *A microphysics guide to cirrus clouds – Part 1: Cirrus types*, Atmospheric Chemistry and Physics, 16, 3463–3483, 2016.

Kuebbeler, M., Lohmann, U., Hendricks, J., and Kärcher, B.: *Dust ice nuclei effects on cirrus clouds*, Atmospheric Chemistry and Physics, 14, 3027–3046, 2014.

Kulmala, M., Laaksonen, A., and Pirjola, L.: *Parameterizations for sulfuric acid/water nucleation rates*, Journal of Geophysical Research: Atmospheres, 103, 8301–8307, 1998.

Kumar, P., Sokolik, I. N., and Nenes, A.: *Parameterization of cloud droplet formation for global and regional models: including adsorption activation from insoluble CCN*, Atmospheric Chemistry and Physics, 9, 2517–2532, 2009.

Kumar, P., Sokolik, I. N., and Nenes, A.: *Cloud condensation nuclei activity and droplet activation kinetics of wet processed regional dust samples and minerals*, Atmospheric Chemistry and Physics, 11, 8661–8676, 2011.

Landgraf, J. and Crutzen, P. J.: *An Efficient Method for Online Calculations of Photolysis and Heating Rates*, Journal of the Atmospheric Sciences, 55, 863–878, 1998.

Lauer, A., Eyring, V., Hendricks, J., Jöckel, P., and Lohmann, U.: *Global model simulations of the impact of ocean-going ships on aerosols, clouds, and the radiation budget*, Atmospheric Chemistry and Physics, 7, 5061–5079, 2007.

Lawrence, M. G. and Rasch, P. J.: *Tracer Transport in Deep Convective Updrafts: Plume Ensemble versus Bulk Formulations*, Journal of the Atmospheric Sciences, 62, 2880–2894, 2005.

Levkov, L., Rockel, B., Kapitza, H., and E., R.: *3D mesoscale numerical studies of cirrus and stratus clouds by their time and space evolution*, Beitr. Phys. Atmos, 65, 35–58, 1992.

Li, J.-L. F., Waliser, D. E., Chen, W.-T., Guan, B., Kubar, T., Stephens, G., Ma, H.-Y., Deng, M., Donner, L., Seman, C., and Horowitz, L.: *An observationally based evaluation of cloud ice water in CMIP3 and CMIP5 GCMs and contemporary reanalyses using contemporary satellite data*, Journal of Geophysical Research: Atmospheres, 117, n/a–n/a, 2012.

Lin, H. and Leaitch, W. R.: *Development of an in-cloud aerosol activation parameterization for climate modelling in: Proceedings of the WMO Workshop on measurement of Cloud Properties for Forecasts of Weather, Air Quality and Climate*, World Meteorological Organization, Geneva, pp. 328–335, 1997.

Lin, S.-J. and Rockel, B. B.: *Multidimensional Flux-Form Semi–Lagrangian Transport Schemes*, Monthly Weather Review, 124, 2046–2070, 1996.

Lin, Y.-L., Farley, R. D., and Orville, H. D.: *Bulk Parameterization of the Snow Field in a Cloud Model*, Journal of Climate and Applied Meteorology, 22, 1065–1092, 1983.

Liu, X. and Penner, J. E.: *Ice nucleation parameterization for global models*, Meteorological Magazine, 14, 499–514, 2005.

Liu, X., Penner, J. E., Ghan, S. J., and Wang, M.: *Inclusion of Ice Microphysics in the NCAR Community Atmospheric Model Version 3 (CAM3)*, Journal of Climate, 20, 4526–4547, 2007.

Liu, X., Shi, X., Zhang, K., Jensen, E. J., Gettelman, A., Barahona, D., Nenes, A., and Lawson, P.: *Sensitivity studies of dust ice nuclei effect on cirrus clouds with the Community Atmosphere Model CAM5*, Atmospheric Chemistry and Physics, 12, 12 061–12 079, 2012.

Lohmann, U.: *Possible Aerosol Effects on Ice Clouds via Contact Nucleation*, Journal of the Atmospheric Sciences, 59, 647–656, 2002.

Lohmann, U.: *Anthropogenic Aerosol Influences on Mixed-Phase Clouds*, Current Climate Change Reports, 3, 32–44, 2017.

Lohmann, U. and Diehl, K.: *Sensitivity Studies of the Importance of Dust Ice Nuclei for the Indirect Aerosol Effect on Stratiform Mixed-Phase Clouds*, Journal of the Atmospheric Sciences, 63, 968–982, 2006.

Lohmann, U. and Feichter, J.: *Global indirect aerosol effects: a review*, Atmospheric Chemistry and Physics, 5, 715–737, 2005.

Lohmann, U. and Hoose, C.: *Sensitivity studies of different aerosol indirect effects in mixed-phase clouds*, Atmospheric Chemistry and Physics, 9, 8917–8934, 2009.

Lohmann, U. and Kärcher, B.: *First interactive simulations of cirrus clouds formed by homogeneous freezing in the ECHAM general circulation model*, Journal of Geophysical Research: Atmospheres, 107, AAC 8–1–AAC 8–13, 2002.

Lohmann, U. and Roeckner, E.: *Design and performance of a new cloud microphysics scheme developed for the ECHAM general circulation model*, Climate Dynamics, 12, 557–572, 1996.

Lohmann, U., Feichter, J., Chuang, C. C., and Penner, J. E.: *Prediction of the number of cloud droplets in the ECHAM GCM*, Journal of Geophysical Research: Atmospheres, 104, 9169–9198, 1999.

Lohmann, U., Quaas, J., Kinne, S., and Feichter, J.: *Different Approaches for Constraining Global Climate Models of the Anthropogenic Indirect Aerosol Effect*, Bulletin of the American Meteorological Society, 88, 243–250, 2007a.

Lohmann, U., Stier, P., Hoose, C., Ferrachat, S., Kloster, S., Roeckner, E., and Zhang, J.: *Cloud microphysics and aerosol indirect effects in the global climate model ECHAM5-HAM*, Atmospheric Chemistry and Physics, 7, 3425–3446, 2007b.

Lohmann, U., Spichtinger, P., Jess, S., Peter, T., and Smit, H.: *Cirrus cloud formation and ice supersaturated regions in a global climate model*, Environmental Research Letters, 3, 045 022, 2008.

Lohmann, U., Lüönd, F., and Mahrt, F.: An introduction to clouds from the microscale to climate, Cambridge University Press, 2016.

Matus, A. V. and L'Ecuyer, T. S.: *The role of cloud phase in Earth's radiation budget*, Journal of Geophysical Research: Atmospheres, 122, 2559–2578, 2017.

Meyers, M. P., DeMott, P. J., and Cotton, W. R.: *New Primary Ice-Nucleation Parameterizations in an Explicit Cloud Model*, Journal of Applied Meteorology, 31, 708–721, 1992.

Milankovitch, M. M.: Canon of Insolation and the Ice–Age Problem, U.S. Department of Commerce and the National Science Foundation, Washington, D.C., 1941.

Morales, R. and Nenes, A.: *Characteristic updrafts for computing distribution?averaged cloud droplet number and stratocumulus cloud properties*, Journal of Geophysical Research: Atmospheres, 115, 2010.

Murray, B. J., Wilson, T. W., Dobbie, S., Cui, Z., Al-Jumur, S. M. R. K., Möhler, O., Schnaiter, M., Wagner, R., Benz, S., Niemand, M., Saathoff, H., Ebert, V., Wagner, S., and Kärcher, B.: *Heterogeneous nucleation of ice particles on glassy aerosols under cirrus conditions*, Nature Geoscience, 3, 233–237, 2010.

Murray, B. J., D., O., Atkinson, J. D., and Webb, M. E.: *Ice nucleation by particles immersed in supercooled cloud droplets*, Chem. Soc. Rev., 41, 6519–6554, 2012.

Nordeng, T. E.: *Extended versions of the convection parametrization scheme at ECMWF and their impact upon the mean climate and transient activity of the model in the tropics*, ECMWF Tech. Memo. No. 206, 1994.

Petters, M. D. and Kreidenweis, S. M.: *A single parameter representation of hygroscopic growth and cloud condensation nucleus activity*, Atmospheric Chemistry and Physics, 7, 1961–1971, 2007.

Phillips, V. T. J., Donner, L. J., and Garner, S. T.: *Nucleation Processes in Deep Convection Simulated by a Cloud-System-Resolving Model with Double-Moment Bulk Microphysics*, Journal of the Atmospheric Sciences, 64, 738–761, 2007.

Phillips, V. T. J., DeMott, P. J., and Andronache, C.: *An Empirical Parameterization of Heterogeneous Ice Nucleation for Multiple Chemical Species of Aerosol*, Journal of the Atmospheric Sciences, 65, 2757–2783, 2008.

Phillips, V. T. J., Demott, P. J., Andronache, C., Pratt, K. A., Prather, K. A., Subramanian, R., and Twohy, C.: *Improvements to an Empirical Parameterization of Heterogeneous Ice Nucleation and Its Comparison with Observations*, Journal of the Atmospheric Sciences, 70, 378–409, 2013.

Pozzer, A., Jöckel, P., Sander, R., Williams, J., Ganzeveld, L., and Lelieveld, J.: *Technical Note: The MESSy-submodel AIRSEA calculating the air-sea exchange of chemical species*, Atmospheric Chemistry and Physics, 6, 5435–5444, 2006.

Pozzer, A., de Meij, A., Pringle, K. J., Tost, H., Doering, U. M., van Aardenne, J., and Lelieveld, J.: *Distributions and regional budgets of aerosols and their precursors simulated with the EMAC chemistry-climate model*, Atmospheric Chemistry and Physics, 12, 961–987, 2012.

Pratt, K. A., DeMott, P. J., French, J. R., Wang, Z., Westphal, D. L., Heymsfield, A. J., Twohy, C. H., Prenni, A. J., and Prather, K. A.: *In situ detection of biological particles in cloud ice-crystals*, Nature Geoscience, 2, 398–401, 2009.

Prenni, A. J., Petters, M. D., Kreidenweis, S. M., Heald, C. L., Martin, S. T., Artaxo, P., Garland, R. M., Wollny, A. G., and Pöschl, U.: *Relative roles of biogenic emissions and Saharan dust as ice nuclei in the Amazon basin*, Nature Geoscience, 2, 402–405, 2009.

Pringle, K. J., Tost, H., Message, S., Steil, B., Giannadaki, D., Nenes, A., Fountoukis, C., Stier, P., Vignati, E., and Lelieveld, J.: *Description and evaluation of GMXe: a new aerosol submodel for global simulations (v1)*, Geoscientific Model Development, 3, 391–412, 2010.

Prinn, R. G., Weiss, R. F., Fraser, P. J., Simmonds, P. G., Cunnold, D. M., Alyea, F. N., O'Doherty, S., Salameh, P., Miller, B. R., Huang, J., Wang, R. H. J., Hartley, D. E., Harth, C., Steele, L. P., Sturrock, G., Midgley, P. M., and McCulloch, A.: *A history of chemically and radiatively important gases in air deduced from ALE/GAGE/AGAGE*, Journal of Geophysical Research: Atmospheres, 105, 17 751–17 792, 2000.

Pruppacher, H. R. and Klett, J. D.: Microphysics of Clouds and Precipitation, Springer, New York, 1997.

Righi, M., Hendricks, J., and Sausen, R.: *The global impact of the transport sectors on atmospheric aerosol in 2030 – Part 2: Aviation*, Atmospheric Chemistry and Physics, 16, 4481–4495, 2016.

Roeckner, E., Brokopf, R., Esch, M., Giorgetta, M., Hagemann, S., Kornblueh, L., Schlese, U., Schulzweida, U., and Manzini, E.: The Atmospheric General Circulation Model ECHAM5, Part II, Max-Planck-Institut für Meteorologie, 2004.

Rogers, R. R. and Yau, M. K.: A short course in cloud physics, Butterworth-Heinemann, 3rd edn., 1989.

Salzmann, M., Ming, Y., Golaz, J.-C., Ginoux, P. A., Morrison, H., Gettelman, A., Krämer, M., and Donner, L. J.: *Two-moment bulk stratiform cloud microphysics in the GFDL AM3 GCM: description, evaluation, and sensitivity tests*, Atmospheric Chemistry and Physics, 10, 8037–8064, 2010.

Sander, R., Kerkweg, A., Jöckel, P., and Lelieveld, J.: *Technical note: The new comprehensive atmospheric chemistry module MECCA*, Atmospheric Chemistry and Physics, 5, 445–450, 2005.

Sander, R., Baumgaertner, A., Gromov, S., Harder, H., Jöckel, P., Kerkweg, A., Kubistin, D., Regelin, E., Riede, H., Sandu, A., Taraborrelli, D., Tost, H., and Xie, Z.-Q.: *The atmospheric chemistry box model CAABA/MECCA-3.0*, Geoscientific Model Development, 4, 373–380, 2011.

Sander, R., Jöckel, P., Kirner, O., Kunert, A. T., Landgraf, J., and Pozzer, A.: *The photolysis module JVAL-14, compatible with the MESSy standard, and the JVal PreProcessor (JVPP)*, Geoscientific Model Development, 7, 2653–2662, 2014.

Sandu, A. and Sander, R.: *Technical note: Simulating chemical systems in Fortran90 and Matlab with the Kinetic PreProcessor KPP–2.1*, Atmospheric Chemistry and Physics, 6, 187–195, 2006.

Satoh, M.: Atmospheric Circulation Dynamics and General Circulation Models, Springer-Verlag Berlin Heidelberg, 2nd edn., 2014.

Seinfeld, J. H. and Pandis, S. N.: Atmospheric Chemistry and Physics: from Air Pollution to Climate Change, John Wiley & Sons, 2nd edn., 2006.

Seinfeld, J. H., Bretherton, C., Carslaw, K. S., Coe, H., DeMott, P. J., Dunlea, E. J., Feingold, G., Ghan, S., Guenther, A. B., Kahn, R., Kraucunas, I., Kreidenweis, S. M., Molina, M. J., Nenes, A., Penner, J. E., Prather, K. A., Ramanathan, V., Ramaswamy, V., Rasch, P. J., Ravishankara, A. R., Rosenfeld, D., Stephens, G., and Wood, R.: *Improving our fundamental understanding of the role of aerosol-cloud interactions in the climate system*, Proceedings of the National Academy of Sciences, 113, 5781–5790, 2016.

Shi, X., Liu, X., and Zhang, K.: *Effects of pre-existing ice crystals on cirrus clouds and comparison between different ice nucleation parameterizations with the Community Atmosphere Model (CAM5)*, Atmospheric Chemistry and Physics, 15, 1503–1520, 2015.

Sourdeval, O., Gryspeerdt, E., Krämer, M., Goren, T., Delanoë, J., Afchine, A., Hemmer, F., and Quaas, J.: *Ice crystal number concentration estimates from lidar–radar satellite remote sensing – Part 1: Method and evaluation*, Atmospheric Chemistry and Physics, 18, 14 327–14 350, 2018.

Spichtinger, P. and Cziczo, D. J.: *Impact of heterogeneous ice nuclei on homogeneous freezing events in cirrus clouds*, Journal of Geophysical Research: Atmospheres, 115, 2010.

Spichtinger, P. and Krämer, M.: *Tropical tropopause ice clouds: a dynamic approach to the mystery of low crystal numbers*, Atmospheric Chemistry and Physics, 13, 9801–9818, 2013.

Stier, P., Feichter, J., Kinne, S., Kloster, S., Vignati, E., Wilson, J., Ganzeveld, L., Tegen, I., Werner, M., Balkanski, Y., Schulz, M., Boucher, O., Minikin, A., and Petzold, A.: *The aerosol-climate model ECHAM5-HAM*, Atmospheric Chemistry and Physics, 5, 1125–1156, 2005.

Storelvmo, T.: *Aerosol Effects on Climate via Mixed-Phase and Ice Clouds*, Annual Review of Earth and Planetary Sciences, 45, 199–222, 2017.

Storelvmo, T. and Tan, I.: *The Wegener-Bergeron-Findeisen process – Its discovery and vital importance for weather and climate*, Meteorologische Zeitschrift, 24, 455–461, 2015.

Storelvmo, T., Kristj·nsson, J. E., and Lohmann, U.: *Aerosol Influence on Mixed-Phase Clouds in CAM-Oslo*, Journal of the Atmospheric Sciences, 65, 3214–3230, 2008.

Sullivan, S. C., Morales Betancourt, R., Barahona, D., and Nenes, A.: *Understanding cirrus ice crystal number variability for different heterogeneous ice nucleation spectra*, Atmospheric Chemistry and Physics, 16, 2611–2629, 2016.

Sundqvist, H., Berge, E., and Kristjansson, J. E.: *Condensation and Cloud Parameterization Studies with a Mesoscale NUmerical Weather Prediction Model*, Monthly Weather Review, 117, 1641–1657, 1989.

Tanre, D., Geleyn, J.-F., and Slingo, J. M.: First results of the introduction of an advanced aerosol-radiation interaction in the ECMWF low resolution global model, in: Aerosols and their climatic effects, A. Deepak, 1984.

Tiedtke, M.: *A Comprehensive Mass Flux Scheme for Cumulus Parameterization in Large-Scale Models*, Monthly Weather Review, 117, 1779–1800, 1989.

Tompkins, A. M.: *A Prognostic Parameterization for the Subgrid-Scale Variability of Water Vapor and Clouds in Large-Scale Models and Its Use to Diagnose Cloud Cover*, Journal of the Atmospheric Sciences, 59, 1917–1942, 2002.

Tost, H.: *Chemistry–climate interactions of aerosol nitrate from lightning*, Atmospheric Chemistry and Physics, 17, 1125–1142, 2017.

Tost, H., Jöckel, P., Kerkweg, A., Sander, R., and Lelieveld, J.: *Technical note: A new comprehensive SCAVenging submodel for global atmospheric chemistry modelling*, Atmospheric Chemistry and Physics, 6, 565–574, 2006a.

Tost, H., Jöckel, P., and Lelieveld, J.: *Influence of different convection parameterisations in a GCM*, Atmospheric Chemistry and Physics, 6, 5475–5493, 2006b.

Tost, H., Jöckel, P., and Lelieveld, J.: *Lightning and convection parameterisations – uncertainties in global modelling*, Atmospheric Chemistry and Physics, 7, 4553–4568, 2007.

Tost, H., Lawrence, M. G., Brühl, C., Jöckel, P., Team, T. G., and Team, T. S.-O.-D.: *Uncertainties in atmospheric chemistry modelling due to convection parameterisations and subsequent scavenging*, Atmospheric Chemistry and Physics, 10, 1931–1951, 2010.

van der Werf, G. R., Randerson, J. T., Giglio, L., Collatz, G. J., Mu, M., Kasibhatla, P. S., Morton, D. C., DeFries, R. S., Jin, Y., and van Leeuwen, T. T.: *Global fire emissions and the contribution of deforestation, savanna, forest, agricultural, and peat fires (1997–2009)*, Atmospheric Chemistry and Physics, 10, 11 707–11 735, 2010.

Vehkamäki, H., Kulmala, M., Napari, I., Lehtinen, K. E. J., Timmreck, C., Noppel, M., and Laaksonen, A.: *An improved parameterization for sulfuric acid?water nucleation rates for tropospheric and stratospheric conditions*, Journal of Geophysical Research: Atmospheres, 107, AAC 3–1–AAC 3–10, 2002.

Vignati, E., Wilson, J., and Stier, P.: *M7: An efficient size-resolved aerosol microphysics module for large-scale aerosol transport models*, Journal of Geophysical Research: Atmospheres, 109, 2004.

Voigt, C., Schumann, U., Minikin, A., Abdelmonem, A., Afchine, A., Borrmann, S., Boettcher, M., Buchholz, B., Bugliaro, L., Costa, A., Curtius, J., Dollner, M., Dörnbrack, A., Dreiling, V., Ebert, V., Ehrlich, A., Fix, A., Forster, L., Frank, F., F¸tterer, D., Giez, A., Graf, K., Groofl, J.-U., Grofl, S., Heimerl, K., Heinold, B., Hüneke, T., Järvinen, E., Jurkat, T., Kaufmann, S., Kenntner, M., Klingebiel, M., Klimach, T., Kohl, R., Krämer, M., Krisna, T. C., Luebke, A., Mayer, B., Mertes, S., Molleker, S., Petzold, A., Pfeilsticker, K., Port, M., Rapp, M., Reutter, P., Rolf, C., Rose, D., Sauer, D., Schäfler, A., Schlage, R., Schnaiter, M., Schneider, J., Spelten, N., Spichtinger, P., Stock, P., Walser, A., Weigel, R., Weinzierl, B., Wendisch, M., Werner, F., Wernli, H., Wirth, M., Zahn, A., Ziereis, H., and Z^ger, M.: *ML-CIRRUS: The Airborne Experiment on Natural Cirrus and Contrail Cirrus with the High-Altitude Long-Range Research Aircraft HALO*, Bulletin of the American Meteorological Society, 98, 271–288, 2017.

Waliser, D. E., Li, J.-L. F., Woods, C. P., Austin, R. T., Bacmeister, J., Chern, J., Del, G. A., Jiang, J. H., Kuang, Z., Meng, H., Minnis, P., Platnick, S., Rossow, W. B., Stephens, G. L., Sun-Mack, S., Tao, W.-K., Tompkins, A. M., Vane, D. G., Walker, C., and Wu, D.: *Cloud ice: A climate model challenge with signs and expectations of progress*, Journal of Geophysical Research: Atmospheres, 114, 2009.

Wang, M. and Penner, J. E.: *Cirrus clouds in a global climate model with a statistical cirrus cloud scheme*, Atmospheric Chemistry and Physics, 10, 5449–5474, 2010.

Wilson, T. W., Murray, B. J., Wagner, R., Möhler, O., Saathoff, H., Schnaiter, M., Skrotzki, J., Price, H. C., Malkin, T. L., Dobbie, S., and Al-Jumur, S. M. R. K.: *Glassy aerosols with a range of compositions nucleate ice heterogeneously at cirrus temperatures*, Atmospheric Chemistry and Physics, 12, 8611–8632, 2012.

Wilson, T. W., Ladino, L. A., Alpert, P. A., Breckels, M. N., Brooks, I. M., Browse, J., Burrows, S. M., Carslaw, K. S., Huffman, J. A., Judd, C., Kilthau, W. P., Mason, R. H., McFiggans, G., Miller, L. A., Nájera, J., Polishchuk, E., Rae, S., Schiller, C. L., Si, M., Temprado, J. V., Whale, T. F., Wong, J. P. S., Wurl, O., Yakobi-Hancock, J. D., Abbatt, J. P. D., Aller, J. Y., Bertram, A. K., Knopf, D. A., and Murray, B. J.: *A marine biogenic source of atmospheric ice-nucleating particles*, Nature, 525, 234–238, 2015.

WISP-94: *Low Rate Navigation, State Parameter, and Microphysics Flight-Level Data. Version 1.0. UCAR/NCAR - Earth Observing Laboratory*, 2011.

WMO: International meteorological vocabulary, Geneva, Switzerland: Secretariat of the World Meteorological Organization, 2nd edn., 1992.

Young, K. C.: *A Numerical Simulation of Wintertime, Orographic Precipitation: Part I. Description of Model Microphysics and Numerical Techniques*, Journal of the Atmospheric Sciences, 31, 1735–1748, 1974.

Yun, Y. and Penner, J. E.: *Global model comparison of heterogeneous ice nucleation parameterizations in mixed phase clouds*, Journal of Geophysical Research: Atmospheres, 117, D07 203, 2012.

Zhou, C., Penner, J. E., Lin, G., Liu, X., and Wang, M.: *What controls the low ice number concentration in the upper troposphere?*, Atmospheric Chemistry and Physics, 16, 12 411–12 424, 2016.